2018-03-05

Multi-scale Real Gas Transport in Shale Matrix

Xu, Jinze

UNIVERSITY OF CALGARY

Multi-scale Real Gas Transport in Shale Matrix

by

Jinze Xu

A THESIS

SUBMITTED TO THE FACULTY OF GRADUATE STUDIES

IN PARTIAL FULFILMENT OF THE REQUIREMENTS FOR THE

DEGREE OF DOCTOR OF PHILOSOPHY

GRADUATE PROGRAM IN CHEMICAL AND PETROLEUM ENGINEERING

CALGARY, ALBERTA

MARCH, 2018

Abstract

As one of the clean energy resources, shale gas significantly reduces greenhouse gas emissions. The description of the gas transport behavior in shale rocks is one of the numerous challenges for further studies on economically developing shale gas reservoirs. In this work, real gas transport in the multi-scale porous structure of shale matrix is studied. Three models are, respectively, built at scales of single pores, a dual-porosity shale rock and a shale gas reservoir. These models are well validated with experimental, simulation and field data. Results indicate that increasing a taper ratio and an aspect ratio weakens a real gas effect and lowers bulk gas transport, including viscous flow and Knudsen diffusion, while the surface diffusion conductance first increases and decreases afterwards. More tortuous and complex pores weak the dominancy of the shale matrix in a dual-porosity shale rock. Transport conductance owns negative relationships with fractal dimensions of pore size and tortuosity of shale matrix, and positive relationship with minimum pore size. Gas production is underestimated without considering nano-scale pore size distribution-based gas transport mechanisms. A higher fractal dimension of a pore size and a higher variance result in higher cumulative gas production and lower sensitivity of gas production to a nano-scale pore size distribution.

Acknowledgements

First, I want to express my sincere appreciation to my supervisor Dr. Zhangxing (John) Chen for his support and guidance during my study at the University of Calgary. Dr. Chen keeps providing professional knowledge and suggestions to improve my research and skills. He is always patient and willing to help me solve the problems during my research.

I also would like thank Dr. Keliu for his detailed suggestions, patient guidance and great help for my research and professional skills.

I am extremely grateful to Drs. Nancy Chen, Frank Cheng, Gemma Lu and Shunde Yin, the members of my examination committees. They share lots of guiding and instructional opinions to improve my thesis.

The support of Department of Chemical and Petroleum Engineering, University of Calgary and Reservoir Simulation Group (RSG) is gratefully acknowledged as well. I hope to express my gratitude to all the staff of the Department and all the students in RSG.

Table of Contents

List of Tables

List of Figures and Illustrations

List of Symbols, Abbreviations and Nomenclature

Roman Symbol	Definition
A	Cross-sectional area, m^2
a	Length of the major axis of the cross section for a single tapered elliptical nanopore, m
b	Length of the minor axis of the cross section for a tapered elliptical nanopore, m
c	Gas transport conductance, $(mol \cdot m)/(Pa \cdot s)$;
D	Fractal dimension, dimensionless
$E()$	Complete elliptic integral of the second kind
d_p	Equivalent pore diameter, m
d_m	Gas molecular diameter, m
d_H	Mean hydraulic diameter, m
F	Cumulative probability, dimensionless
f	Probability density function
G_{kE}	Knudsen diffusion geometry parameter for a tapered elliptical nanopore, m^3, $= \frac{\gamma_E}{\xi_E(\xi_E+1)} K(1-\frac{1}{{\gamma_E}^2}){b_{in}}^3$
G_{kR}	Knudsen diffusion geometry parameter for a tapered rectangular nanopore, m^3, $= \frac{\gamma_R}{\xi_R(\xi_R+1)}[\gamma_R \ln\left(\frac{1}{\gamma_R}+\frac{1}{\gamma_R}\sqrt{1+{\gamma_R}^2}\right)+\ln(\gamma_R+\sqrt{1+{\gamma_R}^2})+\frac{1+{\gamma_R}^3-[1+{\gamma_R}^2]^{\frac{3}{2}}}{3\gamma_R}]{h_{in}}^3$

G_{sE} Surface diffusion geometry parameter for a tapered elliptical nanopore, m^2, $= \frac{\gamma_E}{\xi_E} {b_{in}}^2$

G_{sR} Surface diffusion geometry parameter for a tapered rectangular nanopore, m^2, $= \frac{\gamma_R}{\xi_R} {h_{in}}^2$

G_{vE} Viscous flow geometry parameter for a tapered elliptical nanopore, m^4, $= \frac{{\gamma_E}^3}{\xi_E({\gamma_E}^2+1)({\xi_E}^2+\xi_E+1)} {b_{in}}^4$

G_{vR} Viscous flow geometry parameter for a tapered rectangular nanopore, m^4, $= [1 - \frac{192\gamma_R}{\pi^5} \sum_{i=1,3,5,\ldots}^{\infty} \frac{tanh(i\pi/2\gamma_R)}{i^5}] \frac{{\gamma_R}^3}{\xi_R({\xi_R}^2+\xi_R+1)} {h_{in}}^4$

ΔH Isosteric adsorption heat at $\theta = 0, J/mol$

$H()$ Heaviside step function

h Height of the cross section for a tapered rectangular nanopore, m

K_A Apparent permeability, m^2

Kn Knudsen number, dimensionless

$K()$ Complete elliptic integral of the first kind

k Boltzmann constant, $= 1.38 \times 10^{-23}\ J/K$

L Straight length of sample, m

L_t Tortuous length of the pore, m

M Gas molecular weight, kg/mol

N_p Total number of pores with the equivalent pore diameter larger than d_p in shale matrix, dimensionless

N_A Avogadro constant, $= 6.02 \times 10^{23}\ mol^{-1}$

n	Molecular number density, m^{-3}
o_1	Fitting coefficient, $= 7.9$
o_2	Fitting coefficient, $= 9 \times 10^{-6}$
o_3	Fitting coefficient, $= 0.28$
P	Pressure, Pa
P_c	Critical pressure, Pa
P_e	Effective confined pressure, Pa
P_L	Langmuir pressure, Pa
P_{ob}	Overburden pressure, Pa
P_r	Reduced pressure, dimensionless, $= \frac{P}{P_c}$
Q	Transport molar rate in shale matrix, mol/s
Q_{prod}	Cumulative gas production, m^3/s
q	Transport molar rate in a single pore, mol/s
q_D	Dimensionless transport molar rate in a single pore, dimensionless
R	Gas constant, $= 8.314\ J/(K \cdot mol)$
S	Lateral surface area of a nanopore, m^2
T	Temperature, K
T_c	Critical temperature, K
T_r	Reduced temperature, dimensionless, $= \frac{T}{T_{cz}}$
V	Volume of a nanopore, m^3
V_a	Pore volume occupied by the adsorbed gas in a nanopore, m^3
V_b	Pore volume occupied by the free gas in a nanopore, m^3

V_m	Molar volume, m^3/mol
$\overline{v}$	Average molecular speed from Maxwell-Boltzmann distribution, m/s
Z	Gas compressibility factor, dimensionless

Greek Symbol	Definition
α	Function of gas properties and temperature in the SRK EOS, dimensionless
γ	Aspect ratio, dimensionless
λ	Mean free path, m
χ	Repulsion parameter in the SRK EOS, $(Pa \cdot m^3)/mol$
σ	Fracture aperture, m
Ψ	Ratio between the blockage rate constant and the forward migration rate constant, dimensionless
Γ	Gas transport ratio, dimensionless
κ	Attraction parameter in the SRK EOS, m^3/mol
ω	Acentric factor, dimensionless
ξ	Taper ratio, dimensionless
ϕ	Porosity, dimensionless
$\mathfrak{D}_k$	Knudsen diffusion coefficient, m^2/s
$\mathfrak{D}_s$	Surface diffusion coefficient, m^2/s
θ	Gas coverage, dimensionless
ρ	Gas density, kg/m^3
μ	Gas viscosity, $Pa \cdot s$

μ_0	Gas viscosity at P = 1.01325×105 Pa and T = 423 K, $= 2.31 \times 10^{-5}\ Pa \cdot s$
η	Ratio between d_{pmin} and d_{pmax} in shale matrix, dimensionless, $= d_{pmin}/d_{pmax}$.

Subscript	Definition
0	Initial condition
a	Adsorbed gas
b	Free gas
E	A tapered elliptical nanopore
f	Natural fracture
i	Ideal gas
in	Inlet
k	Knudsen diffusion
m	Shale matrix
max	Maximum
min	Minimum
out	Outlet
p	Pore
R	A tapered rectangular nanopore
s	Surface diffusion
t	Total

v	Viscous flow

Abbreviation	Definition
EOS	Equation of state
SRK	Soave-Redlich-Kwong
TMAC	Tangential momentum accommodation coefficient

Chapter One: Introduction

As a game changer, shale gas is continuing to have repercussions for energy scenarios worldwide. Owing to advanced drilling and hydraulic fracturing, shale gas is developed very fast in North America (Wang et al., 2011). The study from the American Natural Gas Alliance (ANGA) indicates that North America owns a supply capacity of the natural gas for at least next 100 years (Bocora, 2012). However, a number of challenges still needed to be addressed. In Canada, exploration and production have been performed in many shale gas plays (i.e., Muskwa shale, Montney shale and Duvernay shale). In western Canada, the first gas discovery was made in Medicine Hat, Alberta, 1883 (Rivard et al., 2014). Canada is now the third largest producer and the fourth largest exporter of natural gas in the world (Rivard et al., 2014). However, the development of shale gas reservoirs still faces numerous challenges. The description of the gas transport behavior in shale rocks is one of the numerous challenges for further studies on evaluating gas transport efficiency, optimizing well production and economically developing shale gas reservoirs (Shapiro et al., 2008).

1.1 Research Background

Shale gas flow in fractures is the continuum flow, which can be described by the conventional Darcy equation. However, when gas goes to nanopores of shale matrix, the interaction between the pore walls and the gas molecules cannot be neglected as the pore size of nanopores is comparable to the mean free path of gas molecules under reservoir conditions; the gas transport in shale matrix thus becomes non-continuum. Complex pore structures of tapered non-circular pores, real gas effects and the upscaling of a model from the scale of a single pore to the scale of a bundle

of pores bring about further difficulties. Modelling of multi-scale real gas transport in shale matrix becomes challenging and attracts much interest in this topic.

Shale gas is mainly generated from thermogenic degradation of organic contents, cracking of oil, and biogenic degradation of organic contents (Loucks et al., 2010). As an ultra-tight rock, shale exhibits low permeability (nanodarcy to microdarcy), low porosity (2% to 15%) (Curtis et al., 2002) and a low pore diameter (1 nm to 1 μm) (Figure 1-1). Two types of pores exist in shale. One is a nanopore, which is found in clay-rich mud rock (Reed and Loiucks, 2007), and the other is a micropore, which is found in silica-rich mud rock (Bustin et al., 2008). Nanopores dominate in shale rock containing both micropores and nanopores (Loucks et al., 2009). Moreover, the organic content provides a platform for the transport of shale gas in porous media, and the adsorbed gas and free gas coexist in pores (Levorsen and Berry, 1967). This research focuses on free gas, which dominates the production of shale gas from shale formations (Kuuskraa et al., 2013). The adsorbed gas molecules are bound; thus, they exhibit no kinetic energy and do not affect the gas phase pressure (Heller and Zoback, 2014).

Under high pressure, as a volume occupied by molecules is significantly reduced, enormous intermolecular and molecule-wall collisions occur (Bolsaitis and Spain, 1977; Singh, 2010). Generally, the classical Knudsen number is employed to divide the flow regime as continuum flow ($Kn<0.001$), laminar slip flow ($0.001<Kn<0.1$), transition flow ($0.1<Kn<10$), and free-molecular flow ($Kn>10$) (Cunningham and Williams, 1980). However, considering the existence of adsorbed gas transport in shale matrix, classical flow regime classification cannot be well applied in the real gas transport in shale matrix. Recent studies on shale gas models in nanopores mostly interpreted the transport behavior simply from the mathematical value of a Knudsen number. Both

intermolecular and molecule-wall collisions (Figure 1-2) play important roles in flow regimes. Knudsen diffusion, which is also known as Knudsen collision, is mainly controlled by molecule-wall collision (Cunningham and Williams, 1980).

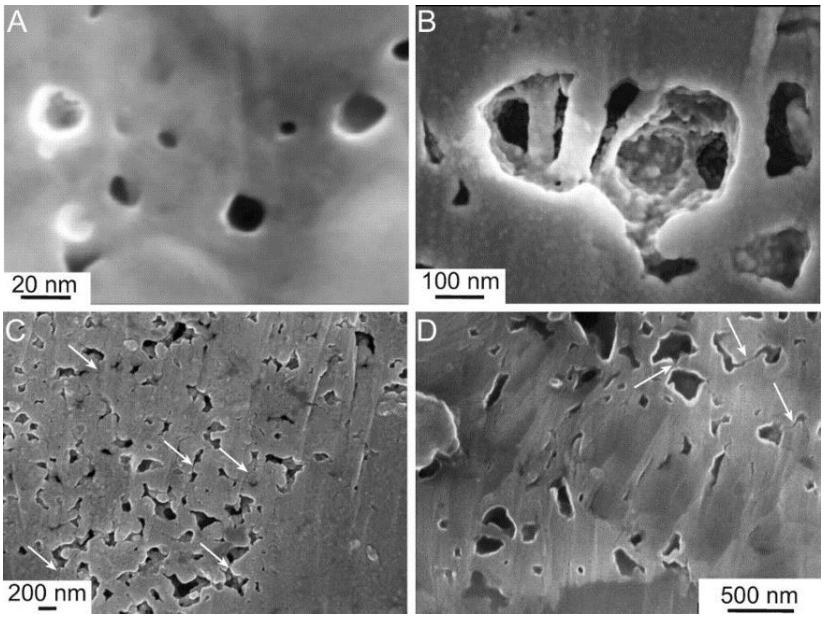

Figure 1-1 Variations in nanopores of shale rocks by secondary electron (Loucks et al., 2009)

Many models have been proposed to explore the gas transport mechanisms in single nanopores. In 2007, Javadpour et al. adopted the ideal gas kinetic theory to study the transport behavior of shale gas in nanopores (Javadpour et al., 2007). In this initial model, the Knudsen diffusion is mostly discussed without considering the laminar slip flow. In 2009, they further coupled the Knudsen diffusion and laminar slip flow by using the ideal gas EOS (equation of state) to calculate the total transport flux of ideal gas (Javadpour, 2009). This model has served as basis for many succeeding models developed from 2009 to 2015. In 2012 and 2015, Darabi et al. and Guo et al. further discussed and updated the apparent permeability by introducing the ratio of porosity and tortuosity as a correction factor for the structure of nanopores based on ideal gas EOS;

this factor remains the focus of ideal gas law (Darabi et al., 2012; Guo et al., 2015). In 2015, Wu et al. interpreted the transport behavior of shale gas from the perspective of molecular collision by directly adding weights to the nanofludic items based on the ideal gas EOS (Wu et al., 2015). Ren et al. (2016) studied the gas transport behavior in shale matrix by considering the slip flow as a part of Knudsen diffusion to avoid the estimation of a tangential momentum accommodation coefficient (TMAC) in slip models.

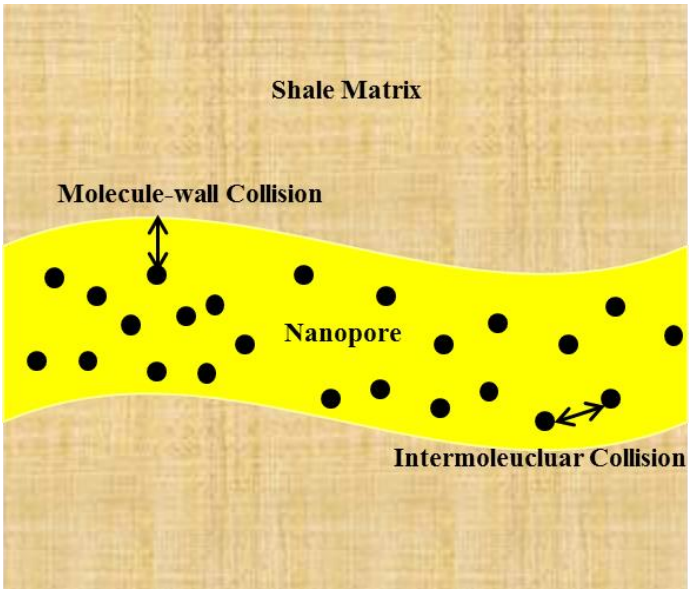

Figure 1-2 Schematic view of gas transport in the nanopores of shale rocks

Gas transport in a bundle of pores in shale matrix were studied in past years. Zheng and Yu (2012) established a permeability model for gas flow in dual-porosity media and obtained good validations with experimental data. Miao et al. (2015) investigated the gas transport behavior by using the fractal geometry theory for dual-porosity rocks embedded with random fractures, which can reveal more mechanisms of seepage characteristics than traditional models. Li et al. (2016) showed that the results obtained from a fractal model in a dual-porosity medium can well match

those from numerical simulation. However, the previous fractal models in dual-porosity rocks are limited for ideal gas transport under a low Knudsen number (viscous flow).

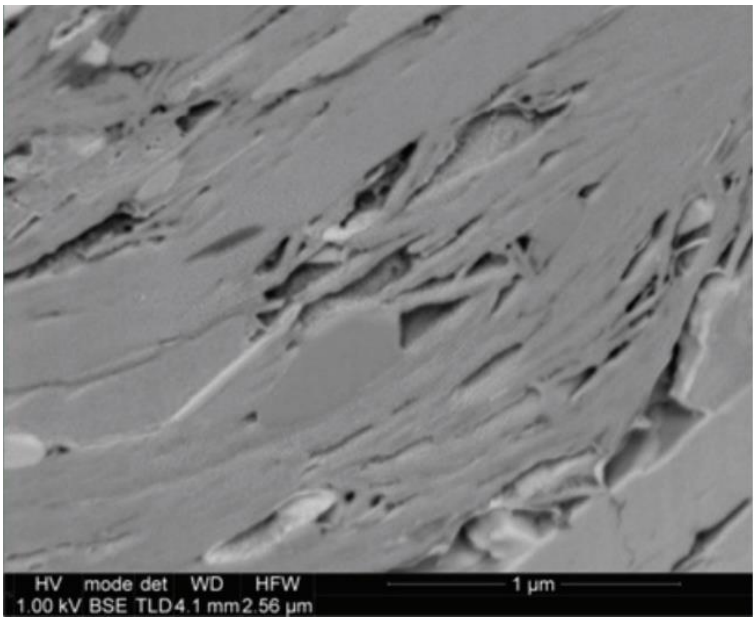

Figure 1-3 Pore structures in shale rock (Curtis et al., 2010)

1.2 Statement of Problems

Extensive studies have been performed on the multi-scale gas transport in shale matrix. However, some limitations still exist for these studies, which can be summarized as follows:

(1) Current models still have deficiencies to capture a pore structure and present a real gas flow regime in a single nanopore.

The tapered non-circular structure of nanopores was not captured (Figure 1-3), which has been reported by many experimental observations (Wilson et al., 2016; Bu et al., 2015; Shan et al., 2015; Nikolov, 2014; Curtis, 2010; Slatt and O'Brien, 2011). The empirical formula was widely used to describe the real gas effect, which limits the model within several kinds of gases. Contributions of free gas transport to transport efficiencies in nanopores have not been explored.

Flow regimes of real gas transport in nanopores with considering different transport mechanisms (viscous flow, Knudsen diffusion and surface diffusion) were not explored.

(2) Current models still have deficiencies to present effects of a pore size distribution on gas transport behavior in shale matrix with a bundle of pores.

The previous models for gas transport in a bundle of pores in shale matrix were limited to ideal gas transport under a low Knudsen number (viscous flow), and the effect of shale matrix on gas transport in a dual-porosity shale rock is not studied. In order to better understand the role of shale matrix, an improved model is needed to bridge the pore size distribution, fracture aperture distribution and multiple transport mechanisms (viscous flow, Knudsen diffusion and surface diffusion) in a dual-porosity shale rock.

(3) At the reservoir scale, effects of nano-scale pore size distributions on shale gas production are needed to be revealed.

Previous studies ignored a pore size distribution, and directly connected single nanopores and a shale gas reservoir, which results in an unrealistic estimation of gas transport efficiency with ignoring gas transport mechanisms in a bundle of pores. A thorough analysis of effects of a nano-scale pore size distribution on shale gas production is thus needed.

1.3 Objectives of this Work

Based on the existing problems, this work includes three parts: real gas transport in tapered non-circular nanopores, real gas transport in shale matrix with a bundle of pores and effects of a nano-scale pore size distribution on production performance of a shale gas reservoir. These three parts of the work cover scales of single nanopores, a bundle of pores and a reservoir, and they are

bridged with each other to construct the main thread of the work as shown in Figure 1-4.The objectives are as follows:

(1) To construct a model for gas transport in tapered non-circular nanopores of shale rocks integrating a pore structure, a real gas effect, and molecular kinetic and transport behavior. Based on this model, we explain the gas transport behavior in tapered single nanopores.

(2) To establish a real gas transport model in a dual-porosity shale rock composed of a bundle of pores in shale matrix and a bundle of channels in natural fractures with fractal structures based on the first stage of work. Based on this stage of the work, we explore the effect of shale matrix on gas transport in a dual-porosity shale rock.

(3) To establish an improved approach to integrate a pore size distribution, a real gas effect, nano-scale gas transport mechanisms, a geomechanical effect and computational simulation of shale gas production. Based on this approach, we indicate the impact of a nano-scale pore size distribution on shale gas production.

1.4 Structure of this Thesis

This thesis is structured as follows: after clarifying the research objectives in Chapter 1, the gas transport mechanisms in tapered single nanopores are investigated by an analytical model in Chapter 2. The success of this model provides a basis for the upscaling of the model from single nanopores to a bundle of pores. A gas transport model is then built based on a fractal theory to describe the gas transport behavior in a dual-porosity shale rock in Chapter 3. In order to account for effects of a nano-scale pore size distribution on gas production, an improved approach is employed to bridge a pore size distribution, multiple gas transport mechanisms and gas production in Chapter 4. Lastly the results and recommendations in this thesis are concluded in Chapter 5.

Literature reviews of previous studies are included in the introduction section of each chapter.

Chapter Two: Real Gas Transport in Tapered Non-Circular Nanopores of Shale Rocks

2.1 Introduction

With the increase in energy consumption worldwide, shale gas has become an important energy resource. As a clean source of fuel among other sources (crude oil, coal, etc.), shale gas significantly reduces greenhouse gas emission (Wang et al., 2011). With the enormous application of hydraulic fracturing, shale gas has been rapidly explored in North America. However, the development of shale gas still faces numerous challenges. For instance, the transport behavior of shale gas considerably changes in nanopores (Wu et al., 2015). Thus, studies on gas transport in nanopores basically contribute to investigations on this resource, indicating the mechanisms of the transport behavior and benefits in the optimization of operation.

Shale rocks that are deep underground are formed by compaction and solidification with increasing pressure over a long period of time (Zhang et al., 2012; Rogers, 2011). This process provides the high-pressure condition for the transport of shale gas in nanopores. The chemical and physical parameters in the three formations of Duvernay Shale (Munson, 2015), Marcellus Shale (Kargbo et al., 2010; Soeder, 1988), and Bowland Shale (Andrews, 2013) from Canada, the United States and the United Kingdom, respectively, are summarized in Table 2-1. For hydrocarbons found underground, they only exhibit ideal-gas behavior at a pressure of approximately 1 MPa (Wang, 2004). Once the pressure is >1 MPa, the gas properties may deviate from the ideal case. As we can see the pressure range from Table 2-1, the ideal gas equation of state (EOS) is no more appropriate for the shale gas in the underground. Though the empirical equation can consider the real gas effect, it is developed for the particular gas, which limits its application range (Wu et al., 2016; Ren et al., 2016). Thus real gas EOS should be introduced into the study of real gas transport

in nanopores, which is able to present the real gas effect for more kinds of gases. However, for previous models on the transport of real gas in nanopores, ideal gas law and empirical equations are still employed (Wu et al., 2016; Ren et al., 2016).

Table 2-1 Reservoir condition of shale gas in different formations

Formation	Duvernay Shale	Marcellus Shale	Bowland Shale
Country	Canada	United States	United Kingdom
Depth range (m)	3000-4000	1200-2500	1800-2500
Pressure range (MPa)	35-70	10-35	10-40
Temperature (K)	360-390	310-340	330-350

As an ultra-tight rock, shale exhibits low permeability (nanodarcy to microdarcy), low porosity (2% to 15%), and low pore size (1-1000 nm) (Curtis, 2002). In terms of geometries of cross sections for nanopores in shale gas reservoirs, they are commonly irregular bubble-like, elliptical and rectangular (Loucks et al., 2009; Wilson et al., 2016). Along the axial direction, nanopores exhibit both the straight and tapered characteristics (Wilson et al., 2016; Bu et al., 2015; Shan et al., 2015; Nikolov, 2014; Curtis, 2010; Slatt and O'Brien, 2011). Thus, both geometries of cross section and tapering effects should be considered to present mathematical and physical models that can better describe the gas transport in nanopores of shale rocks. Though recent studies have taken the non-circular cross section into consideration, limitations exist (e.g. ignorance of tapering effect and elliptical cross section in Wu et al. model (Wu et al., 2016), neglect of tapering effect and surface diffusion in Ren et al. model (Ren et al., 2016)).

Table 2-2 is a brief summary of previous models for the transport of shale gas in naonopores (Wu et al., 2016; Ren et al., 2016; Javadpour, 2009; Civan, 2010; Darabi et al., 2012; Rahmanian

et al., 2012; Sheng et al., 2015), and these models have been reviewed in the past. Before 2015, most of the shale gas models in nanopores are based on the ideal gas law. Though the real gas effect is considered in Wu et al. model and Ren et al. model in 2016, the models are based on the empirical equation of methane properties, which limits the application of the models in more kinds of gases. Besides the real gas EOS, the tapered nanopore structure is also neglected in previous models. Hence, a more realistic model that bridges the connections among real gas phase behavior, molecular kinetics, and transport behavior for shale gas in straight/tapered non-circular nanopores should be developed.

Table 2-2 Features of existing gas transport models in nanopores

Model	Description	Comments
Javadpour, 2009, Civan, 2010, Darabi et al, 2012	Ideal gas EOS; Linear superposition of viscous flow and Knudsen diffusion based on the slip boundary condition; Straight circular pores	Only for ideal gas in straight circular pore; Neither adsorption nor surface diffusion
Rahmanian et al, 2013	Ideal gas EOS; Weighted superposition of viscous flow and Knudsen diffusion based on slip boundary condition; Straight circular pores	Only for ideal gas in straight circular pore; Neither adsorption nor surface diffusion
Sheng et al, 2015	Ideal gas EOS; Weighted superposition of viscous flow,	Only for ideal gas in straight circular pore.

	Knudsen diffusion and surface diffusion based on slip boundary condition; Straight circular pores	
Wu et al., 2016	Consideration of real gas effect based on empirical equation of methane; Weighted superposition of viscous flow, Knudsen diffusion and surface diffusion based on the slip boundary condition; Straight pores with circular and rectangular cross sections	Empirical equation to describe real gas effect; straight rectangular and circular pores (elliptical cross section is omitted); Compressibility factor is always larger than 1 which is not real under low pressure
Ren et al., 2016	Consideration of real gas effect based on empirical equation of methane; Linear supervision of viscous flow and Knudsen diffusion based on non-slip boundary; Straight pores with elliptical and rectangular cross sections	Empirical equation to describe real gas effect; Straight pores; Neither adsorption nor surface diffusion

2.2 Model Establishment

In this study, we establish a model to bridge real gas effect, molecular kinetics and transport behavior in the tapered non-circular nanopore. The tapered nanopore structure with non-circular (elliptical and rectangular) cross sections is shown in Figure 2-1.

Basic geometric characteristics of the tapered non-circular nannopores in this model are described as follows:

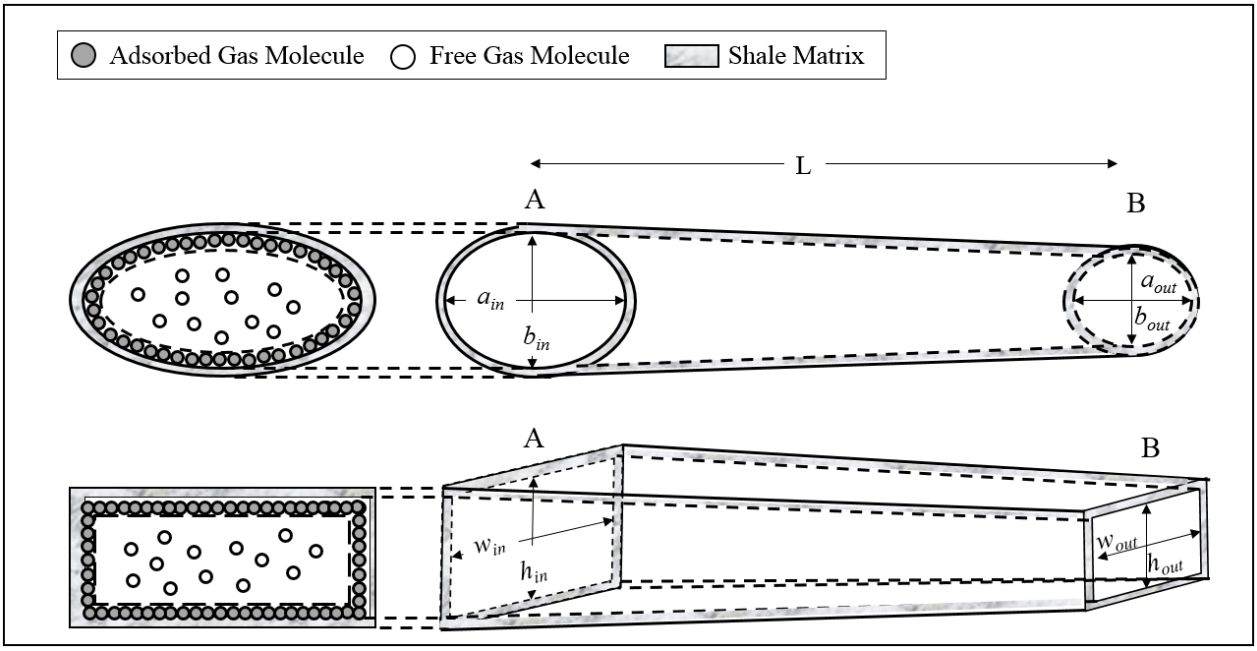

Figure 2-1 Schematic view of tapered non-circular nanopores

(1) Tapered elliptical nanopores: the length of the major axis of the inlet cross section is a_{in}, and the length of the major axis of the outlet cross section is a_{out}, which is $\leq a_{in}$. The length of the minor axis of the inlet cross section is b_{in}, and the length of the minor axis of the outlet cross section is b_{out}, which is $\leq b_{in}$. In this model, following relationships exist:

$$\frac{a_{in}}{a_{out}} = \frac{b_{in}}{b_{out}} = \xi_E \tag{2-1a}$$

$$\frac{a_{in}}{b_{in}} = \frac{a_{out}}{b_{out}} = \gamma_E \tag{2-1b}$$

where ξ_E is the taper ratio for tapered elliptical nanopores, dimensionless; γ_E is the aspect ratio for tapered elliptical nanopores, dimensionless.

For the tapered nanopore in Figure. 2-1, the pore size decreases along the length from the inlet A to the outlet B, which indicates the taper ratio is more or equal than 1. If the flow is reverse (from B to A), the pore size increases along the length of the nanopore from B to A and we can refer to such nanopore as the widening nanopore, in which case the same transport molar rate can be obtained. While $\xi_E = 1$ and $\gamma_E = 1$, the nanopore is straight with circular cross section.

(2) Tapered rectangular nanopores: The width of the inlet cross section is w_{in}, and the width of the outlet cross section is w_{out}, which is $\leq w_{in}$. The height of the inlet cross section is h_{in}, and the height of the outlet cross section is h_{out}, which is $\leq h_{in}$. In this model, following relationships exist:

$$\frac{w_{in}}{w_{out}} = \frac{h_{in}}{h_{out}} = \xi_R \tag{2-2a}$$

$$\frac{w_{in}}{h_{in}} = \frac{w_{out}}{h_{out}} = \gamma_R \tag{2-2b}$$

where ξ_R is the taper ratio for tapered rectangular nanopores, dimensionless; γ_R is the aspect ratio for tapered rectangular nanopores, dimensionless.

While $\xi_R = 1$ and $\gamma_R = 1$, the nanopore is straight with square cross section.

(3) Taper function: We assume that the pore diameter decreases linearly along the pores, which is based on the experimental observation (Figure 3(B) in the paper from Shan et al., 2015; Figure 10(b) in Curtis et al, 2010; Figure 21 in paper from Nikolov, 2014 and Figure 15(D) in the paper from Slatt and O'Brien, 2011). The taper function is expressed as follows:

$$\frac{d(a)}{dx} = \frac{a_{out} - a_{in}}{L} \tag{2-3a}$$

$$\frac{d(b)}{dx} = \frac{b_{out} - b_{in}}{L} \tag{2-3b}$$

$$\frac{d(h)}{dx} = \frac{h_{out} - h_{in}}{L} \tag{2-3c}$$

$$\frac{d(w)}{dx} = \frac{w_{out} - w_{in}}{L} \tag{2-3d}$$

where a is the length of the major axis of the cross section for tapered elliptical nanopores, m; b is the length of the minor axis of the cross section for tapered elliptical nanopores, m; h is the height of the cross section for tapered rectangular nanopores, m; w is the width of the cross section for tapered rectangular nanopores, m; L is the length of the nanopore, m.

2.2.1 Transport Behavior

Based on the Knudsen number, leading mechanism of gas transport includes continuum flow, slip flow, transitional flow and Knudsen diffusion (Majumder et al., 2011). While the Knudsen number is less than 0.001, the intermolecular collision dominates and the transport regime refers to the continuum flow; If the Knudsen number ranges from 0.001 to 0.1, with the increase of the molecular-wall collision frequency, the slippage exists and the type of the transport regime is the slip flow; For the Knudsen number between 0.1 and 10, the intermolecular collision frequency and the molecular-wall collision frequency is nearly the same, and the transport regime is the transitional flow; If the Knudsen number is larger than 10, the molecular-wall collision dominates, and the transport regime refers to the Knudsen diffusion. Many significant models have been proposed to combine these gas transport mechanisms as summarized in Table. 2. In this work, we adopt the approach of linear superposition of viscous flow, Knudsen diffusion and surface diffusion (Ren et al., 2016; Noy, 2013; Singh et al., 2014). The transport mechanism of free gas in

nanopores is summarized as the Knudsen diffusion and viscous flow, which together contribute to the transport of free gas in the nanopores. The transport mechanism of adsorbed gas in nanopores is characterized as the surface diffusion, which exists in the single-layer in the internal adsorbed surface of nanopores (Wu et al., 2016). In this model, the pressure gradient is constant ($\nabla P = \frac{\Delta P}{L}$) (Roy et al., 2003; Gunda et al., 2013).

2.2.1.1 Viscous Flow

The viscous flow flux resulting from the pressure driving force is expressed by the Hagen-Poiseuille equation. In order to avoid the empirical parameter of tangential momentum accommodation coefficient (TMAC), the slippage effect is included in the Knudsen diffusion and the construction of viscous flow molar rate (Q_v) follows the no-slip boundary (Ren et al., 2016).

The expression of q_v for single nanopores with rectangular and elliptical cross sections is as follows (White, 2006):

$$q_v = \begin{cases} -\frac{\phi_b}{\tau}\frac{4\rho w^3 h}{3\mu M}\left[1 - \frac{192w}{\pi^5 h}\sum_{i=1,3,5,\ldots}^{\infty}\frac{tanh(i\pi h/2w)}{i^5}\right]\nabla P, Rectangular \\ -\frac{\phi_b}{\tau}\frac{\pi\rho}{64\mu M}\frac{a^3b^3}{a^2+b^2}\nabla P, Elliptical \end{cases} \quad (2\text{-}4)$$

where q_v is the viscous flow molar rate in single nanopores, mol/s; ϕ_b is the effective porosity for bulk gas transport (see Appendix A); τ is the tortuosity of the nanopore; ρ is the density, kg/m^3; μ is the viscosity, $Pa \cdot s$; M is the molar mass, kg/mol; P is the pressure, Pa.

By coupling Equations (2-1), (2-2), (2-3) and (2-4) we can obtain the expression of q_v for single tapered nanopores with rectangular and elliptical cross sections as follows (see Appendix B):

$$q_v = \begin{cases} -\frac{\phi_b}{\tau}\frac{\rho}{4\mu M} G_{vR} \nabla P, Rectangular \\ -\frac{\phi_b}{\tau}\frac{3\pi\rho}{64\mu M} G_{vE} \nabla P, Elliptical \end{cases} \quad (2\text{-}5)$$

where G_{vR} is the viscous flow geometry parameter for tapered rectangular nanopores, m^4, $= [1 - \frac{192\gamma_R}{\pi^5}\sum_{i=1,3,5,\ldots}^{\infty}\frac{tanh(i\pi/2\gamma_R)}{i^5}]\frac{{\gamma_R}^3}{\xi_R({\xi_R}^2+\xi_R+1)}{h_{in}}^4$; G_{vE} is the viscous flow geometry parameter for tapered elliptical nanopores m^4, $= \frac{{\gamma_E}^3}{\xi_E({\gamma_E}^2+1)({\xi_E}^2+\xi_E+1)}{b_{in}}^4$.

Thus, we obtain the viscous flow conductance (c_v) for gas transport in single nanopores as follows:

$$c_v = \begin{cases} \frac{\phi_b}{\tau}\frac{\rho}{4\mu M} G_{vR}, Rectangular \\ \frac{\phi_b}{\tau}\frac{3\pi\rho}{64\mu M} G_{vE}, Elliptical \end{cases} \quad (2\text{-}6)$$

where c_v is the viscous flow conductance in singlle nanopores, $(mol \cdot m)/(Pa \cdot s)$.

2.2.1.2 Knudsen Diffusion

The Knudsen diffusion coefficient (D_k) for nanopores with rectangular and elliptical cross sections is as follows (Lafferty, 1998):

$$\mathfrak{D}_k = \begin{cases} \frac{\bar{v}h}{4}[\gamma_R \ln\left(\frac{1}{\gamma_R}+\frac{1}{\gamma_R}\sqrt{1+{\gamma_R}^2}\right) + \ln\left(\gamma_R+\sqrt{1+{\gamma_R}^2}\right) + \frac{1+{\gamma_R}^3-[1+{\gamma_R}^2]^{\frac{3}{2}}}{3\gamma_R}], Rectangluar \\ \frac{2\bar{v}b}{3\pi}K(1-\frac{1}{{\gamma_E}^2}), \ Elliptical \end{cases} \quad (2\text{-}7)$$

where $\mathfrak{D}_k$ is the Knudsen diffusion coefficient, m^2/s; $\overline{v}$ is the mean molecular speed from Maxwell-Boltzmann distribution, m/s; $K()$ is the complete elliptic integral of the first kind.

The Knudsen diffusion molar rate (q_k) in single nanopores is as the following (Cunningham, 1980):

$$q_k = -\frac{\phi_b A}{\tau ZRT} D_k \nabla P \quad (2\text{-}8)$$

where q_k is the Knudsen diffusion molar rate in single nanopores, mol/s; A is the cross-sectional area, m^2; R is the gas constant, $= 8.314\, J/(K \cdot mol)$; T is the temperature, K; Z is the compressibility factor, dimensionless.

By coupling Equations (2-1), (2-2), (2-3), (2-7) and (2-8), we could get the expression of Q_k in the tapered nanopore with rectangular and elliptical cross sections as the following equation:

$$q_k = \begin{cases} -\frac{\phi_b}{\tau}\frac{G_{kR}}{Z}\sqrt{\frac{2}{\pi RMT}}\nabla P, \ \ Rectangular \\ -\frac{\phi_b}{\tau}\frac{G_{kE}}{Z}\sqrt{\frac{8}{9\pi RMT}}\nabla P, \ Elliptical \end{cases} \tag{2-9}$$

where G_{kR} is the Knudsen diffusion geometry parameter for tapered rectangular nanopores, m^3, $= \frac{\gamma_R}{\xi_R(\xi_R+1)}[\gamma_R \ln\left(\frac{1}{\gamma_R}+\frac{1}{\gamma_R}\sqrt{1+{\gamma_R}^2}\right)+\ln\left(\gamma_R+\sqrt{1+{\gamma_R}^2}\right)+\frac{1+{\gamma_R}^3-\left[1+{\gamma_R}^2\right]^{\frac{3}{2}}}{3\gamma_R}]{h_{in}}^3$; G_{kE} is the Knudsen diffusion geometry parameter for tapered elliptical nanopores, m^3, $= \frac{\gamma_E}{\xi_E(\xi_E+1)}K(1-\frac{1}{{\gamma_E}^2}){b_{in}}^3$.

The Knudsen diffusion conductance (c_k) in single nanopores is defined as follows：

$$c_k = \begin{cases} \frac{\phi_b}{\tau}\frac{G_{kR}}{Z}\sqrt{\frac{2}{\pi RMT}}, \ \ Rectangular \\ \frac{\phi_b}{\tau}\frac{G_{kE}}{Z}\sqrt{\frac{8}{9\pi RMT}}, \ Elliptical \end{cases} \tag{2-10}$$

where c_k is the Knudsen diffusion conductance in single nanopores, $(mol \cdot m)/(Pa \cdot s)$.

2.2.1.3 Surface Diffusion

Besides the viscous flow and Knudsen diffusion, surface diffusion also exists in nanopore, which happens in the adsorbed layer formed on walls of nanopores.

For the single adsorbed layer, we apply Langmuir's law with considering real gas effect to calculate the gas coverage (θ) for the adsorbed gas (Civan et al., 2014):

$$\theta = \frac{P/Z}{P/Z+P_L} \tag{2-11}$$

where θ is the gas coverage, dimensionless; P_L is the Langmuir pressure, Pa.

The surface diffusion coefficient (D_s) is calculated as follows (Chen and Yang, 1991; Wu et al., 2015):

$$\mathfrak{D}_s = 8.29 \times 10^{-7} T^{0.5} \exp\left(-\frac{\Delta H^{0.8}}{RT}\right) \frac{2(1-\theta)+\Psi\theta(2-\theta)+[H(1-\Psi)](1-\Psi)\Psi\theta^2}{2(1-\theta+\frac{\Psi}{2})^2} \tag{2-12}$$

where $\mathfrak{D}_s$ is the surface diffusion coefficient, m^2/s; ΔH is the isosteric adsorption heat at $\theta = 0$, J/mol; $H()$ is the Heaviside step function; Ψ is the ratio between the blockage rate constant and the forward migration rate constant, dimensionless.

The surface diffusion molar rate (q_s) in single nanopores is calculated as follows (Wu et al., 2015)

$$q_s = -\frac{4\phi_a \theta A \mathfrak{D}_s}{\pi\tau N_A {d_m}^3 P} \nabla P \tag{2-13}$$

where q_s is the surface diffusion molar rate in single nanopores, mol/s; ϕ_a is the effective porosity for adsorbed gas transport (see Appendix A); N_A is the Avogadro constant, $= 6.02 \times 10^{23}\ mol^{-1}$; d_m is the molecular diameter, m.

By coupling Equations (2-1), (2-2), (2-3) and (2-13), we can get q_s for single tapered nanopores with non-circular cross sections as follows:

$$q_s = \begin{cases} -\frac{4\phi_a \theta \mathfrak{D}_s G_{sR}}{\pi\tau N_A {d_m}^3 P} \nabla P, Rectangular \\ -\frac{\phi_a \theta \mathfrak{D}_s G_{sE}}{\tau N_A {d_m}^3 P} \nabla P, Elliptical \end{cases} \tag{2-14}$$

where G_{sR} is the surface diffusion geometry parameter for tapered rectangular nanopores, m^2, $= \frac{\gamma_R}{\xi_R} {h_{in}}^2$; G_{sE} is the surface diffusion geometry parameter for tapered elliptical nanopores, m^2, $= \frac{\gamma_E}{\xi_E} {b_{in}}^2$.

Thus the surface diffusion conductance (c_s) for single nanopores is expressed as follows:

$$c_s = \begin{cases} \frac{4\phi_a \theta \mathfrak{D}_s G_{sR}}{\pi \tau N_A {d_m}^3 P}, Rectangular \\ \frac{\phi_a \theta \mathfrak{D}_s G_{sE}}{\tau N_A {d_m}^3 P}, Elliptical \end{cases} \quad (2\text{-}15)$$

where c_s is the surface diffusion conductance for single nanopores, $(mol \cdot m)/(Pa \cdot s)$.

2.2.2 Molecular Kinetics

For the present model, the system contains gas molecules with velocities that are randomly selected from the Maxwell-Boltzmann distribution. The mean molecular speed ($\overline{v}$) from the Maxwell-Boltzmann distribution is given below (Javadpour et al., 2007):

$$\overline{v} = 2\sqrt{\frac{2RT}{\pi M}} \quad (2\text{-}16)$$

The expression of Knudsen number (Kn) is as follows (Barisik and Beskok, 2014):

$$Kn = \frac{\lambda}{d_H} \quad (2\text{-}17)$$

where Kn is the Knudsen number, dimensionless, d_H is the mean hydraulic diameter, m (see Appendix A).

The mean free path (λ) can be expressed as follows (Barisik and Beskok, 2014):

$$\lambda = \frac{1}{\pi n d_m^2} \quad (2\text{-}18)$$

where λ is the mean free path, m; n is the gas molecular number density, $1/m^3$.

2.2.3 Equation of State

Soave-Redlich-Kwong (SRK) EOS considers the repulsion and attraction forces of gas molecules in physics and includes the corresponding parameters in its mathematical expression. Considering the real gas in nanopores with specific volume under certain pressure and temperature, the SRK EOS is as follows (Tassio, 2013):

$$P = \frac{RT}{V_m - \chi} - \frac{\alpha\kappa}{V_m(V_m + \chi)} \tag{2-19a}$$

$$\kappa = 0.42748 \frac{R^2 T_c^2}{P_c} \tag{2-19b}$$

$$\chi = 0.08664 \frac{RT_c}{P_c} \tag{2-19c}$$

$$\alpha = [1 + (0.48508 + 1.55171\omega - 0.15613\omega^2)\left(1 - \sqrt{T_r}\right)]^2 \tag{2-19d}$$

where χ is a repulsion parameter in the SRK EOS, $(Pa \cdot m^3)/mol$; κ is an attraction parameter in the SRK EOS, m^3/mol; α is a function of gas properties and temperature in the SRK EOS, dimensionless; ω is the acentric factor, dimensionless; T_r is the reduced temperature, dimensionless, $= \frac{T}{T_c}$; V_m is the molar volume, m^3/mol; P_c is the critical pressure, Pa; T_c is the critical temperature, K; R is the gas constant, $= 8.314\ J/(K \cdot mol)$.

The solution of molar volume (V_m) from Equation (2-19) in this model is as follows:

$$V_m = -\frac{1}{3P}\left(B + \frac{3P\left(\chi^2 P + \chi RT - \alpha\kappa\right) + R^2T^2}{B} - RT\right) \tag{2-20a}$$

$$B = \sqrt[3]{\frac{\beta + \sqrt{\beta^2 - 4[3P(\chi^2 P + \chi RT - \alpha\kappa) + R^2T^2]^3}}{2}} \tag{2-20b}$$

$$\beta = -2R^3T^3 - 27\alpha\kappa\chi P^2 - 9RPT(\chi^2 P + \chi RT - \alpha\kappa) \tag{2-20c}$$

We can obtain the molecular number density (n) under the real gas effect:

$$n = \frac{N_A}{V_m} \tag{2-21}$$

The density (ρ) can be calculated in terms of n as follows:

$$\rho = \frac{Mn}{N_A} \tag{2-22}$$

We can obtain the expression of compressibility factor (Z) in terms of n as follows:

$$Z = \frac{P}{nkT} \tag{2-23}$$

The viscosity (μ) is obtained as follows (Jarrahian and Heidaryan, 2014):

$$\mu = \mu_0[1 + \frac{o_1}{{T_r}^5}\left(\frac{{P_r}^4}{{T_r}^{20}+{P_r}^4}\right) + o_2\left(\frac{P_r}{T_r}\right)^2 + o_3(\frac{P_r}{T_r})] \tag{2-24}$$

where μ_0 is the gas viscosity at P = 1.01325×105 Pa and T = 423 K, $= 2.31 \times 10^{-5}\ Pa \cdot s$; P_r is the reduced pressure, dimensionless, $= \frac{P}{P_c}$; o_1, o_2 and o_3 are the fitting coefficients, $o_1 = 7.9$, $o_2 = 9 \times 10^{-6}$, $o_3 = 0.28$.

2.2.4 Model Description

To date, we have improved the modelling of real gas transport in nanopores of shale rocks. Tapered non-circular nanopore structure and real gas EOS are the tie bridging the connection between real gas effect, molecular kinetics and transport behavior.

For bulk gas transport in the region surrounded by the adsorbed layer, viscous flow and Knudsen diffusion coexists. We adopt the approach of linear superposition of viscous flow and Knudsen diffusion for free gas, which has been well validated with simulation and experimental data of free gas in previous studies.Thus the molar rate for the free gas transport in single nanopores (q_b) is calculated as Equation (2-25):

$$q_b = q_v + q_k \tag{2-25}$$

where q_b is the molar rate for bulk gas transport in single nanopores, mol/s.

For the adsorbed gas transport in the adsorbed layer, only surface diffusion exists. Thus the molar rate for the adsorbed gas transport in single nanopores (q_a) is calculated as follows:

$$q_a = q_s \tag{2-26}$$

where q_a is the molar rate for adsorbed gas transport, mol/s.

Together with the viscous flow and Knudsen diffusion, the total flow molar rate for the gas is as follows:

$$q_t = q_b + q_a \tag{2-27}$$

where q_t is the total molar rate for gas transport in single nanopores, mol/s.

By dividing both sides by the pressure gradient for Equation (2-26), the total conductance of free gas is calculated as Equation (2-28). The conductance of adsorbed gas transport (c_a) and the total conductance of gas transport (c_t) in single nanopores are calculated as Equations (2-29) and (2-30):

$$c_b = c_v + c_k \tag{2-28}$$

$$c_a = c_s \tag{2-29}$$

$$c_t = c_a + c_b \tag{2-30}$$

where c_b is the conductance for bulk gas transport in single nanopores, $(mol \cdot m)/(Pa \cdot s)$; c_a is the conductance for adsorbed gas transport in single nanopores, $(mol \cdot m)/(Pa \cdot s)$; c_t is the total conductance for gas transport in single nanopores, $(mol \cdot m)/(Pa \cdot s)$;

If we fix the gas compressibility factor as 1, we can obtain the molar rate in single nanopores for viscous flow, Knudsen diffusion, surface diffusion, adsorbed gas transport, bulk gas transport and total gas transport with ideal gas law as q_{vi}, q_{ki}, q_{si}, q_{ai}, q_{bi} and q_{ti}.

2.3 Model Validation

We validate the proposed model with the data from experiments and simulations over a wide range of pressure. We firstly validate the model with the experimental data from Yamaguchi et al. under low pressure in 2011 (Yamaguchi et al., 2011) and Ewart et al. under high pressure in 2007 (Ewart et al., 2007). In Yamaguchi et al.'s experiment, the nitrogen is tested the transport rate in a microtube with the diameter of 25.27 um and the length of 5.3 cm. The experiment from Ewart et al. is performed in the microtube with the diameter of 320 um and the length of 5.925 cm. The dimensionless molar flow rate (q_D) is determined in the experiments as follows (Yamaguchi et al., 2011; Ewart et al., 2007):

$$q_D = \frac{c_t}{c_v} \tag{2-31}$$

where q_D is the dimensionless molar rate for gas transport in single nanopores, dimensionless.

An excellent match between the model and experiment is shown in Figure 2-2, which confirms that the model has the adaptability for a low pressure range.

We then validate the model under different high pressures based on the simulation results presented by Landry et al. (Landry et al., 2016). The methane is selected for the simulation in a nanopore with pore radius of 4.223 nm in case 1 and pore radius of 2.585 nm in case 2. The comparison with the simulation data is shown as Figure 2-3, which shows excellent match under the high pressure.

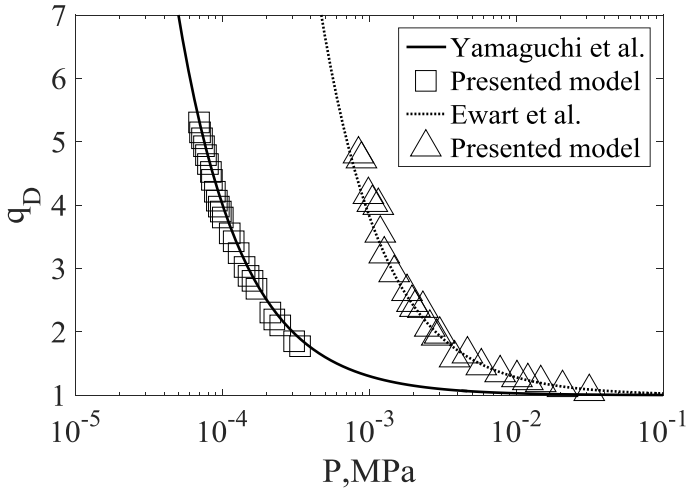

Figure 2-2 Validation with experimental data reported by Yamaguchi et al. and Edwart et al.，(Ewart et al.'s experiment: $T = 298\,K$, $= 1$, $\tau = 1$, $b_{\text{in}} = 25.27\,um$, $\xi_E = 1$ and $\gamma_E = 1$; Yamguchi et al.'s experiment: $T = 293\,K$, $= 1$, $\tau = 1$, $b_{\text{in}} = 320\,um$, $\xi_E = 1$ and $\gamma_E = 1$).

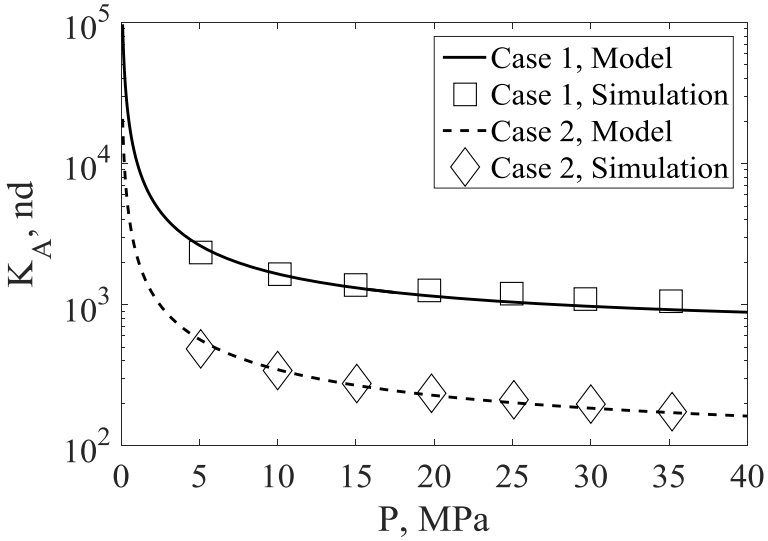

Figure 2-3 Validation with simulation data reported by Landry et al., Case 1: $T = 400$ K, $\phi = 0.5832$， $b_{in} = 8.45$ nm, $\tau = 2.9$, $\xi_E = 1$ and $\gamma_E = 1$; Case 2: $T = 400$ K, $\phi = 0.1963$， $b_{in} = 5.17$ nm, $\tau = 2.8$, $\xi_E = 1$ and $\gamma_E = 1$.

2.4 Results and Discussions

In this part, the transport behavior of real gas in tapered non-circular nanopores is investigated and analyzed based on the developed model.

2.4.1 Real Gas Effect

In order to better understand the proposed model in this thesis, three latest models (Sheng et al. in 2015, Ren et al. in 2016 and Wu et al. in 2016) are selected for the comparison (Figure 2-4). As these models cannot be applied into non-circular tapered nanopores, we simply consider the transport of the methane in a straight circular nanopore. The molecular attraction is neglected in Wu et al. model, which causes the compressibility factor is always larger than that obtained from the real gas EOS. Overestimated compressibility factor produces a lower gas density which further decreases the viscous flow conductance (c_v). Overestimated compressibility factor also brings a lower gas coverage and makes the surface diffusion conductance (c_s) smaller. As the Knudsen diffusion conductance (c_k) is inversely proportional to the compressibility factor, the exaggerated compressibility factor leads to the underestimation of c_k. Thus the total conductance (c_t) obtained from Wu et al. model is always lower than that from the present model. In Sheng et al. model, the compressibility factor is regarded as 1 without considering the real gas effect. Thus the total conductance estimated by Sheng et al. model is underestimated in case of the low pressure, and vice versa in case of the high pressure. The total conductance predicted by Ren et al. model is the smallest due to the neglect of surface diffusion.

The real gas effect is further investigated in tapered non-circular nanopores. Figure 2-5 indicates the impact of the real gas effect on the free gas transport (Knudsen diffusion and viscous flow) is greater than that on the adsorbed gas transport (surface diffusion). This is because the real

gas effect affects the surface diffusion by the adsorption capacity, but such effect can be negligible (Wu et al., 2015). Thus the free gas transport is more subject to being influence by the real gas effect compared with the adsorbed gas transport. That is, the real gas effect mainly affects the gas transport in nanopores through influencing the free gas transport. Increasing taper ratio and aspect ratio weakens the real gas effect (Figure 2-5**)** as the free gas transport ratio decreases (Figure 2-6). Figure 2-7 (a) indicates the tapered circular nanopore is most influenced by the real gas effect, followed by tapered square, elliptical and rectangular nanopores with aspect ratio of 2; this is because the tapered circular nanopore owns the largest free gas transport ratio Figure 2-7 (b), which is most sensitive to the real gas effect.

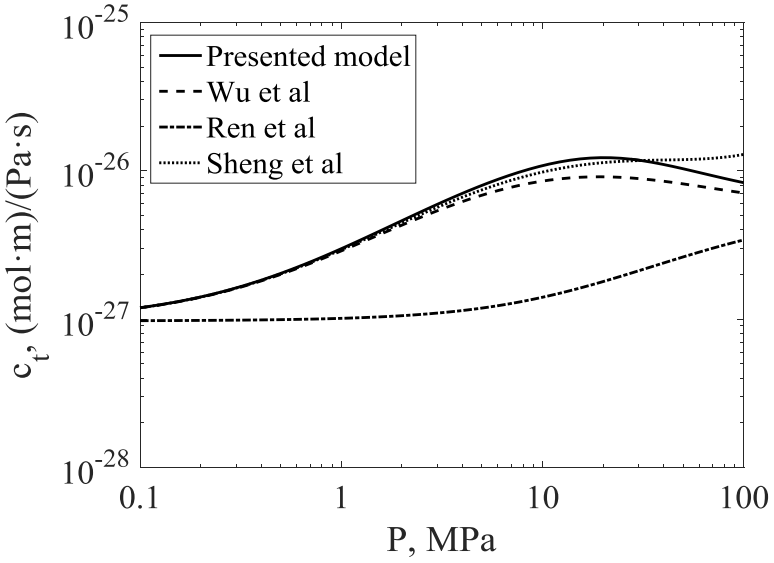

Figure 2-4 Comparison of present model with other models, $T = 330$ K, $\phi = 0.09$, $\tau = 2$, $b_{in} = 7$ nm, $\xi_E = 1$ and $\gamma_E = 1$.

2.4.2 Effects of Tapered Non-circular Nanopore Structure

The transport behavior is further discussed with focus on the tapered non-circular nanopore structure. Effects of taper ratio and aspect ratio on the transport conductance under the constant mean cross-sectional area and pressure are shown in Figures 2-8. With the increasing taper ratio and aspect ratio, the Knudsen diffusion and viscous flow conductance keep decreasing. Considering the Knudsen diffusion and viscous flow only exist in free gas, this trend is mainly due to the decrease of pore volume of free gas as indicated by the effective porosity of free gas (ϕ_b) in Figure 2-9. The surface diffusion conductance firstly increases and decreases afterwards with the increase in taper ratio; this is because the $\phi_a G_s$ firstly increases and then decreases (Wu et al., 2015). Compared with the adsorbed gas transport, the higher bulk gas transport ratio under the lower taper ratio and aspect ratio yields to a higher apparent permeability (Figure 2-10**)**. Thus the bulk gas transport contributes more to the transport capacity compared with the adsorbed gas transport.

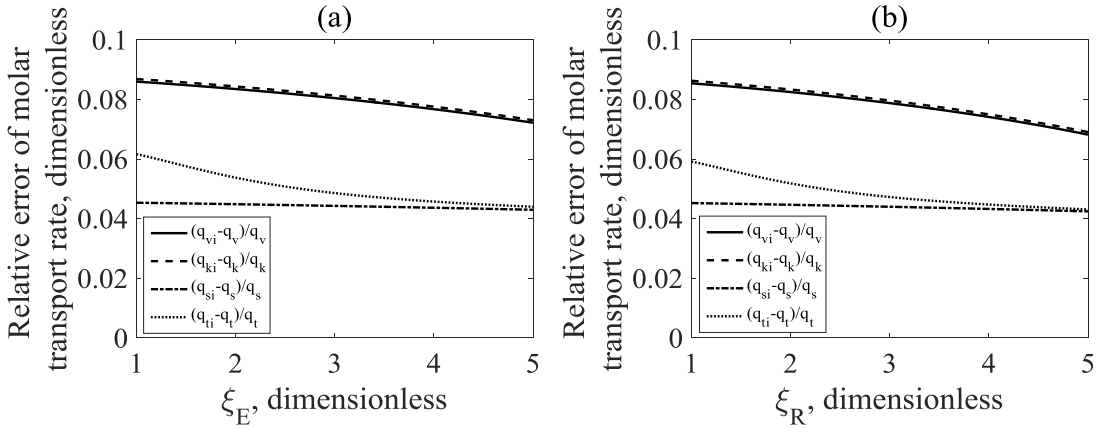

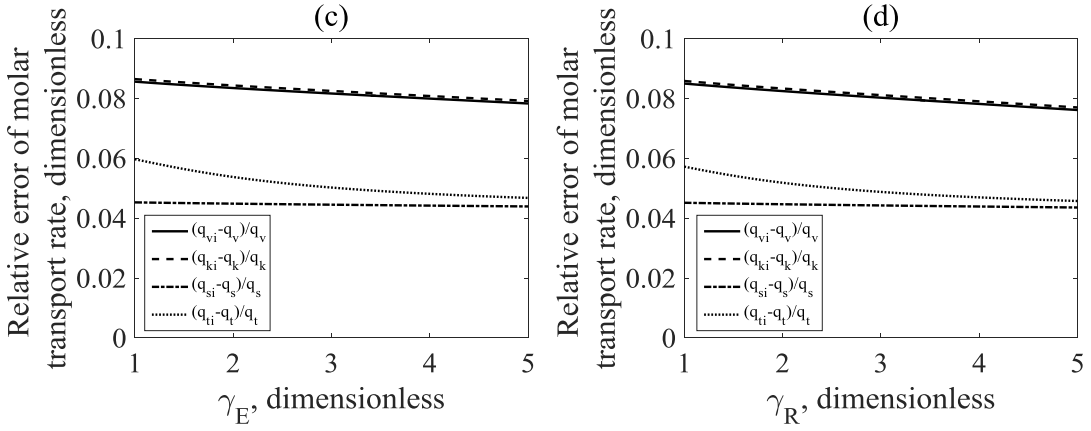

Figure 2-5 Sensitivity of gas transport rate to real gas effect (a. tapered elliptical nanopore, $\gamma_E = 3$; b. tapered rectangular nanopore, $\gamma_R = 3$; c. tapered elliptical nanopore, $\xi_E = 3$; d. tapered rectangular nanopore, $\xi_R = 3$), $T = 330\ K$, $P = 40\ MPa$ $\phi = 0.09$, $\tau = 2$ and $\bar{A} = 50\ nm^2$.

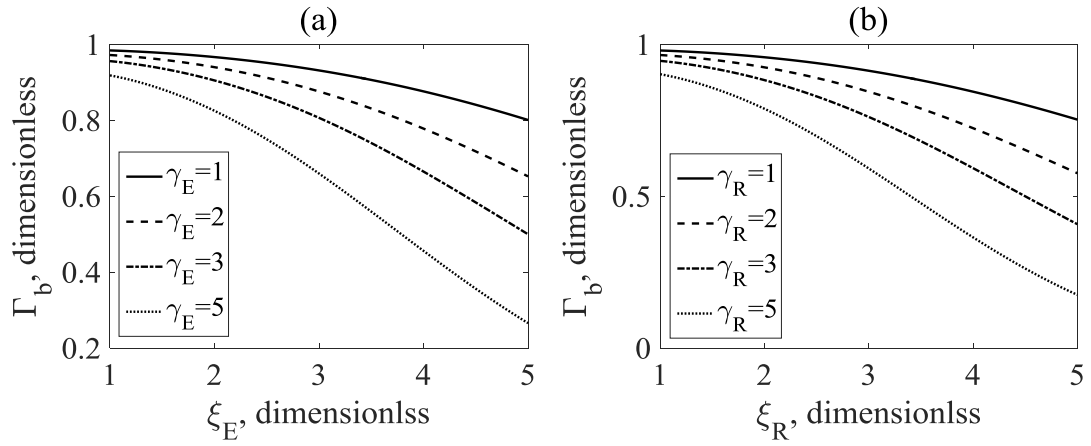

Figure 2-6 Effects of tapered non-circular nanopore structure on the bulk gas and adsorbed gas transport ratios (a and c. tapered elliptical nanopore; b and d. tapered rectangular nanopore), $T = 330$ K, $P = 40$ MPa, $\phi = 0.09$, $\tau = 2$ and $\bar{A} = 50$ nm^2.

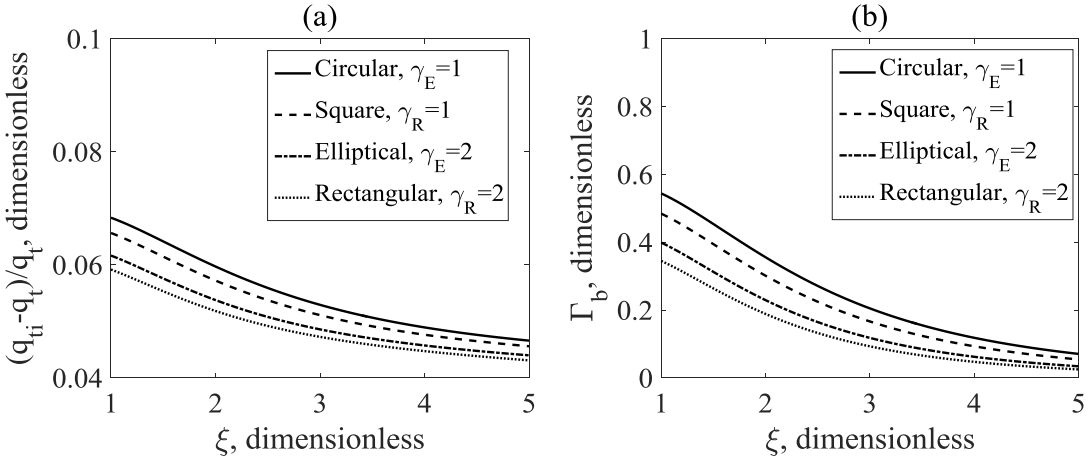

Figure 2-7 Sensitivity of pore shape to real gas transport, $T = 330\ K$, $P = 40\ MPa$ $\phi = 0.09$, $\tau = 2$ and $\bar{A} = 50\ nm^2$.

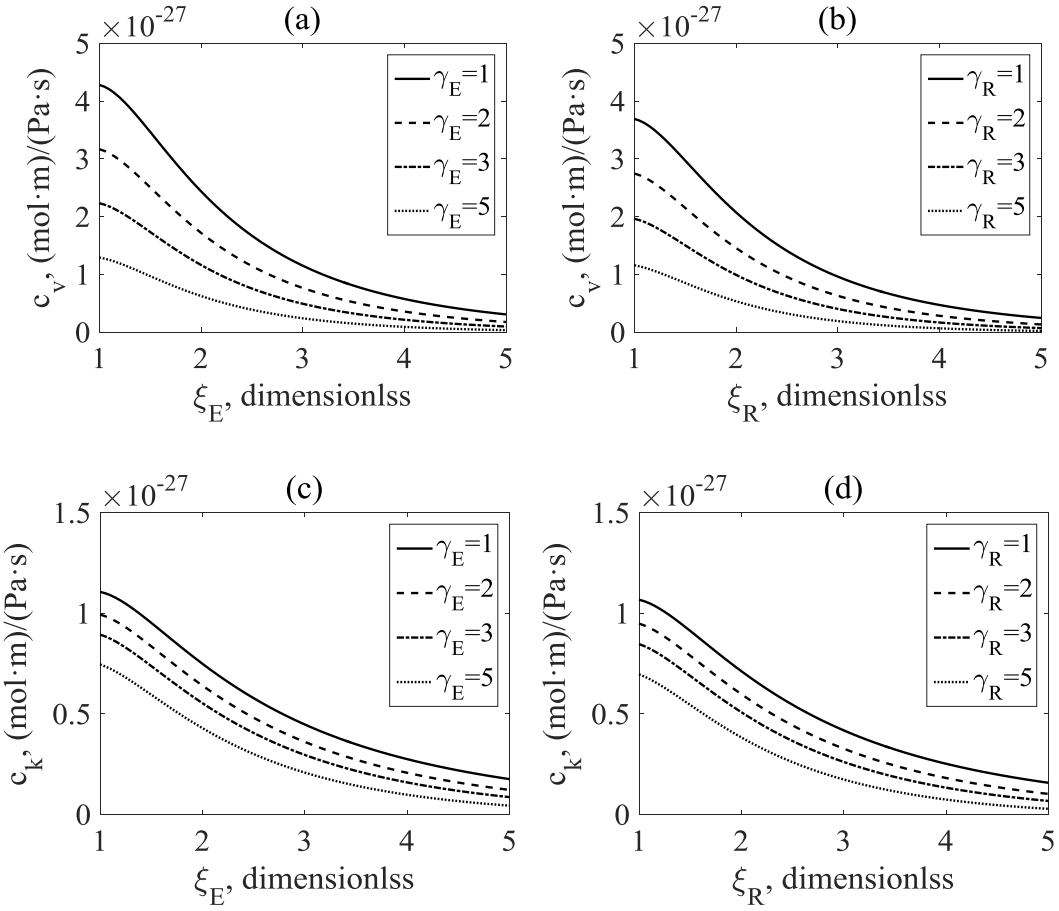

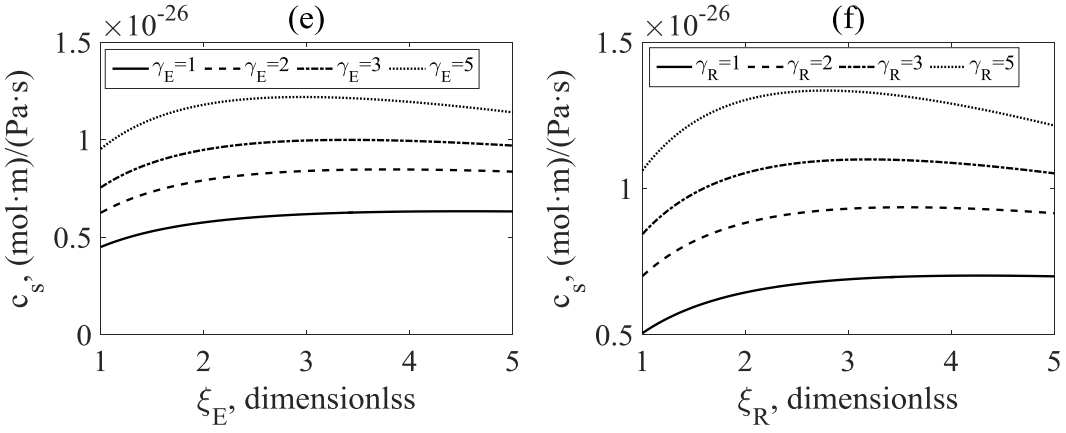

Figure 2-8 Effects of tapered non-circular nanopore structure on the transport conductance (a, c, e: tapered elliptical nanopore; b, d, f: tapered rectangular nanopore), $T = 330\ K$, $P = 40\ MPa$, $\phi = 0.09$, $\tau = 2$ and $\bar{A} = 50\ nm^2$.

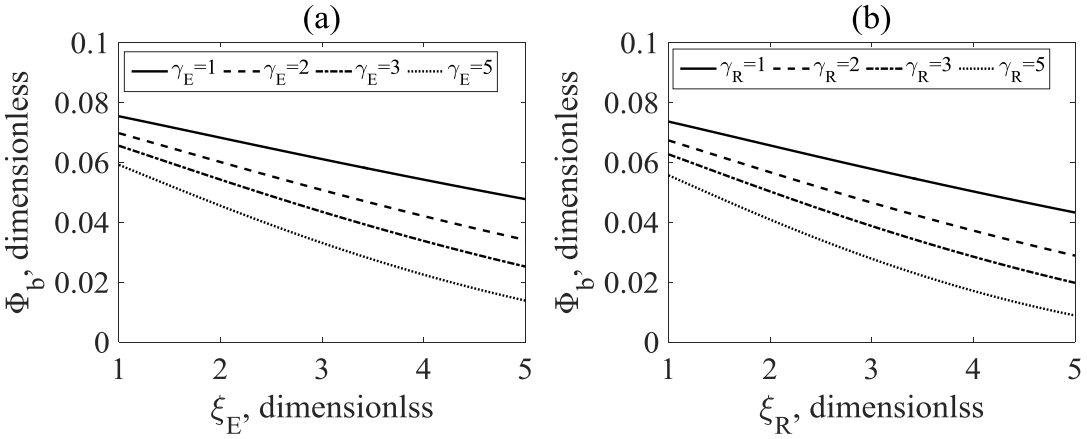

Figure 2-9 Effects of tapered non-circular nanopore structure on the effective porosity for bulk gas transport (a. tapered elliptical nanopore; b. tapered rectangular nanopore), $T = 330\ K$, $P = 40\ MPa$, $\phi = 0.07$, $\tau = 2$ and $\bar{A} = 50\ nm^2$.

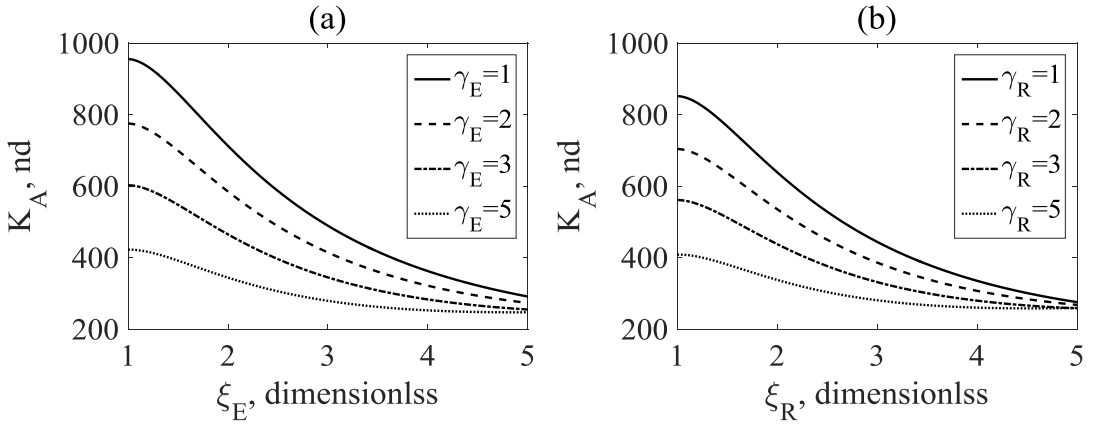

Figure 2-10 Effects of tapered non-circular nanopore structure on apparent permeability, $T = 330\ K$, $P = 40\ MPa$, $\phi = 0.07$, $\tau = 2$ and $\bar{A} = 50\ nm^2$.

2.4.3 Transport Regime Analysis

On the basis of previous discussion, the dominant transport mechanism under different condition is further explored. We define the dominant transport mechanism as the one with the highest molar rate ratio. Three regions are divided based on the dominant transport region by pressure and mean cross-sectional area: (1) region 1: domination of surface diffusion; (2) region 2: domination of Knudsen diffusion; (3) region 3: domination of viscous flow. The transport regime map in Figure 2-11 indicates: (1) If mean cross-sectional area is less than 100 nm^2, the surface diffusion dominates; (2) If mean cross-sectional area is between 100 and 1000 nm^2, the viscous flow dominates in the pressure greater than 10 MPa, the surface diffusion dominates in the pressure range between 1 MPa and 10 MPa, and the Knudsen diffusion dominates in the pressure lower than 1 MPa; (3) If mean cross-sectional area ranges between 1000 nm^2 and 10^5 nm^2, the viscous flow dominates under the pressure greater than 5 MPa, while the Knudsen diffusion dominates under the pressure lower than 5 MPa; (4) If mean cross-sectional area is larger than 10^5

nm^2, viscous flow dominates. In the free gas dominated region, the Knudsen diffusion mainly dominates in the low pressure and medium mean cross-sectional area region, which is because the molecular-wall collision dominates under low pressure and small pore size. With the increase of the pressure and mean-cross sectional area, the intermolecular collision gradually dominates and results in the domination of the viscous flow. As shown in Figure 2-12, the apparent permeability in the surface diffusion-dominated regime is the lowest. Once the Knudsen diffusion or viscous flow-dominated regime is reached, the apparent permeability increases. This is in agreement with the conclusion obtained in subsection 4.2: the transport capacity is greater with a higher bulk gas transport ratio. Figure 16 also indicates the apparent permeability can be an indicator to predict the transport regime: (1) If the apparent permeability is larger than 10^5 nd, the viscous flow dominates in the nanopores; (2) If the apparent permeability ranges from 10^4 nd to 10^5 nd, the viscous flow dominates in the high pressure region and the Knudsen diffusion dominates in the low pressure region; (4) If the apparent permeability is lower than 10^4 nd, the surface diffusion mainly dominates in the region with small cross-sectional area. Thus, the viscous flow is significant for nanopores with high apparent permeability ($>10^5$ nd). Figure 2-13 shows effects of taper ratio and aspect ratio on the dominant transport regimes. With increasing taper ratio and aspect ratio, the surface diffusion-dominated region enlarges, the viscous flow-dominated region shrinks, and the Knudsen diffusion regime moves towards the higher mean cross-sectional area range. This is in agreement with the conclusion in subsection 2.4.1: increasing taper ratio and aspect ratio increases adsorbed gas transport ratio and decreases free gas transport ratio.

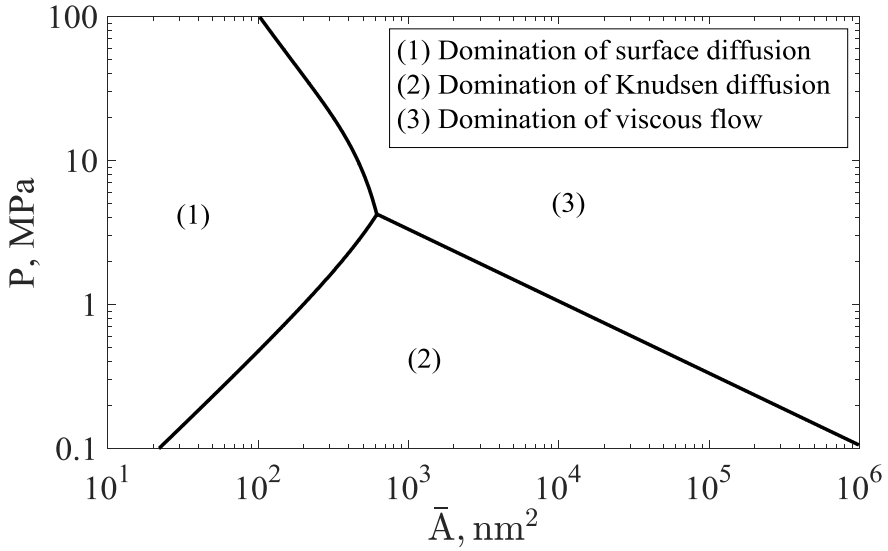

Figure 2-11 Transport regime map, $T = 330\ K$, $\phi = 0.09$, $\tau = 2$, $\xi_E = 2$ and $\gamma_E = 2$.

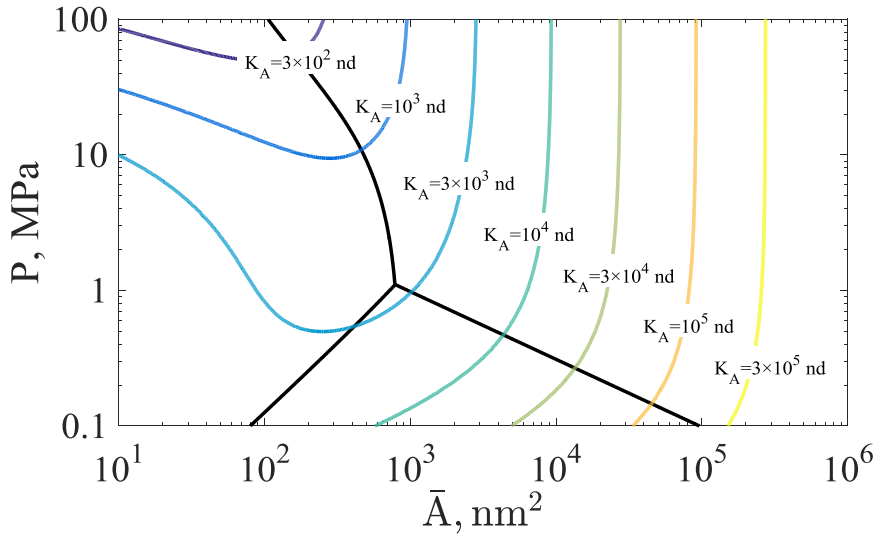

Figure 2-12 Apparent permeability contour map, $T = 330\ K$, $\phi = 0.09$, $\tau = 2$, $\xi_E = 2$ and $\gamma_E = 2$.

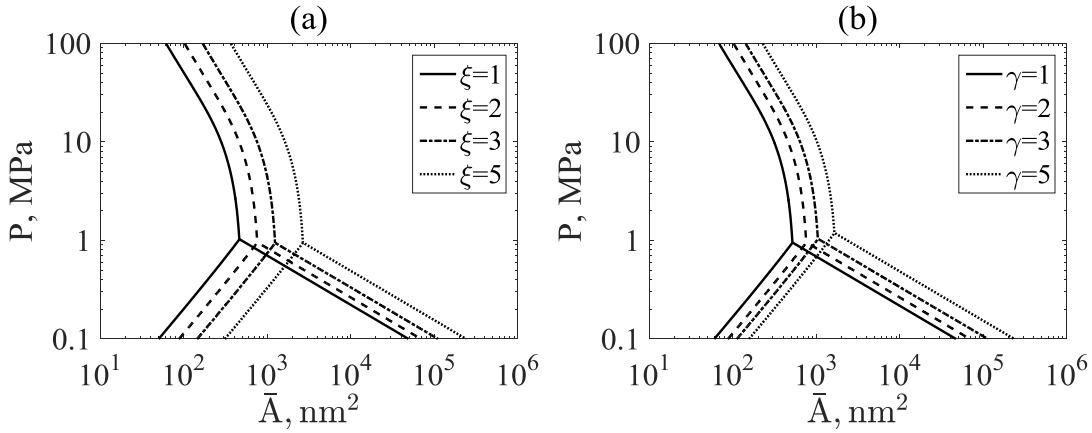

Figure 2-13 Effects of tapered non-circular nanopore structure on dominant transport regimes, $T = 330\ K$, $\phi = 0.09$, $\tau = 2$, $\gamma_E = 2$ in a and $\xi_E = 2$ in b.

2.5 Conclusion

An improved gas transport model has been built in this study, which bridges the real gas effect, molecular kinetics and transport behavior in the tapered non-circular nanopore. Validations of six kinds of gases based on experiments and molecular simulations show the reliability and practicability of the present model. Main conclusions are as follows:

(1) The real gas effect of the present model has been validated under high temperatures and pressures. Further comparison with previous models shows real gas EOS must be coupled. Compared with adsorbed gas, the free gas transport (Knudsen diffusion and viscous flow) is most influenced by real gas effect. Real gas effect mainly affects the gas transport in nanopores through influencing the free gas transport. Owing to the highest free gas transport ratio, the tapered circular nanopore is most sensitive to the real gas effect, followed by tapered square, elliptical and rectangular nanopores with aspect ratio of 2. Increasing taper ratio and aspect ratio weakens the real gas effect on gas transport.

(2) With the increase of taper ratio and aspect ratio under the constant mean cross-sectional area, conductance of Knudsen diffusion and viscous flow reduce, and the surface diffusion conductance firstly increase and decrease afterwards. Increasing taper ratio and aspect ratio shrinks the pore volume occupied by free gas, and decreases the free gas transport ratio, thus lowers the transport capacity of the nanopore.

(3) With the mean cross-sectional area lower than 100 nm^2, the surface diffusion dominates. When the mean cross-sectional area ranges from 100 nm^2 to 1000 nm^2, the Knudsen diffusion, surface diffusion and viscous flow dominate in the low, middle and high pressure range, respectively. If the mean cross-sectional area is between 1000 nm^2 and 10^5 nm^2, viscous flow dominates in the pressure greater than 5 MPa while Knudsen diffusion dominates in the pressure lower than 5 MPa. Supposing the mean cross-sectional area is larger than 10^5 nm^2, viscous flow dominates. The apparent permeability can be an indicator to predict the transport regime. The apparent permeability that is greater than 10^5 nd implies the viscous flow dominates. With increasing mean cross-sectional area, free gas transport gradually dominates, which increases the transport capacity indicated by the apparent permeability. Increasing taper ratio and aspect ratio reduces the transport capacity of nanopores by shrinking the free gas -dominated region.

Chapter Three: Effects of Shale Matrix on Gas Transport in Fractal Dual-porosity Shale Rocks

3.1 Introduction

In Chapter 2, we established a model to study gas transport in tapered non-circular nanopores of shale rocks. This model can serve the study of gas transport mechanisms in single nanopores, however it is limited to study the gas flow in shale matrix with a bundle of pores. Shale matrix owns a complex pore structure with a wide range of pore size distribution. According to the experimental results reported by Chalmers et al. (2012), Utpalendu and Prasad (2013) and Wu et al. (2017), the shale matrix owns a wide range of pore size distribution which can be from 1 nm to 100 um. As shown in Figure 2-11, the gas transport regime is dependent on the cross-sectional area of pores which are determined by pore sizes. Thus to propose a model which can be applied in the study of gas transport in a bundle of pores in shale matrix is very important. We have reviewed previous models on shale gas transport in nanopores in Chapter 2, and these models are limited to describe the shale gas transport in a bundle of pores.

In fact, except for shale matrix, the natural fracture is also a very important structure in dual-porosity shale rocks. Fracture aperture is an important parameter affecting the gas transport mechanisms in natural fractures of shale rocks. A wide range of fracture aperture size is also reported by previous studies (Wu et al., 2015), and the range of fracture aperture must be considered in studying the gas transport mechanisms in shale rocks. Different sizes of apertures lead to different apparent permeability of natural fractures. However, previous model are mainly focused on the single fractures. Wu et al. (2015) proposed a model to study gas transport in microfractures. They indicated the gas transport efficiency is significantly affected by micofracture

shape and size. Akkutlu et al. (2017) studied the gas transport in a coupled discrete fracture and dual-continuum porous media. In their study, they developed a multiscale simulation workflow for gas transport in shale rocks.

Fractal theory has been an effective method to describe pore size distribution in shale rocks. According to Clarkson et al. (2012)'s experiment on shale gas plays (Barnett, Marcellus, Haynesville, Eagle Ford, Woodford, Muskwa and Duvernay shale), the fractal theory can be applied to describe the real pore size distribution. Some scholars applied the fractal theory to model the fluid transport in rocks. Xu et al. (2013) studied the relative permeability in unsaturated porous media. They found that pore size distribution affected the multiphase flow in porous media. Miao et al. (2015) proposed a fractal model for permeability of fractured rocks. They claimed that the pore size distribution based on fractal theory can significantly affect the fluid transport efficiency of fractured rocks. Miao et al. (2015) presented an analytical model in another study to research on the permeability of dual-porosity media. Their model indicated that the permeability of dual-porosity media is influenced by fractal dimensions and structural parameters. Yang et al. (2017) applied the fractal theory to study the flow resistance in microchannels. They showed that the decrease of the permeability is affected by the fractal geometry. However, a model to describe the gas transport in dual-porosity shale rocks is still in need to be explored. In this study, we build a model for gas transport in dual-porosity shale rocks, and apply it to describe shale gas transport. The effect of shale matrix on gas transport in dual-porosity shale rocks is especially discussed in the results and discussions.

3.2 Model Establishment

The dual-porosity shale rock in this study is composed of a bundle of pores and rectangular fractures. We assume that the pores and fractures cut through the model. The pores exist in the shale matrix. The free gas transport in both fracture and pores, and the adsorbed gas only transports in pores. Two transport mechanisms of viscous flow and Knudsen diffusion are considered in free gas, and the gas transport mechanism of surface diffusion is considered in adsorbed gas.

3.2.1 Pore size/ fracture aperture distribution

For the dual-porosity shale rocks, the total number of pores (N_p) and fractures (N_f) are calculated as follows (Yu and Li, 2001):

$$N_p = (\frac{d_{pmax}}{d_p})^{D_p} \tag{3-1a}$$

$$N_f = (\frac{\sigma_{max}}{\sigma})^{D_f} \tag{3-1b}$$

where N_p is the total number of pores with their equivalent pore diameter larger than d_p; N_f is the total number of fractures with the aperture larger than σ, dimensionless; σ is the fracture aperture, m; d_p is the equivalent diameter of pores, m; d_{pmax} is the maximum equivalent diameter of pores, m; σ_{max} is the maximum fracture aperture, m.

Let $d_p = d_{pmin}$ and $\sigma = \sigma_{min}$, expressions of the total number of pores (N_{pt}) and the total number of fractures (N_{ft}) are obtained as follows:

$$N_{pt} = (\frac{d_{pmax}}{d_{pmin}})^{D_p} \tag{3-2a}$$

$$N_{ft} = (\frac{d_{pmax}}{\sigma_{min}})^{D_p} \tag{3-2b}$$

where N_{pt} is the total number of pores, dimensionless; N_{ft} is the total number of fractures, dimensionless; d_{pmin} is the minimum pore size; σ_{min} is the minimum fracture aperture.

We do the differentiation on Equation (3-2) for both sides, and the following equations are obtained:

$$-\frac{dN_p}{N_{pt}} = D_p {d_{pmin}}^{D_p} \, {d_p}^{-(D_p+1)} \mathrm{d}(d_p) = f_p \mathrm{d}(d_p) \tag{3-3a}$$

$$-\frac{dN_f}{N_{ft}} = D_f {\sigma_{min}}^{D_f} \, \sigma^{-(D_f+1)} \mathrm{d}(\sigma) = f_f \mathrm{d}(\sigma) \tag{3-3b}$$

where f_p is the probability density function of pore size; f_f is the probability density function of fracture aperture.

The cumulative probabilities of pores (F_p) and fractures (F_f) are thus obtained as follows:

$$F_p = 1 - \left(\frac{d_{pmin}}{d_p}\right)^{D_p} \tag{3-4a}$$

$$F_f = 1 - \left(\frac{d_{pmin}}{d_p}\right)^{D_p} \tag{3-4b}$$

where F_p is the cumulative probability of pores; F_f is the cumulative probability of fractures.

3.2.2 Gas Transport in Shale Matrix

Three kinds of gas transport mechanisms (viscous flow, Knudsen diffusion and surface diffusion) exist in shale matrix. Viscous flow and Knudsen diffusion co-exist in the free gas phase, and surface diffusion exists in the adsorbed gas phase. The viscous flow is dominated by intermolecular collision, and the Knudsen diffusion is dominated by molecule-wall collision. The adsorbed gas occurs on the wall of pores, during which the adsorbed gas molecules jump from one adsorption site to another. We consider the single adsorbed layer in this study.

Expressions of transport rates of viscous flow, Knudsen diffusion and surface diffusion in single pores are shown as follows (Xu et al., 2017; Xu et al., 2018):

$$q_{vm} = \frac{3\xi^3\left(\frac{2\xi^2}{\xi+1}\right)^{-\frac{4}{3}}}{(\xi^2+\xi+1)}\frac{\pi\rho\phi_{mb}{d_p}^4}{128\mu M}\frac{\Delta P}{L_p} \tag{3-5a}$$

$$q_{km} = \frac{\pi\phi_{mb}\bar{v}{d_p}^3}{12ZRT}\frac{\Delta P}{L_p} \tag{3-5b}$$

$$q_{sm} = \xi\left(\frac{2\xi^2}{\xi+1}\right)^{-\frac{2}{3}}\frac{\theta\phi_{ma}\mathfrak{D}_s{d_p}^2}{N_A{d_m}^3 P}\frac{\Delta P}{L_p} \tag{3-5c}$$

where M is the molecular weight, kg/mol; ϕ_b is the effective porosity for free gas transport, dimensionless; $\mathfrak{D}_s$ is the surface diffusion coefficient, m^2/s; ρ is the gas density, kg/m^3; ξ is the taper ratio, dimensionless; P is pressure, Pa; L_t is the tortuous length of pores, m, $= L^{D_\tau}{d_p}^{1-D_\tau}$; Z is the gas compressibility factor, dimensionless; d_m is the molecular diameter, m; μ is the gas viscosity, $Pa \cdot s$; ϕ_{ma} is the effective porosity for adsorbed gas transport, dimensionless; D_τ is the fractal dimension of the tortuosity of pores, dimensionless; θ is the gas coverage, dimensionless.

The fractal theory is the bridge between the gas transport in single pores and that in a bundle of pores. The transport rates of viscous flow, Knudsen diffusion and surface diffusion are expressed as follows:

$$Q_{vm} = -\int_{d_{pmin}}^{d_{pmax}} q_{vm}\, dN_p \tag{3-6a}$$

$$Q_{km} = -\int_{d_{pmin}}^{d_{pmax}} q_{km}\, dN_p \tag{3-6b}$$

$$Q_{sm} = -\int_{d_{pmin}}^{d_{pmax}} q_{sm}\, dN_p \tag{3-6c}$$

where q_{vm} is the viscous flow molar rate in a single pore in shale matrix, mol/s; Q_{vm} is the total viscous flow molar rate in shale matrix, mol/s; q_{km} is the Knudsen diffusion molar rate in a single

pore in shale matrix, mol/s; Q_{km} is the total Knudsen diffusion molar rate in shale matrix, mol/s; q_{sm} is the surface diffusion molar rate in a single pore in shale matrix, mol/s; Q_{sm} is the total surface diffusion molar rate in shale matrix, mol/s.

By coupling Equations (3-5) and (3-6), we can obtain Q_{vm}, Q_{km} and Q_{sm} as follows:

$$Q_{vm} = \frac{D_p(1-{\eta_p}^{3-D_p+D_{\tau p}})}{3-D_p+D_\tau} \frac{3\varepsilon^3\left(\frac{2\varepsilon^2}{\varepsilon+1}\right)^{-\frac{4}{3}}}{\varepsilon^2+\varepsilon+1} \frac{\pi\phi_{mb}\rho {d_{pmax}}^{3+D_{\tau p}}}{128\mu M L^{D_\tau-1}} \frac{\Delta P}{L} \tag{3-7a}$$

$$Q_{km} = \frac{D_p(1-{\eta_p}^{2-D_p+D_{\tau p}})}{2-D_p+D_\tau} \frac{\pi\phi_{mb}\bar{v} {d_{pmax}}^{2+D_{\tau p}}}{12ZRTL^{D_\tau-1}} \frac{\Delta P}{L} \tag{3-7b}$$

$$Q_{sm} = \frac{D_p(1-{\eta_p}^{1-D_p+D_{\tau p}})}{1-D_p+D_\tau} \varepsilon \left(\frac{2\varepsilon^2}{\varepsilon+1}\right)^{-\frac{2}{3}} \frac{\phi_{ma}\theta\mathfrak{D}_s {d_{pmax}}^{1+D_{\tau p}}}{N_A {d_m}^3 PL^{D_\tau-1}} \frac{\Delta P}{L} \tag{3-7c}$$

We adopt the linear superposition of different transport rates of gas transport mechanisms. Total gas transport rates of free gas, adsorbed gas and gas are thus calculated as follows:

$$Q_{bm} = Q_{vm} + Q_{km} \tag{3-8a}$$

$$Q_{am} = Q_{sm} \tag{3-8b}$$

$$Q_{tm} = Q_{am} + Q_{bm} \tag{3-8c}$$

where Q_{bm} is the free gas transport molar rate in shale matrix, mol/s; Q_{am} is the adsorbed gas transport molar rate in shale matrix, mol/s; Q_{tm} is the total gas transport molar rate in shale matrix, mol/s.

The viscous flow conductance (c_{vm}), Knudsen diffusion conductance (c_{km}), surface diffusion conductance (c_{sm}), adsorbed gas transport conductance (c_{am}), free gas transport conductance (c_{bm}), and total gas transport conductance (c_{tm}) in shale matrix are obtained as follows:

$$c_{vm} = \frac{D_p(1-{\eta_p}^{3-D_p+D_{\tau p}})}{3-D_p+D_\tau} \frac{3\varepsilon^3\left(\frac{2\varepsilon^2}{\varepsilon+1}\right)^{-\frac{4}{3}}}{\varepsilon^2+\varepsilon+1} \frac{\pi\phi_{mb}\rho {d_{pmax}}^{3+D_{\tau p}}}{128\mu M L^{D_\tau-1}} \tag{3-9a}$$

$$c_{km} = \frac{D_p(1-{\eta_p}^{2-D_p+D_{\tau p}})}{2-D_p+D_\tau} \frac{\pi\phi_{mb}\bar{v}{d_{pmax}}^{2+D_{\tau p}}}{12ZRTL^{D_\tau-1}} \tag{3-9b}$$

$$c_{sm} = \frac{D_p(1-{\eta_p}^{1-D_p+D_{\tau p}})}{1-D_p+D_\tau} \varepsilon \left(\frac{2\varepsilon^2}{\varepsilon+1}\right)^{-\frac{2}{3}} \frac{\phi_{ma}\theta\mathfrak{D}_s{d_{pmax}}^{1+D_{\tau p}}}{N_A{d_m}^3 PL^{D_\tau-1}} \tag{3-9c}$$

$$c_{am} = c_{sm} \tag{3-9d}$$

$$c_{bm} = c_{vm} + c_{km} \tag{3-9e}$$

$$c_{tm} = c_{am} + c_{bm} \tag{3-9f}$$

where c_{am} is the adsorbed gas transport conductance in shale matrix, $(mol \cdot m)/(Pa \cdot s)$; c_{km} is the Knudsen diffusion conductance in shale matrix, $(mol \cdot m)/(Pa \cdot s)$; c_{vm} is the viscous flow conductance in shale matrix, $(mol \cdot m)/(Pa \cdot s)$; c_{tm} is the total gas transport conductance in shale matrix, $(mol \cdot m)/(Pa \cdot s)$; c_{sm} is the surface diffusion conductance in shale matrix, $(mol \cdot m)/(Pa \cdot s)$; c_{bm} is the free gas transport conductance in shale matrix, $(mol \cdot m)/(Pa \cdot s)$.

3.2.3 Gas Transport in Natural Fractures

Considering that the adsorbed gas does not exist in natural fractures, mechanisms of Knudsen diffusion and viscous flow are taken into the modelling of gas transport in natural fractures. In order to construct the analytical model, we simply fractures as planes with rectangular cross sections. This simplification is also widely used in the research of fluid flow in fractures.

Expressions of transport rates of viscous flow (q_{vf}) and Knudsen diffusion (q_{kf}) are shown as follows (Lafferty, 1998):

$$q_{vf} = \frac{\pi\phi_f\rho}{64\mu M} I_{vf}\sigma^4 \frac{\Delta P}{L_f} \tag{3-10a}$$

$$q_{kf} = \frac{\phi_f\bar{v}\sigma^3}{4ZRT} I_{kf} \frac{\Delta P}{L_f} \tag{3-10b}$$

where I_{vf} is the geometric parameter of viscous flow in the fracture, $= \frac{1}{1+{\gamma_f}^2}$; q_{vf} is the viscous flow molar rate in a single fracture, mol/s; I_{kf} is the geometric parameter of Knudsen diffusion in the fracture, $= \gamma_f[\gamma_f \ln\left(\frac{1}{\gamma_f} + \frac{1}{\gamma_f}\sqrt{1+{\gamma_f}^2}\right) + \ln\left(\gamma_f + \sqrt{1+{\gamma_f}^2}\right) + \frac{1+{\gamma_f}^3-(1+{\gamma_f}^2)^{\frac{3}{2}}}{3\gamma_f}]$; q_{kf} is the Knudsen diffusion molar rate in a single fracture, mol/s.

Total gas transport rates of viscous flow (Q_{vf}) and Knudsen diffusion (Q_{vk}) in a bundle of pores are calculated as follows:

$$Q_{vf} = -\int_{\sigma_{min}}^{\sigma_{max}} q_{vf}\, dN_f \tag{3-11a}$$

$$Q_{kf} = -\int_{\sigma_{min}}^{\sigma_{max}} q_{kf}\, dN_f \tag{3-11b}$$

where Q_{kf} is the total Knudsen diffusion molar rate in fractures, mol/s; Q_{vf} is the total viscous flow molar rate in fractures, mol/s.

By coupling Equations (3-9) and (3-10), we can obtain Q_{vf} and Q_{kf} as follows:

$$Q_{vf} = \frac{\pi D_f \phi_f \rho (cos\beta_1)^{D_{\tau f}} (1-{\eta_f}^{3+D_{\tau f}-D_f})}{64\mu M L^{D_{\tau f}-1}(3+D_{\tau f}-D_f)} I_{vf} {\sigma_{max}}^{3+D_{\tau f}} \frac{\Delta P}{L} \tag{3-12a}$$

$$Q_{kf} = \frac{D_f \phi_f \bar{v} (cos\beta_1)^{D_{\tau f}} (1-{\eta_f}^{2+D_{\tau f}-D_f})}{4ZRTL^{D_{\tau f}-1}(2+D_{\tau f}-D_f)} I_{kf} \sigma_{max}^{2+D_{\tau f}} \frac{\Delta P}{L} \tag{3-12b}$$

The viscous flow conductance (c_{vf}), Knudsen diffusion conductance (c_{kf}), and total gas transport conductance (c_{tf}) in fractures are obtained as follows:

$$c_{vf} = \frac{\pi D_f \phi_f \rho (cos\beta_1)^{D_{\tau f}} (1-{\eta_f}^{3+D_{\tau f}-D_f})}{64\mu M L^{D_{\tau f}-1}(3+D_{\tau f}-D_f)} I_{vf} {\sigma_{max}}^{3+D_{\tau f}} \tag{3-13a}$$

$$c_{kf} = \frac{D_f \phi_f \bar{v} (cos\beta_1)^{D_{\tau f}} (1-\eta_f^{2+D_{\tau f}-D_f})}{4ZRTL^{D_{\tau f}-1}(2+D_{\tau f}-D_f)} I_{kf} \sigma_{max}^{2+D_{\tau f}} \tag{3-13b}$$

$$c_{tf} = c_{vf} + c_{kf} \tag{3-13c}$$

where c_{kf} is the total Knudsen diffusion conductance in fractures, $(mol \cdot m)/(Pa \cdot s)$; c_{vf} is the total viscous flow conductance in fractures, $(mol \cdot m)/(Pa \cdot s)$; c_{tf} is the total gas transport conductance in fractures, $(mol \cdot m)/(Pa \cdot s)$.

The total gas transport conductance in dual-porosity shale rock (Q_t) is thus calculated as follows (Zheng and Yu, 2012; Miao et al., 2015; Li et al., 2016):

$$Q_t = Q_{tf} + Q_{tm} \tag{3-14}$$

where Q_t is the total gas transport rate in dual-porosity shale rocks, mol/s.

The total conductance of gas transport in dual-porosity shale rocks (c_t) is obtained as follows:

$$c_t = c_{tf} + c_{tm} \tag{3-15}$$

where c_t is the total conductance in dual-porosity shale rocks, $(mol \cdot m)/(Pa \cdot s)$.

Based on the derivation in Chapter 2, the apparent permeability of dual-porosity shale rocks (K_A) is calculated as the following:

$$K_A = \frac{\mu M}{\rho A_t} c_t \tag{3-16}$$

where K_A is the apparent permeability of the dual-porosity shale rock, m^2.

3.3 Model Validation

In order to validate the practicability and accuracy of the model, we compared the model results with the experimental results reported by Zhu et al. (2016) and Ren et al. (2016) based on shale plug cores. In Zhu et al.'s experiment, the methane flows through a shale core plug with the length of 5 cm and the diameter of 2.5 meter. The flow rate is obtained in their experiment. In Ren et al.'s experiment, the flow test is conducted in a shale core plug with the diameter of 4 cm and the length of 8 cm. The flow rate is also measured in Ren et al.'s experiment. From Figure 3-1, we

can see that the total gas transport conductance from the model is in a good agreement with that from the experiment, which indicates the good practicability and accuracy of the proposed model. The validation also shows that the parallel flow exists in the core plug.

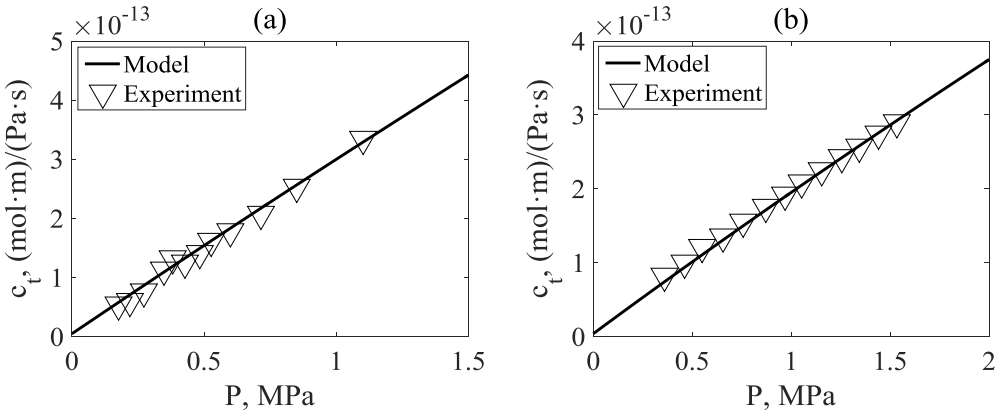

Figure 3-1 Validation of total gas transport conductance with experimental data of shale core plug ((a): experimental data of shale core plug reported by Zhu et al. (2016), $L = 5\ cm$, $r = 1.25\ cm$, $T = 300\ K$, $D_p = 2.98$, $D_f = 2.96$, $D_{\tau p} = 1.4$, $D_{\tau f} = 1.2$, $\phi_m = 0.12$, $\phi_f = 0.005$, $D_{pmax} = 30\ um$, $D_{pmin} = 0.8\ nm$, $\sigma_{max} = 130\ um$, $\sigma_{min} = 3.5\ um$, $\varepsilon = 1.2$, $\beta = 30°$ and $\gamma_f = 1.5$; (b): experimental data of shale core plug reported by Ren et al. (2016), $L = 8\ cm$, $r = 2\ cm$, $T = 333.15\ K$, $D_p = 2.96$, $D_f = 2.93$, $D_{\tau p} = 1.4$, $D_{\tau f} = 1.1$, $\phi_m = 0.11$, $\phi_f = 0.004$, $D_{pmax} = 45\ um$, $D_{pmin} = 1\ nm$, $\sigma_{max} = 100\ um$, $\sigma_{min} = 0.7\ um$, $\varepsilon = 1.1$, $\beta = 15°$ and $\gamma_f = 1.4$)

3.4 Results and Discussions

In the results and discussions section, the contribution of shale matrix to gas transport in dual-porosity shale rocks is firstly discussed, effect of the shale matrix on the total gas transport conductance is secondly explored, effect of the shale matrix on the gas transport efficiency of shale rocks is thirdly studied.

3.4.1 Contribution of Shale Matrix to Total Gas Transport

In order to better understand the role of shale matrix, we study on the contributions of natural fractures and shale matrix to total gas transport in dual-porosity shale rocks. We define the fracture/shale matrix dominant region as the one with the largest gas transport ratio. As shown in Figure 3-2, two transport regions are divided: (1) matrix-dominated region; (2) fracture-dominated region. Figure 3-2 indicates: (1) if the porosity of shale matrix is less than 0.05, the natural fracture dominates the flow while the fracture porosity is higher than 0.001; (2) if the porosity of shale matrix is between 0.05 and 0.1, the natural fracture is dominant while the fracture porosity is higher than 0.0015; (3) if the porosity of shale matrix is higher than 0.1, the the natural fracture dominates the flow with the fracture porosity higher than 0.002. Overall, if the fracture porosity is less than 0.0005, the shale matrix is the mian dominant media to provide the gas transport channel. Considering the fractal structure of dual-porosity shale rocks in our study, the effects of fractal dimensions of pore size (D_p) and tortuosity ($D_{\tau p}$) on gas transport region division are studied as shown in Figure 3-3. Figure 3-3(a) indicates decreasing D_p expands shale matrix-dominated region, indicating that the less complex the pores are presented by a smaller D_p, the weaker the dominancy of the shale matrix is. For instance, if the porosity of shale matrix is higher than 0.1, the conditions for the dominancy of fractures are: (1) the porosity of fracture is higher than 0.002 when $D_p = 2.9$; (2) the porosity of fracture is higher than 0.0015 when $D_p = 2.94$; (3) the porosity of fracture is higher than 0.001 when $D_p = 2.98$. Figure 3-3(b) shows that increasing $D_{\tau p}$ shrinks matrix-dominated region, indicating that the more tortuous the pores are presented by a larger $D_{\tau p}$, the weaker the dominancy of the shale matrix is due to a longer flowing path.

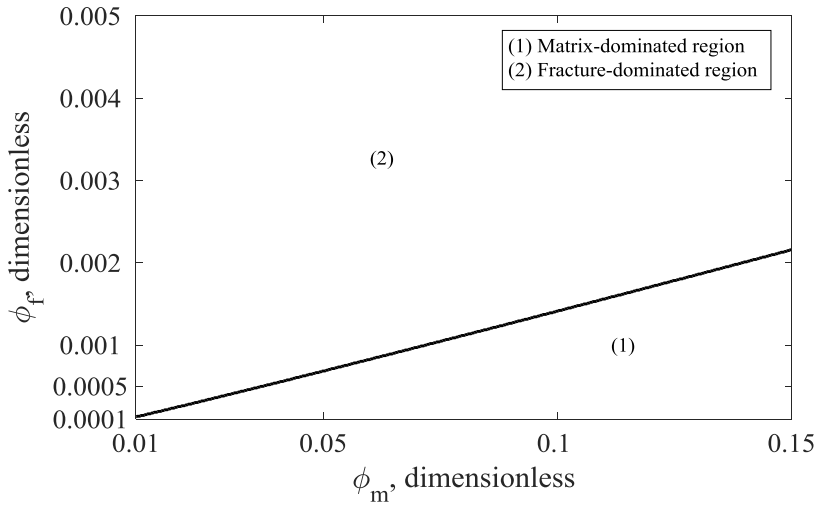

Figure 3-2 Regime of gas transport. $L = 3\ cm$, $A_t = 5\ cm^2$, $P = 25\ MPa$, $T = 350\ K$, $D_f = 2.9$, $D_p = 2.9$, $D_{\tau p} = 1.4$, $D_{\tau f} = 1.1$, $\phi_m = 0.1$, $\sigma_{min} = 1\ um$, $d_{pmin} = 1\ nm$, $\varepsilon = 1.2$, $\beta = 30°$.

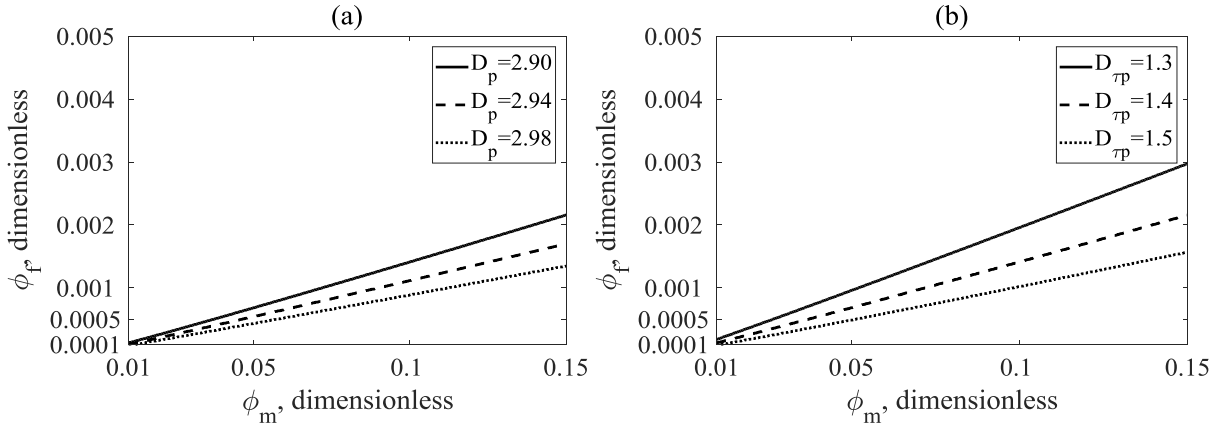

Figure 3-3 (a) Gas transport regime under different fractal dimensions of pores size, $D_{\tau p} = 1.4$; (b) gas transport regime under different fractal dimensions of tortuosity, $D_p = 2.9$. $L = 3\ cm$, $A_t = 5\ cm^2$, $P = 25\ MPa$, $T = 350\ K$, $D_f = 2.9$, $D_{\tau f} = 1.1$, $\phi_m = 0.1$, $\sigma_{min} = 1\ um$, $d_{pmin} = 1\ nm$, $\varepsilon = 1.2$, $\beta = 30°$.

3.4.2 Effect of Shale Matrix on Gas Transport Conductance

To study the gas transport conductance in shale matrix, the pore size distributions under different fractal dimensions of pore size (D_p) and minimum pore sizes (d_{pmin}) are compared as shown in Figure 3-4. Figure 3-4(a) indicates increasing D_p results in a lower frequency of occurrence of larger pores. For instance, the cumulative probability of pore size less than 5 nm is 98.2 % under $D_p = 2.5$, 98.7 % under $D_p = 2.7$ and 99.1 % under $D_p = 2.9$. Figure 3-4(b) shows increasing d_{pmin} leads to a higher frequency of occurrence of larger pores. Specially, the cumulative probability of pore size less than 5 nm is 99.1 % under $d_{pmin} = 1\ nm$, 97.0 % under $d_{pmin} = 1.5\ nm$ and 93.0 % under $d_{pmin} = 2\ nm$. Figure 3-5 (a) indicates with the increase of D_p, the total gas transport conductance decreases. Specially, if the D_p increases from 2.9 to 3, the total gas transport conductance decreases by $8 \times 10^{-16}\ (mol \cdot m)/(Pa \cdot s)$ This is because increasing D_p yields to a higher frequency of larger pores, which leaves more space for gas transport. Figure 3-5 (b) indicates increasing $D_{\tau p}$ leads to a lower total gas transport conductance. The total gas transport conductance reduces near 20% if the $D_{\tau p}$ increases from 1 to 1.5. This is because a larger $D_{\tau p}$ yields to a longer flowing path, which decreases the total gas transport conductance. Figure 3-5(c) shows with the increase of d_{pmin}, the total gas transport conductance increases. The difference between the total gas transport conductance at $d_{pmin} = 1\ nm$ and that at $d_{pmin} = 100\ nm$ is $1 \times 10^{-12}\ (mol \cdot m)/(Pa \cdot s)$. This is because increasing d_{pmin} yields to a higher frequency of occurrence of larger pores.

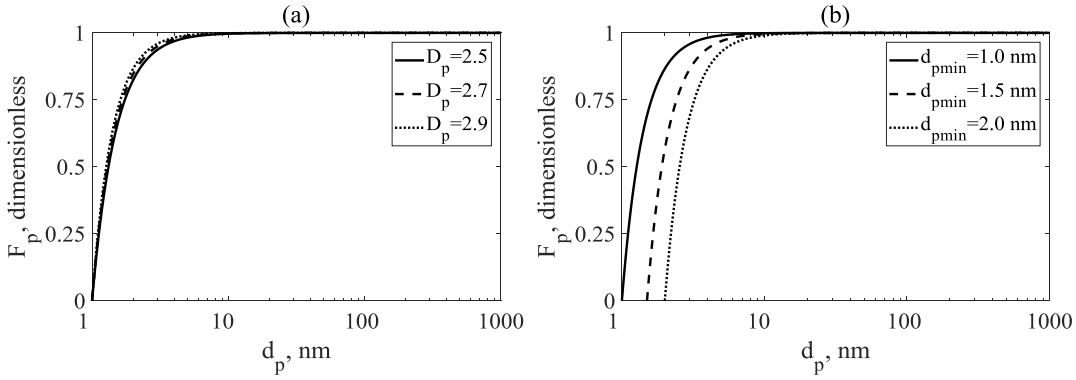

Figure 3-4 (a) Pore size distributions under different fractal dimensions of pore size, $d_{pmin} = 1\ nm$; (b) pore size distributions under minimum pore sizes, $D_p = 2.9$.

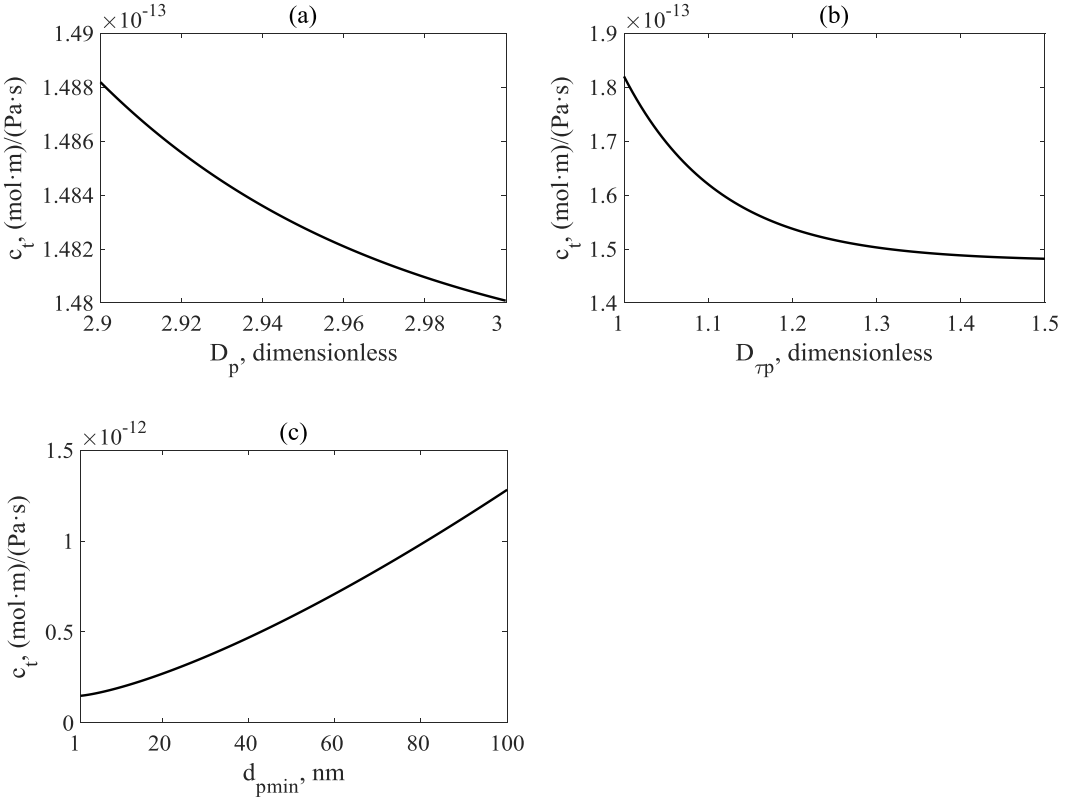

Figure 3-5 (a) Relationship between fractal dimension of pore size and total gas transport conductance, $d_{pmin} = 1\ nm$, $D_{\tau p} = 1.4$; (b) relationship between fractal dimension of tortuosity and total gas transport conductance, $D_p = 2.9$, $d_{pmin} = 1\ nm$; (c) relationship between minimum

pore size and total gas transport conductance, $D_p = 2.9$, $D_{\tau p} = 1.4$. $L = 3\ cm$, $A_t = 5\ cm^2$, $P = 25\ MPa$, $T = 350\ K$, $D_f = 2.9$, $D_{\tau f} = 1.1$, $\phi_m = 0.1$, $\sigma_{min} = 1\ um$, , $\varepsilon = 1.2$, $\beta = 30°$.

3.4.3 Effect of Shale Matrix on Gas Transport Efficiency

Effects of shale matrix on gas transport efficiency of dual-porosity shale rocks are thirdly studied as shown in Figure 3-6. Figure 3-6(a) indicates with the increase of D_p, the contour line of apparent permeability of 5000 nd moves to higher porosity region, indicating that increasing D_p decreases apparent permeability of shale rocks. This is because with a higher D_p, the frequency of occurrence of larger pores decreases, which leads to a higher adsorbed gas transport ratio. As the free gas transport better benefits in the gas transport efficiency, the apparent permeability decreases with the increase of D_p. Figure 3-6(b) shows that decreasing $D_{\tau p}$ moves the contour line of apparent permeability of 5000 nd to a lower porosity region, which means the apparent permeability increases with the decrease of $D_{\tau p}$. This is because decreasing $D_{\tau p}$ shortens the flowing path, which better benefits in the gas transport efficiency. Figure 3-6(c) indicates the contour line of apparent permeability of 5000 nd moves to lower porosity region with the increase of minimum pore size. The apparent permeability thus decreases with the decrease of minimum pore size. This is because with the increase of minimum pore size yields to a higher frequency of occurrence of larger pores, which increases the free gas transport ratio.

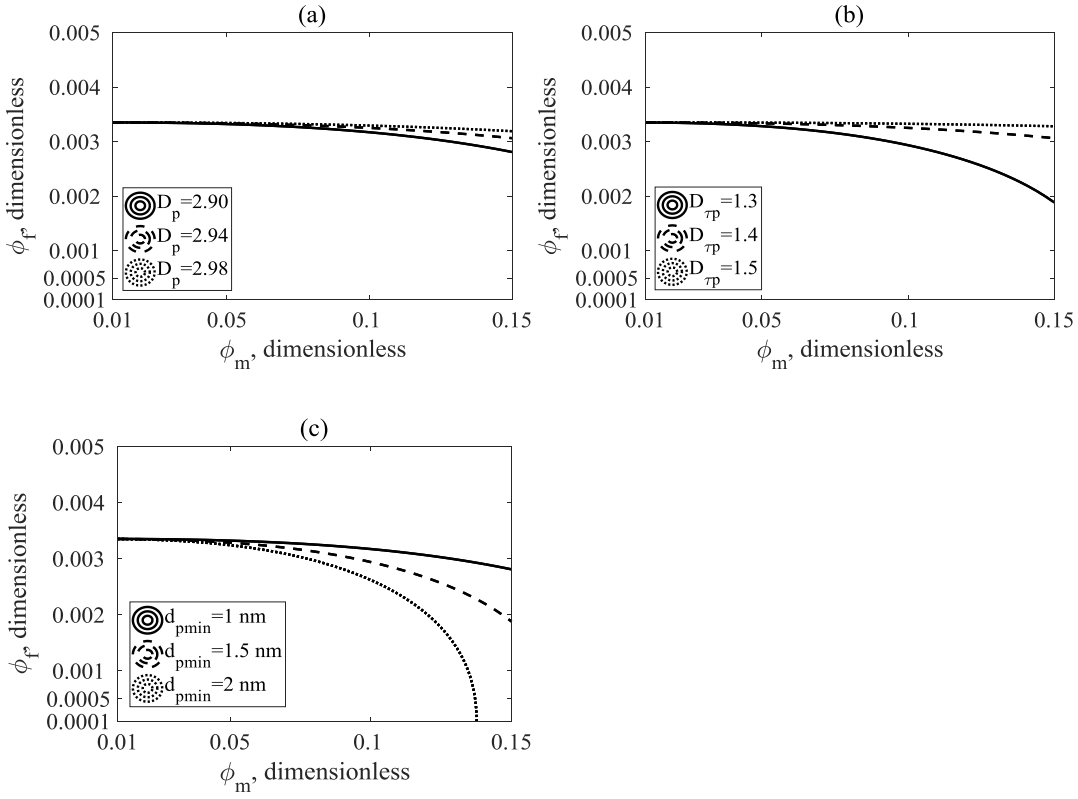

Figure 3-6 (a) Contour line of apparent permeability of 5000 nd under different fractal dimensions of pore size, $D_{\tau p} = 1.4$, $d_{pmin} = 1\,nm$; (b) Contour line of apparent permeability of 5000 nd under different fractal dimensions of tortuosity, $D_p = 2.9$, $d_{pmin} = 1\,nm$; (c) Contour line of apparent permeability of 5000 nd under different minimum pore sizes, $D_{\tau p} = 1.4$, $D_p = 2.9$. $L = 3\,cm$, $A_t = 5\,cm^2$, $P = 25\,MPa$, $T = 350\,K$, $D_f = 2.9$, $D_{\tau f} = 1.1$, $\phi_m = 0.1$, $\sigma_{min} = 1\,um$, , $\varepsilon = 1.2$, $\beta = 30°$.

3.5 Conclusions

In this study, we proposed an analytical model to explore the effect of nano-scale shale matrix on gas transport on gas transport in dual-porosity shale rocks. This model is well validated with experimental data. The following conclusions can be drawn based on this study:

(1) Increasing $D_{\tau p}$ and D_p shrinks matrix-dominated region. The more tortuous and complex the pores are presented by larger $D_{\tau p}$ and D_p, the weaker the dominancy of the pores is due to a longer flowing path and a lower frequency of occurrence of larger pores.

(2) Transport conductance owns negative relationships with $D_{\tau p}$ and D_p, and positive relationship with d_{pmin}. This is because higher D_p and lower d_{pmin} decrease the frequency of occurrence of larger pores, and a higher $D_{\tau p}$ leads to a longer flowing path.

(3) With the increase of $D_{\tau p}$ and D_p, and the decrease of d_{pmin}, the apparent peremability decreases.

Chapter Four: Nano-scale Pore Size Distribution Effects on Shale Gas Production

4.1 Introduction

As discussed in Chapter Three, gas transport efficiency varies with nano-scale pore size distributions (Miao et al., 2015; Li et al., 2016; Xu et al., 2018). However, nano-scale pore size distributions effects on shale gas production were not clearly indicated by previous studies. Studying this topic will have a number of positive impacts in evaluating shale gas production performance and contributing to the research on the development of shale gas resources.

Owing to a nano-scale pore size and a complex pore structure, interpreting gas transport mechanisms in nanopores of shale rocks had been difficult. In 2007, Javadpour et al. adopted the ideal gas kinetic theory to study the transport behavior of shale gas in single nanopores (Javadpour et al., 2007). After that, Javadpour et al. (2009), Civan (2010), Dariabi et al (2012), Rahmanian et al. (2013), Sheng et al. (2015), Wu et al. (2016), Xu et al. (2017) and Zhang et al. (2018) made a lot of improvements on gas transport models in single nanopores: (1) surface diffusion, Knudsen diffusion and viscous flow were regarded as main transport mechanisms in nanpores; (2) a real gas effect and a geomechanical effect were considered; (3) various pore structures were taken into model construction.

However, owing to a wide range of pore size distributions reported by experimental tests and theoretical studies, a gas transport model in single nanopores is limited to reveal the transport mechanisms in shale matrix. According to the study from Chalmers et al. (2012) based on the experimental tests of several samples (Marcellus, Barnett, Woodford, and Haynesville gas shales in the United States and the Doig Formation in Canada), a pore size in shale matrix can range from 1 nm to 100 um. Utpalendu and Prasad (2013), Ye et al. (2015), Zhang et al. (2015), Chalmers and

Bustin (2017) and Wu et al. (2017) also reported a wide range of pore size distributions in shale rocks. To deal with the description of a pore size distribution, a fractal theory was selected and applied. The fractal theory has been proved to be effective in experimental analyses for the samples from Baltic Basin in United Kingdom, Second White Specks and Belle Fourche formations in Canada, and Songliao Basin in China. In 2015, Miao et al. (2015) revealed more mechanisms of seepage characteristics with applying a fractal geometry theory to viscous flow analyses in shale rocks. Li et al. (2016) well validated a fractal-theory based viscous flow model with numerical simulation. Xu et al. (2018) bridged fractal shale matrix, a real gas equation of state, a tapered pore structure and gas transport mechanisms in a comprehensive model. They indicated that the occurrence of nano-pores varies with different pore size distributions, which results in different free gas transport ratios. Thus the impact of a nano-scale pore size distribution is in need to be explored for better understanding the shale gas reservoir production performance.

Previously, many models have been proposed to study the gas production performance in shale gas reservoirs. Yu and Sepehrnoori (2014) proposed an efficient reservoir-simulation approach by integrating the commercial simulator CMG GEM, an economic model, design of experiments, and a response-surface method to perform the production optimization. Jahandideh and Jafarpour (2016) developed a single porosity model to study the effect of heterogeneity on a hydraulic fracturing process. Yu et al. (2016) performed a reservoir simulation study with considering gas transport mechanisms of viscous flow and Knudsen diffusion. In his study, the effects of geometry of hydraulic fractures and gas adsorption on production performance were discussed. Yang et al. (2016) further considered the surface diffusion into reservoir simulation. They found that gas flow mechanisms in nanopores (viscous flow, Knudsen diffusion and surface diffusion) can extend the

transient production time, and the Knudsen diffusion and slippage effect play a dominant role in the later production time. Zhao et al. (2017) applied an apparent permeability formula of single nanopores into reservoir simulation. Their study indicated that the consideration of a real gas effect lifts up the cumulative gas production. Zhan et al. (2017) took the geomechanical effect into modelling during shale gas reservoir simulation with considering nano-scale transport mechanisms, and claimed that apparent permeability is decreased due to the compaction of pores.

However, there are still two main limitations for previous approaches: (1) a pore size distribution was not considered; (2) previous approaches directly connected single nanopores (level 1) and a shale gas reservoir (level 3) as shown in Figure 4-1, which results in an unrealistic estimation of gas transport efficiency with ignoring gas transport mechanisms in a bundle of pores (level 2). A thorough analysis of effects of pore size distributions on shale gas production is thus needed. In this study, an improved approach is proposed to bridge a pore size distribution, multiple transport mechanisms, a geomechanical effect and reservoir simulation. The proposed model is well validated with the available field data, and effects of a nano-scale pore size distribution on gas production are further studied.

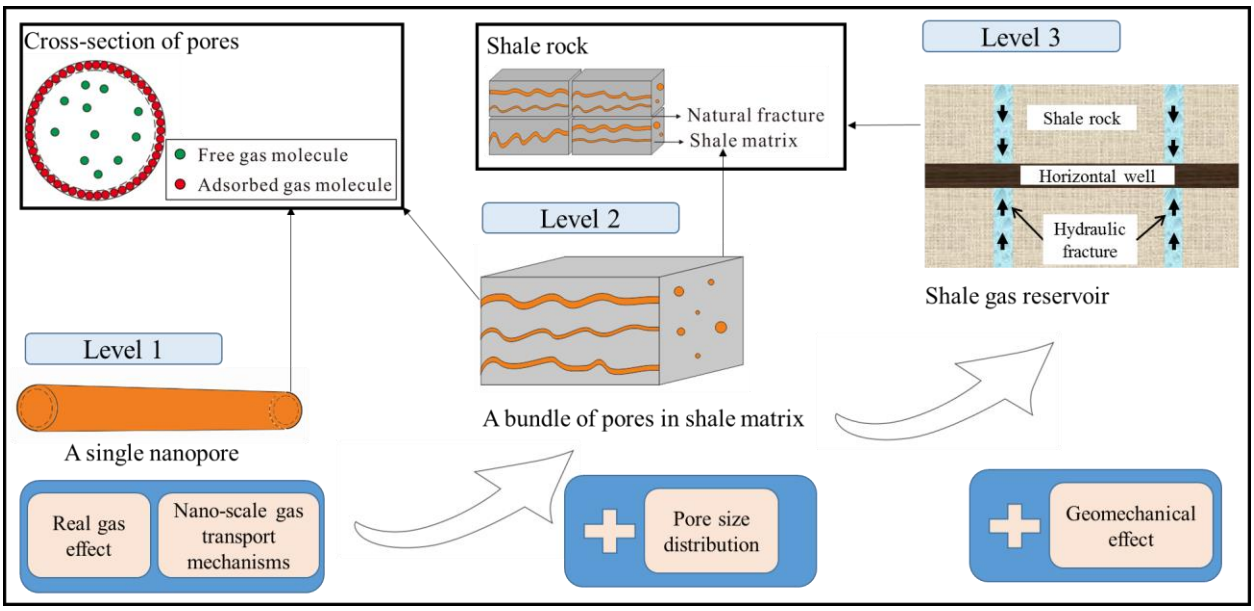

Figure 4-1 Approach of multi-scale shale gas simulation in this study.

4.2 Research Methodology

In this study, we establish an improved approach to integrate a pore size distribution, a real gas effect, nano-scale gas transport mechanisms, a geomechanical effect and computational simulation of shale gas production as shown in Figure 4-1. Multi-scale (level 1 of single nanopores, level 2 of a bundle of pores and level 3 of shale gas reservoir) gas transport models are bridged in this proposed approach, which is able to serve the analysis and optimization of shale gas reservoir production.

4.2.1 Nano-scale Pore Size Distribution

The fractal theory on a pore size distribution reflects the complexity and discreteness of pore structures (Clarkson et al., 2012; Lee et al., 2014; Bahadur et al., 2014; Wang et al., 2015). A higher fractal dimension represents a more complex pore structure. The fractal description of a

pore network has been a widely used and efficient approach to study the complexity and heterogeneity of shale gas reservoirs.

For a fractal structure, the total number of pores is as follows:

$$N_p = (\frac{d_{pmax}}{d_p})^{D_p} \tag{4-1}$$

where N_p is the total number of pores with their equivalent pore diameters larger than d_p, dimensionless; d_p is the equivalent diameter of pores in shale matrix, m, (see Appendix B); d_{pmax} is the maximum equivalent diameter of pores, m; D_p is the fractal dimension of pore sizes, dimensionless.

Based on Equation (4-1), the cumulative distribution function of equivalent pore sizes is thus as follows:

$$F_p = \begin{cases} 1 - \left(\frac{d_{pmin}}{d_p}\right)^{D_p}, & d_p \geq d_{pmin} \\ 0, & d_p < d_{pmin} \end{cases} \tag{4-2}$$

where F_p is the cumulative probability of pores with their equivalent pore diameters less than d_p; d_{pmin} is the minimum equivalent diameter of pores, m.

The total cross-sectional area of pores (A_p) is calculated based on the integration of the cross-sectional area of each pore as follows:

$$A_p = -\int_{d_{pmin}}^{d_{pmax}} \frac{\pi {d_p}^2}{4} dN_p \tag{4-3}$$

where A_p is the total cross-sectional area of pores, m^2.

By coupling equations (4-1) and (4-3), the total cross-sectional area of pores in shale rock is as follows:

$$A_p = \frac{D_p(1-\eta^{2-D_p})}{2-D_p}\frac{\pi {d_{pmax}}^2}{4} \quad (4\text{-}4)$$

The cross-sectional area of pores occupied by free gas in shale rock is as follows:

$$A_{pb} = -\int_{d_{pmin}}^{d_{pmax}} \frac{\pi(d_p-2\theta d_m)^2}{4} dN_p \quad (4\text{-}5)$$

where A_{pb} is the cross-sectional area of pores occupied by free gas, m^2.

By coupling equations (4-1) and (4-5), the cross-sectional area occupied by free gas in shale rock is as follows:

$$A_{pb} = \frac{\pi D_p}{4}\left[\frac{{d_{pmax}}^2\left(1-\eta^{2-D_p}\right)}{2-D_p} - \frac{4\theta d_m d_{pmax}\left(1-\eta^{1-D_p}\right)}{1-D_p} - \frac{4\theta^2 {d_m}^2(1-\eta^{-D_p})}{D_p}\right] \quad (4\text{-}6)$$

4.2.2 Real Gas Effect

Shale gas is mainly stored in tiny pores at supercritical temperature over a wider range of pressures in shale rocks, and the ideal gas law is no more applicable to simulation of shale gas reservoir production. The real gas effect determines the physical properties of gas to affect the free gas transport, and changes the gas coverage to affect the absorbed gas transport. In this simulation, the Soave-Redlich-Kwong (SRK) equation of state (EOS) is selected as this is the most accurate equation of state to model a shale gas process. The Peng-Robinson (PR) EOS is also a very common EOS for a hydrocarbon system, but the SRK EOS is typically applied for light hydrocarbons and a shale gas process (Marschang et al., 2014). The solution of a molar volume (V_m) is as follows:

$$V_m = -\frac{1}{3P}\left(B + \frac{3P\left(\chi^2 P+\chi RT-\alpha\kappa\right)+R^2T^2}{B} - RT\right) \quad (4\text{-}7a)$$

$$B = \sqrt[3]{\frac{g+\sqrt{g^2-4[3P(\chi^2 P+\chi RT-\alpha\kappa)+R^2T^2]^3}}{2}} \quad (4\text{-}7b)$$

$$g = -2R^3T^3 - 27\alpha\kappa\chi P^2 - 9RPT(\chi^2 P + \chi RT - \alpha\kappa) \quad (4\text{-}7c)$$

$$\alpha = [1 + (0.48508 + 1.55171\omega - 0.15613\omega^2)\left(1 - \sqrt{T_r}\right)]^2 \quad (4\text{-}7d)$$

$$\kappa = 0.42748\frac{R^2 T_c^2}{P_c} \quad (4\text{-}7e)$$

$$\chi = 0.08664\frac{RT_c}{P_c} \quad (4\text{-}7f)$$

where χ is a repulsion parameter in the SRK EOS, $(\text{Pa} \cdot \text{m}^3)/\text{mol}$; κ is an attraction parameter in the SRK EOS, m^3/mol; α is a function of gas properties and temperature in the SRK EOS, dimensionless; ω is the acentric factor, dimensionless; T_r is the reduced temperature, dimensionless, $= \frac{T}{T_c}$; V_m is the molar volume, m^3/mol; P_c is the critical pressure, Pa; T_c is the critical temperature, K.

The density of the shale gas (ρ) based on the SRK-EOS is calculated as follows:

$$\rho = \frac{M}{V_m} \quad (4\text{-}8)$$

where M is the molecular weight, kg/mol.

The viscosity (μ) is obtained as follows (Jarrahian and Heidaryan, 2014):

$$\mu = \mu_0[1 + \frac{o_1}{{T_r}^5}\left(\frac{{P_r}^4}{{T_r}^{20} + {P_r}^4}\right) + o_2\left(\frac{P_r}{T_r}\right)^2 + o_3(\frac{P_r}{T_r})] \quad (4\text{-}9)$$

where μ_0 is the gas viscosity at P = 1.01325×105 Pa and T = 423 K, $= 2.31 \times 10^{-5}$ Pa · s; P_r is the reduced pressure, dimensionless, $= \frac{P}{P_c}$; o_1, o_2 and o_3 are the fitting coefficients, $o_1 = 7.9$, $o_2 = 9 \times 10^{-6}$, $o_3 = 0.28$.

The compressibility factor (Z) based on the SRK-EOS is as follows:

$$Z = \frac{P}{nkT} \quad (4\text{-}10)$$

where k is the Boltzmann constant, $= 1.38 \times 10^{-23}\, J/K$.

The gas coverage (θ) is calculated as follows (Civan et al., 2014):

$$\theta = \frac{P/Z}{P/Z+P_L} \tag{4-11}$$

where P_L is the Langmuir pressure, Pa.

The surface diffusion coefficient ($\mathfrak{D}_s$) is calculated by the following equation (Wu et al., 2015):

$$\mathfrak{D}_s = 8.29 \times 10^{-7} T^{0.5} \exp\left(-\frac{\Delta H^{0.8}}{RT}\right) \frac{2(1-\theta)+\Psi\theta(2-\theta)+[H(1-\Psi)](1-\Psi)\Psi\theta^2}{2\left(1-\theta+\frac{\Psi}{2}\right)^2} \tag{4-12}$$

where ΔH is the isosteric adsorption heat at $\theta = 0$, J/mol; $H(\bullet)$ is the Heaviside step function; Ψ is the ratio between the blockage rate constant and the forward migration rate constant, dimensionless; $\mathfrak{D}_s$ is the surface diffusion coefficient, m^2/s.

4.2.3 Gas Transport Mechanisms in Shale Matrix

Shale gas is self-storage and self-generating with free gas, adsorbed gas and dissolved gas coexisting in shale matrix. Most of adsorbed gas is adsorbed on the surface of organic pores, with the contribution of 20%-80% to the total gas in-place (Wu et al., 2016). Three kinds of transport mechanisms (viscous flow, Knudsen diffusion and surface diffusion) are considered in this study as shown in Figure 4-2. Due to the nano-scale effect in pores, free gas can be transported by viscous flow under a pressure gradient and by Knudsen diffusion under a concentration gradient. The Knudsen diffusion is dominated by molecule-wall collision, which is more significant at low pressures and tiny pores. The viscous flow is dominated by intermolecular collision, which is more significant at high pressures and large pores. Adsorbed gas achieves mass transport by surface diffusion, in which adsorbed gas molecules move from one site to another on a pore surface.

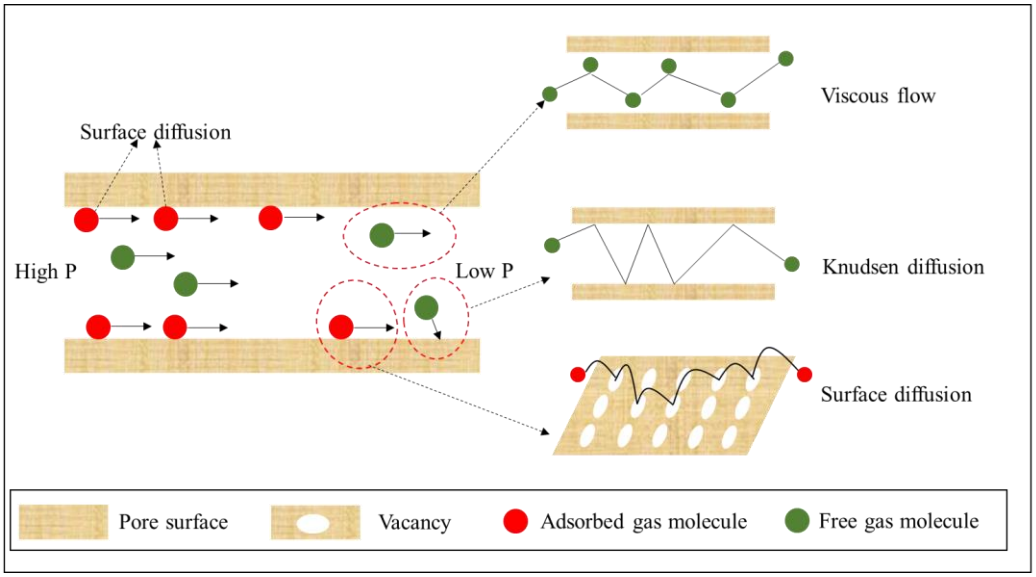

Figure 4-2 Schematic diagram of nano-scale gas transport mechanisms.

The porosity occupied by the free gas (ϕ_{mb}) and that occupied by the adsorbed gas (ϕ_{ma}) in shale matrix are calculated as follows:

$$\phi_{mb} = \frac{A_{pb}}{A_t}\phi_m \tag{4-13a}$$

$$\phi_{ma} = \phi_m - \phi_{mb} \tag{4-13b}$$

The molar rates for the viscous flow flux, Knudsen diffusion flux and surface diffusion flux in a single nanopore are as follows:

$$q_v = \frac{3\xi^3\left(\frac{2\xi^2}{\varepsilon+1}\right)^{-\frac{4}{3}}}{\xi^2+\xi+1}\frac{\pi\rho\phi_b {d_p}^4}{128\mu M}\frac{\Delta P}{L_t} \tag{4-14a}$$

$$q_k = \frac{\pi\phi_b\bar{v}{d_p}^3}{12ZRT}\frac{\Delta P}{L_t} \tag{4-14b}$$

$$q_s = \xi\left(\frac{2\xi^2}{\xi+1}\right)^{-\frac{2}{3}}\frac{\theta\phi_a\mathfrak{D}_s{d_p}^2}{N_A{d_m}^3 P}\frac{\Delta P}{L_t} \tag{4-14c}$$

where ξ is the taper ratio, dimensionless; M is the molecular weight, kg/mol; d_m is the molecular diameter, m; θ is the gas coverage, dimensionless; L_t is the tortuous length of pores, $= L^{D_\tau} {d_p}^{1-D_\tau}$, m.

Considering $Q = -\int_{d_{pmin}}^{d_{pmax}} q_v \, dN_p$, we can obtain the molar rates in a bundle of pores as follows:

$$Q_v = \frac{D_p(1-\eta^{3-D_p+D_\tau})}{3-D_p+D_\tau} \frac{3\xi^3\left(\frac{2\xi^2}{\varepsilon+1}\right)^{-\frac{4}{3}}}{\xi^2+\xi+1} \frac{\pi\phi_b\rho {d_{pmax}}^{3+D_\tau}}{128\mu M L^{D_\tau-1}} \frac{\Delta P}{L} \tag{4-15a}$$

$$Q_k = \frac{D_p(1-\eta^{2-D_p+D_\tau})}{2-D_p+D_\tau} \frac{\pi\phi_b\bar{v} {d_{pmax}}^{2+D_\tau}}{12ZRTL^{D_\tau-1}} \frac{\Delta P}{L} \tag{4-15b}$$

$$Q_s = \frac{D_p(1-\eta^{1-D_p+D_\tau})}{1-D_p+D_\tau} \xi \left(\frac{2\xi^2}{\xi+1}\right)^{-\frac{2}{3}} \frac{\phi_a\theta\mathfrak{D}_s {d_{pmax}}^{1+D_\tau}}{N_A {d_m}^3 P L^{D_\tau-1}} \frac{\Delta P}{L} \tag{4-15c}$$

where Q_v is the total viscous flow molar rate, mol/s; Q_k is the total Knudsen diffusion molar rate, mol/s; Q_s is the total surface diffusion molar rate, mol/s.

We apply the approach of linear superposition of viscous flow, Knudsen diffusion and surface diffusion for gas transport behavior, which has been well validated with simulation and experimental data in previous studies:

$$Q_t = Q_v + Q_k + Q_s \tag{4-16}$$

where Q_t is the total gas transport molar rate, mol/s.

The Darcy flow rate (Q_d) is obtained as follows:

$$Q_d = \frac{K_A \rho A_t}{\mu M} \frac{\Delta P}{L} \tag{4-17}$$

where Q_d is the Darcy flow molar rate, mol/s; K_A is the total apparent permeability, m^2.

The apparent permeability K_A is calculated as follows:

$$K_A = \frac{\mu M L Q_t}{\rho A_t \Delta P} \tag{4-18}$$

A higher apparent permeability yields to better gas transport efficiency.

4.2.4 Geomechanical Effect

Owing to a pressure decline in the development of shale gas reservoirs, the shale rock is affected by a geomechanical effect including changes in porosity and permeability of shale matrix/natural fractures and the conductivity of hydraulic fractures as shown in Figure 4-3. The permeability and porosity of natural fractures are mainly affected by rock compaction. Rock compaction and releasing of adsorbed gas molecules together influence the permeability and porosity of shale matrix. The conductivity of hydraulic fractures decreases with a pressure decline due to a stress increase. With a change in petrophysical properties of shale, gas transport mechanisms in shale matrix are significantly impacted as shown in Equation (4-15). In order to better understand the gas production performance, the geomechanical effect must be taken into modelling.

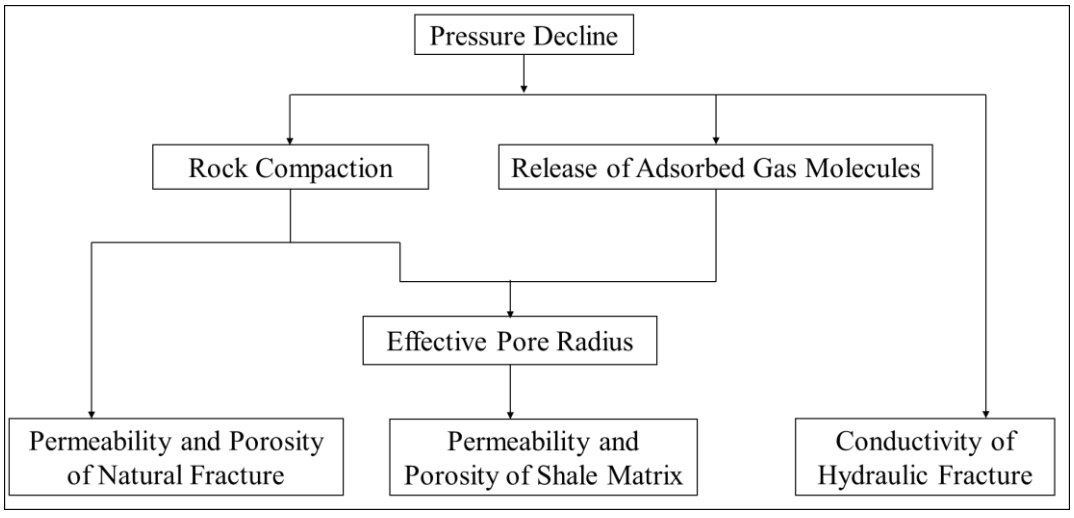

Figure 4-3 Mechanisms of how geomechanical effects influence petrophysical properties of shale.

Based on a stress sensitivity test, Dong et al. proposed the expression of porosity due to a geomechanical effect as follows (Dong et al., 2010):

$$\phi_m = \phi_{m0}\left(\frac{P_e}{P_{e0}}\right)^{-\Omega_m} \quad (4\text{-}19a)$$

$$\phi_f = \phi_{f0}\left(\frac{P_e}{P_{e0}}\right)^{-\Omega_f} \quad (4\text{-}19b)$$

where ϕ_{m0} is the shale matrix porosity at initial effective confined pressure, $= \frac{A_p}{A_t}$, dimensionless; ϕ_{f0} is the natural fracture porosity at initial effective confined pressure, dimensionless; P_e is the effective confined pressure, $= P_{ob} - P$, Pa; P_{e0} is the initial effective confined pressure, Pa; Ω_m is the shale-matrix porosity coefficient, dimensionless; Ω_f is the natural-fracture porosity coefficient, dimensionless.

Combining equation (4-19a) with $\frac{\phi_m}{\phi_{0m}} = \frac{{d_p}^2}{{d_{p0}}^2}$ (Wu et al., 2017), the equivalent pore diameter (d_p) is expressed as follows:

$$d_p = d_{p0}\left(\frac{P_e}{P_{e0}}\right)^{-\frac{\Omega}{2}} \quad (4\text{-}20)$$

where d_{p0} is the equivalent pore diameter at initial effective confined pressure, m.

The permeability of natural fractures is calculated as follows (Wang et al., 2015):

$$K_f = K_{f0}\left(\frac{P_e}{P_{e0}}\right)^{-2\Omega} \quad (4\text{-}21)$$

where K_f is the permeability of natural fractures, m^2; K_{f0} is the permeability of natural fractures at initial effective confined pressure, m^2.

The objective of hydraulic fracturing is to create high-conductivity fractures to increase a gas production rate. However, during the shale gas production, the fracture conductivity decreases

considerably as stress increases, which results in a rapid decline in the production rate. The relationship between reservoir pressure and conductivity of hydraulic fractures generally follows experimental tests. Figure 4-4 shows a decline curve of the conductivity of hydraulic fractures from Marcellus shale (Yang et al., 2015). When the gas pressure is close to 5 MPa, the fracture conductivity of Marcellus shale is only 7% initial fracture conductivity at the reservoir pressure of 32.5 MPa.

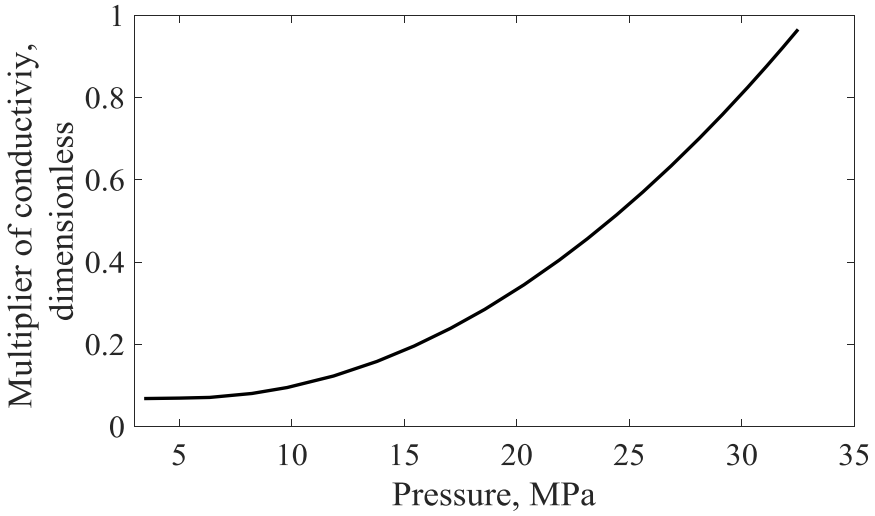

Figure 4-4 Relationship between pressure and multiplier of conductivity for Marcellus shale.

4.2.5 Simulation Procedure

Computational simulation is an efficient method to predict and evaluate well performance in shale gas reservoirs. In this thesis, a pore size distribution, a real gas effect, a geomechanical effect and nano-scale gas transport mechanisms are coupled with the reservoir simulator CMG GEM (CMG-GEM User's Guide, 2016) to study effects of a pore size distribution and nano-scale transport mechanisms on shale gas production. A flow chart showing the integration of a pore-size

distribution, nano-scale gas transport mechanism and reservoir simulation is shown in Figure 4-5. The main steps of this framework are as follows:

1. Determine the pore size distribution function, and initialize temperature and pressure;
2. Compute the physical properties of gas from EOS and geomechanical parameters;
3. Calculate the porosity and permeability of shale matrix/natural fractures based on derived equations, And obtain the conductivity of hydraulic fractures based on the curve of a relationship between conductivity and pressure;
4. Run simulations in the reservoir simulator and update pressure in each grid;
5. If the set-up time has not been reached, proceed to compute the parameters at the next time step with updated pressure. Otherwise, end the program and output all the results (i.e., pressure field, a gas production rate, and cumulative gas production) at each time step.

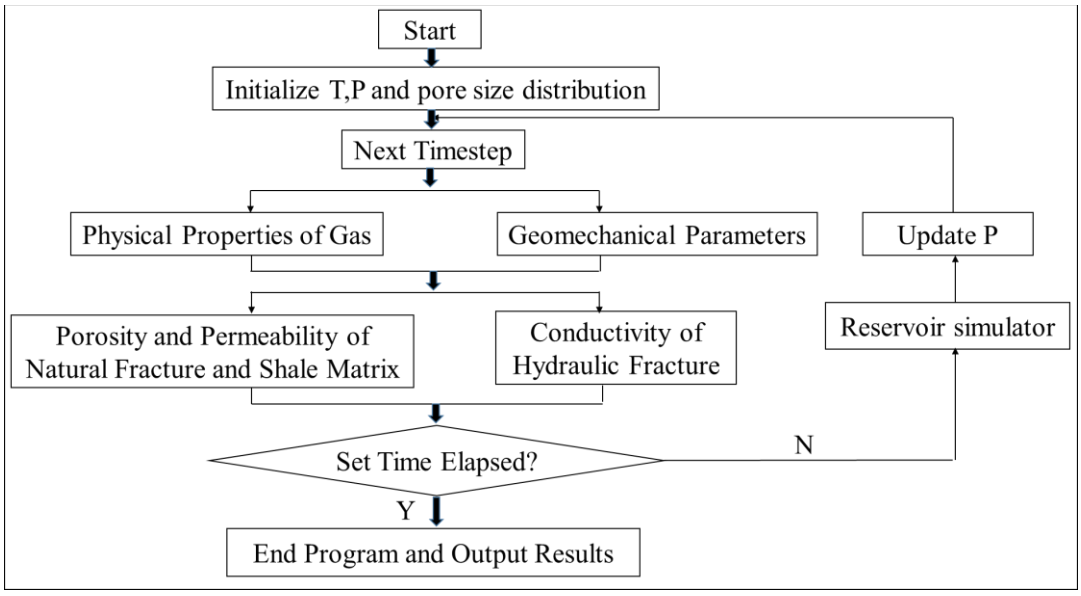

Figure 4-5 Flow chart of the framework for multi-scale shale gas simulation.

4.2.6 Industrial Application

In order to test the practicability of the proposed approach, the production data from Marcellus shale reported by Meyer et al. (2010) is selected to perform an industrial application. In this case, there are seven-stage fracture treatments on a horizontal well with the length of 640 m. Modelling parameters in this study are shown in Table 4-1 and the well constraint of this field case is well bottom-hole pressure as shown in Figure 4-6(a). The comparison with the field data is shown as Figure 4-6(c), which shows a reasonable match. The data in the early time cannot be matched very well; this is because the near-wellbore area owns a higher permeability than average hydraulic fracture permeability and it dominates the gas transport at early time, which is difficult to be simulated in a reservoir simulator.

We define the ideal model as the one without considering such mechanisms. We also define the relative error of gas production between the proposed model and ideal model as follows:

$$\text{Relative error} = \frac{\text{Gas production rate of proposed model} - \text{Gas production rate of ideal model}}{\text{Gas production rate of ideal model}} \times 100\% \quad (4\text{-}22)$$

As shown in Figure 4-6(c), the ideal model underestimates the gas production rate; this is due to the shale apparent permeability-shifting effect with a pressure decline as shown in Figure 6(b). The shale apparent permeability-shifting effect is mainly caused by the non-zero gas velocity on pore walls, and the molecule-wall collision frequency ratio gradually increases with pressure decreasing. Figure 4-6(d) shows that with time progressing, the relative error first increases and then decreases. This can be explained as follows: (1) in the early time, hydraulic fractures dominate the gas production. But with the pressure decline, the contribution of pores in shale matrix to the total flow gradually increases as the fracture conductivity significantly decreases; (2) in the later time, the apparent permeability of shale matrix decreases with the pressure decline, and the

difference of gas transport efficiency between the proposed model and ideal model becomes smaller.

Table 4-1 Modelling parameters for Marcellus Shale (Meyer et al., 2010)

Parameter	Value	Parameter	Value
Depth, m	2400	Number of fracturing stages	7
Thickness, m	50	Fractal dimension of pore size	2.95
HC Porosity	0.042	Minimum pore size, nm	1
Initial Pressure, MPa	32.58	Shale matrix porosity coefficient	0.008
Overburden Pressure, MPa	50	Natural fracture porosity coefficient	0.016
Temperature, ℃	78	Grid size, x, m	25
Reservoir size, x, m	300	Grid size, y, m	100
Reservoir size, y, m	1200	Grid size, z, m	1
Fracture half length, m	100	Number of grids in x direction	13
Fracture conductivity, $md \cdot m$	1.15	Number of grids in y direction	9
Wellbore Radius, m	0.11	Number of grids in z direction	50
Lateral length, m	640		

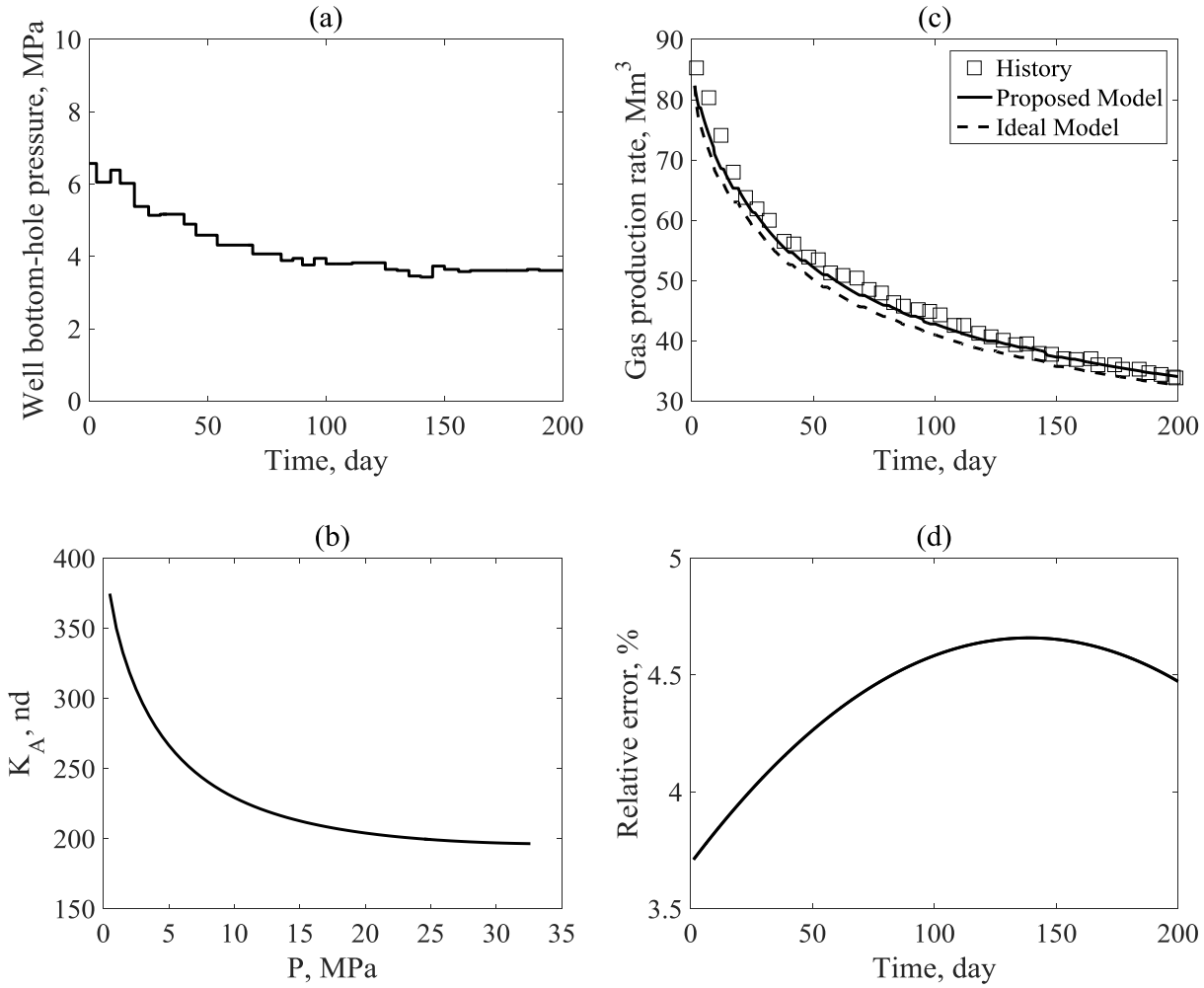

Figure 4-6 (a): relationship between well bottom-hole pressure and time from field data; (b) relationship between time and gas production rate for history, proposed model and ideal model; (c) relationship between apparent permeability and pressure in the model; (d) relationship between time and relative error.

4.3 Results and Discussion

In this section, the impact of a nano-scale pore size distribution on gas transport efficiency is first examined. Based on the conclusion, the effect of a pore size distribution on gas production is second studied. As the initial reservoir pressure is a key parameter in a real field, the role of initial

reservoir pressure in the consideration of a nano-scale pore size distribution is third discussed. Modelling parameters in this section are shown in Table 2.

Table 4-2 Modelling parameters for results and discussions

Parameter	Value	Parameter	Value
Depth, m	2400	Number of fracturing stages	7
Thickness, m	50	Fractal dimension of pore size	2.95
HC Porosity	0.042	Well-bottom hole pressure, MPa	2
Initial Pressure, MPa	22.5	Minimum pore size, nm	1
Overburden Pressure, MPa	50	Shale matrix porosity coefficient	0.008
Temperature, ℃	78	Natural fracture porosity coefficient	0.016
Reservoir size, x, m	300	Grid size, x, m	25
Reservoir size, y, m	1200	Grid size, y, m	100
Fracture half length, m	100	Grid size, z, m	1
Fracture conductivity, $md \cdot m$	1.15	Number of grids in x direction	13
Wellbore Radius, m	0.11	Number of grids in y direction	9
Lateral length, m	640	Number of grids in z direction	50

4.3.1 Impacts of nano-scale pore size distribution on shale apparent permeability

A higher fractal dimension of pore sizes indicates a more complex pore network in shale matrix; a larger variance yields a more discrete pore network. These two parameters (the fractal dimension of pore sizes and variance) are thus highlighted in a nano-scale pore size distribution.

The cumulative probability curves of pore diameters with different fractal dimensions of pore sizes (D_p) under the same variances (Var) are plotted in Figure 4-7(a). Figure 4-7(a) indicates that with an increase in D_p, the frequency of the occurrence of large pores is higher. Specially, the cumulative probability of pores with a pore diameter less than 5 nm ($F_p(d_p \leq 5\ nm)$) is 99.1 % for the $D_p = 2.93$ case, 98.1 % for the $D_p = 2.95$ case, and 96.3 % for the $D_p = 2.97$ case. When D_p increases from 2.93 to 2.97, the apparent permeability (K_A) increases two times as shown in Figure 4-7(b), indicating that a higher fractal dimension of pore sizes leads to better transport efficiency of shale matrix. This is because a higher frequency of large pores leads to a higher free gas transport ratio, which better benefits the gas transport efficiency. The cumulative probability curves with different vari ances under the same D_p are shown in Figure 4-7(c). With a higher Var, the large pores occur more frequently. For instance, the cumulative probability of pores with the pore diameter less than 5 nm ($F_p(d_p \leq 5\ nm)$) is 98.8 % for the $Var = 0.5\ nm^2$ case, 98.1 % for the $Var = 0.55\ nm^2$ case, and 97.2 % for the $Var = 0.6\ nm^2$ case. A more frequent occurrence of large pores further leads to a higher apparent permeability as shown in Figure 4-7(d), which indicates that a higher variance better benefits the gas transport efficiency.

The shale apparent permeability-shifting effect with a pressure decline is shown Figures 4-7(c) and (d). In order to better study this phenomenon, we define the increasing percentage of apparent permeability (ζ) as the relative difference between the apparent permeability at well bottom-hole pressure (BHP) ($K_{A,BHP}$) and the apparent permeability at initial pressure (K_{A,P_0}) (Figures 4-8(a) and (c)):

$$\zeta = \frac{K_{A,BHP} - K_{A,P_0}}{K_{A,P_0}} \times 100\% \tag{4-23}$$

With the objective of studying the sensitivity of a shale apparent permeability-shifting effect to a pore size distribution, we also study the absolute values of the slope of $\zeta - D_p$ ($|\frac{d\zeta}{dD_p}|$) and the slope of $\zeta - Var$ ($|\frac{d\zeta}{dVar}|$) as shown in Figures 4-8(b) and (d).

Figure 4-8(a) shows that a higher D_p leads to a lower increasing percentage of apparent permeability (ζ). Specially, if D_p increases from 2.9 to 2.999, ζ decreases more than four times. This is because the Knudsen diffusion mainly contributes to the increase of apparent permeability with a pressure decline and the ratio of Knudsen diffusion decreases with a higher frequency of occurrence of large pores as shown in Figure 4-7(a). Figure 4-8(b) indicates that the sensitivity of a shale apparent permeability-shifting effect to a fractal dimension decreases with an increase in D_p. This is because the effect of nano-scale gas transport mechanisms on gas transport efficiency decreases with a higher frequency of occurrence of large pores. The relationship between variance and increasing percentage of apparent permeability is shown in Figure 4-8(c). With a larger variance, a lower ζ exhibits. For instance, ζ is 49.8 % for the $Var = 0.5\ nm^2$ case and 34.4 for the $Var = 0.6\ nm^2$ case. This is due to a higher frequency of occurrence of large pores as shown in Figure 4-7(c). Figure 4-7(d) further shows that a higher variance reduces the sensitivity of the shale apparent permeability-shifting effect to variance.

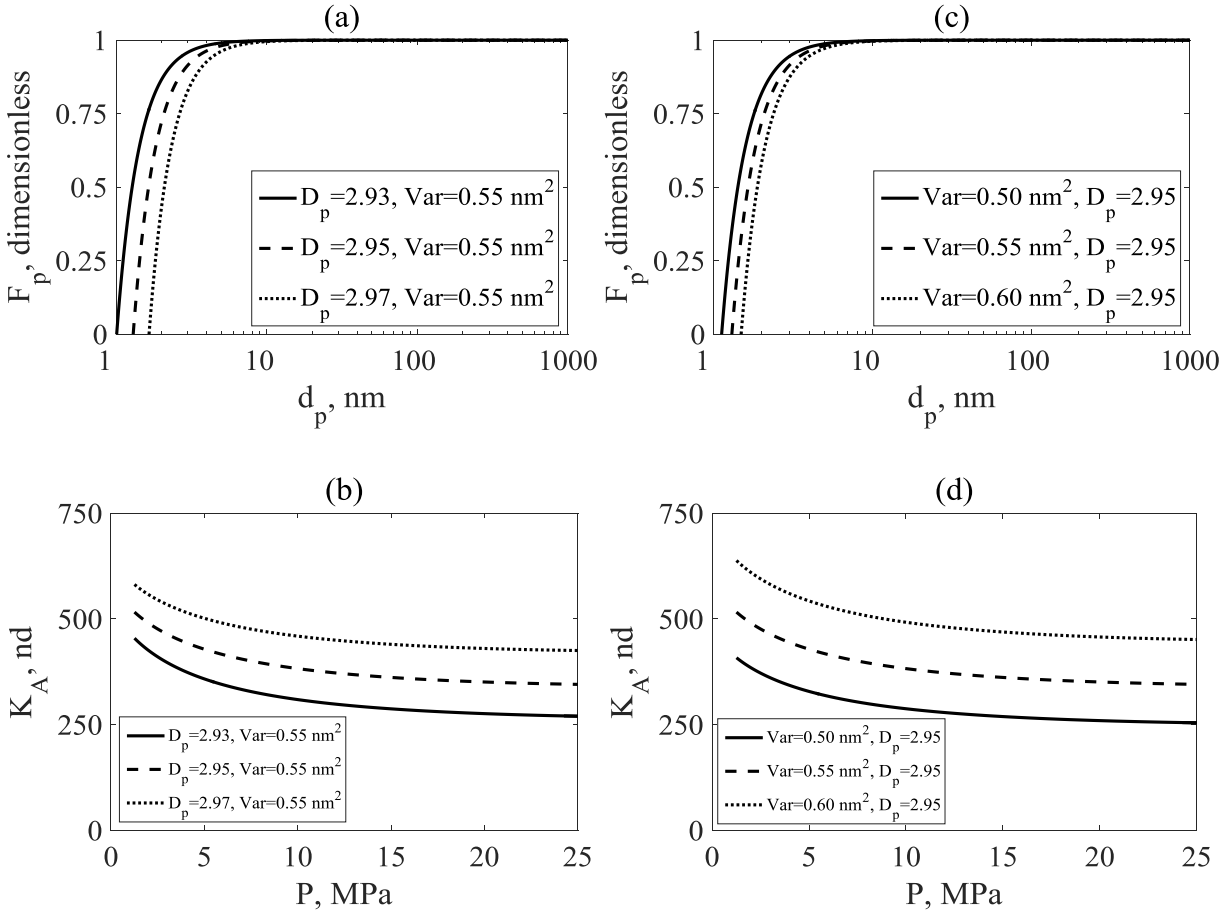

Figure 4-7 (a): relationship between cumulative probability and pore size under different $\boldsymbol{D_p}$; (b) relationship between apparent permeability and pressure under different $\boldsymbol{D_p}$;(c) relationship between cumulative probability of pores and pore size under different variances; (d) relationship between apparent permeability and pressure under different variances.

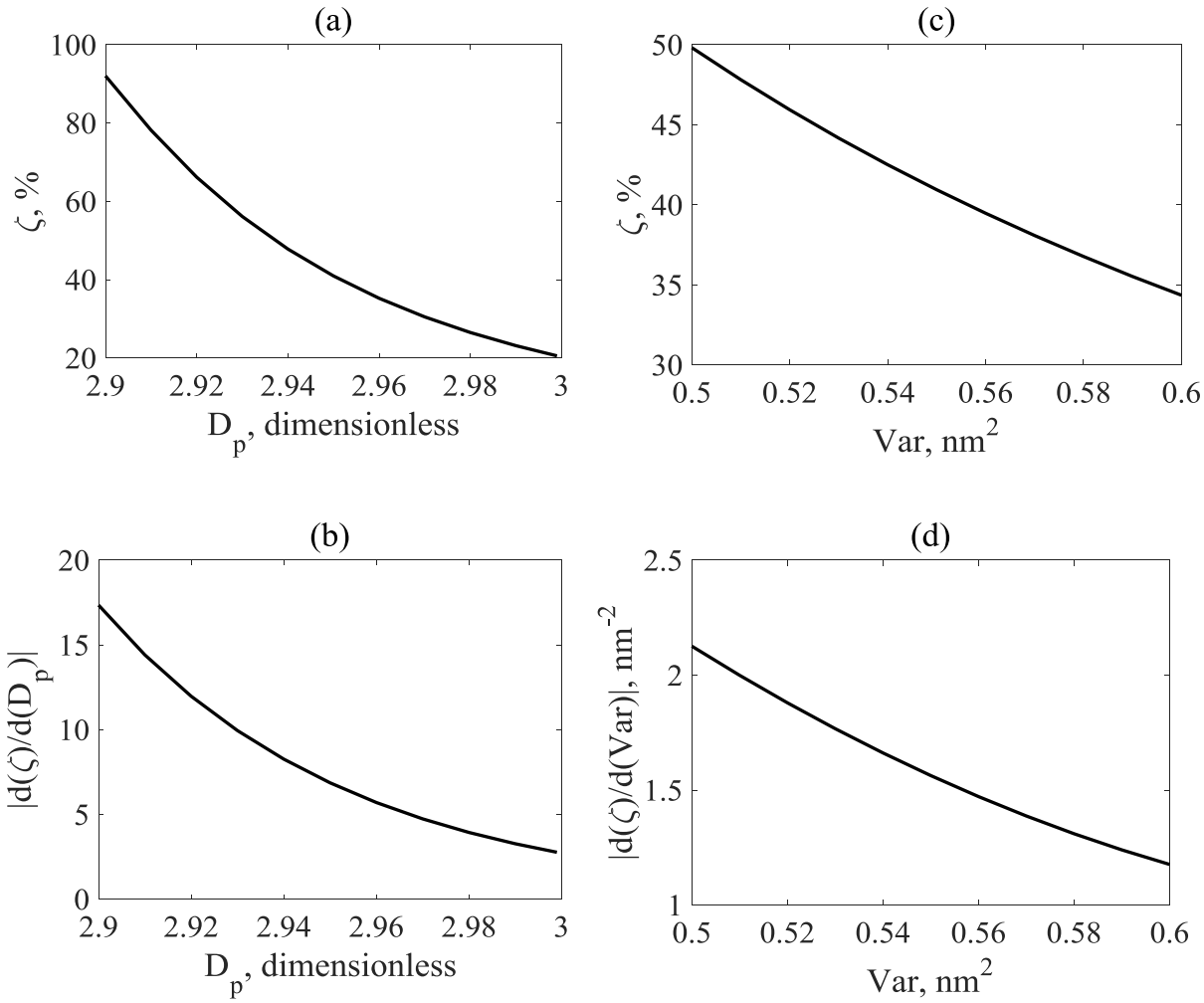

Figure 4-8 (a) relationship between increasing percentage of shale apparent permeability and fractal dimension, $Var = 0.55\ nm^2$; (b) relationship between the slope of $\zeta - D_p$ and fractal dimension, $Var = 0.55\ nm^2$; (c) relationship between increasing percentage of shale apparent permeability and variance, $D_p = 2.95$; (d) relationship between the slope of $\zeta - Var$ and variance, $D_p = 2.95$.

4.3.2 Effects of nano-scale pore size distribution on gas production

As shown in Figure 4-9(a), different shale gas cumulative productions (Q_{prod}) are obtained based on various fractal dimensions. Especially, the relative change of cumulative gas production between the lowest case ($D_p = 2.999$) and the highest case ($D_p = 2.9$) reaches 20%, which indicates that the shale gas production is significantly affected by a pore size distribution. A pore size distribution with a higher D_p yields a higher cumulative gas production; this is because a higher fractal dimension yields a higher apparent permeability as shown in Figure 4-7(b), and a larger drainage area is obtained based on a higher apparent permeability as shown in Figure 4-10. The slope (dQ_{prod}/dD_p) of the gas production rate versus D_p is applied to qualify the sensitivity of gas production to a fractal dimension as shown in Figure 4-9(b). Figure 4-9(b) shows that a higher complexity of a pore network yields a lower sensitivity of the gas production rate to a fractal dimension; this is because the shale apparent permeability-shifting effect is less obvious in a more complex pore network as shown in Figure 4-8(b). Figure 4-9(c) shows the relationship between cumulative gas production and variance; a larger variance yields a higher cumulative gas production, which is due to better gas transport efficiency as shown in Figure 4-7(d). Figure 4-9(d) indicates that the sensitivity of gas production to variance decreases with a higher variance. Specially, when variance increases from 0.5 nm^2 to 0.6 nm^2, the absolute value of the slope of $Q_{prod} - Var$ decreases by 10%. This is because a higher variance reduces the sensitivity of a shale apparent permeability-shifting effect to a nano-scale pore size distribution as shown in Figure 4-8(d).

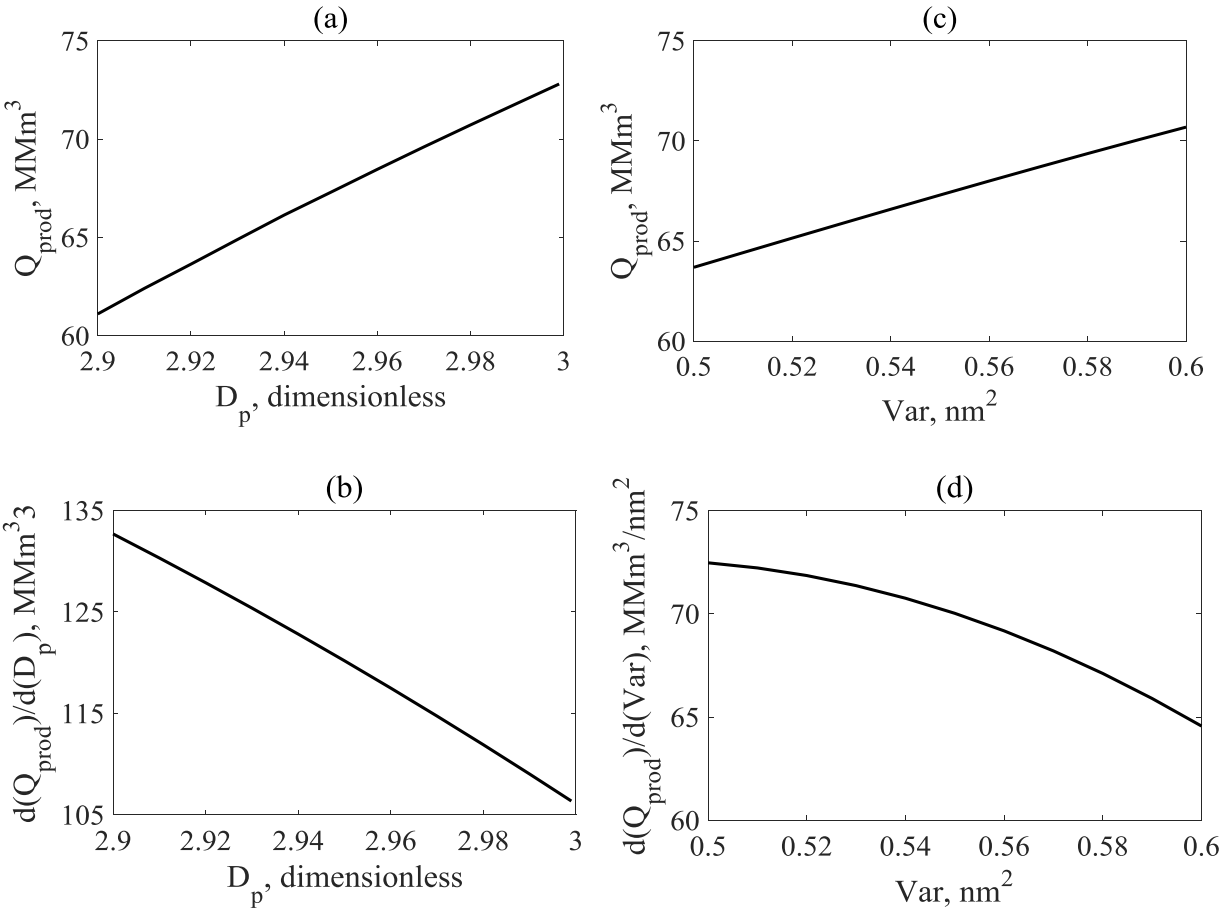

Figure 4-9 (a) relationship between cumulative gas production and fractal dimension of pore size, $Var = 0.55\ nm^2$; (b) relationship between the slope of $Q_{prod} - D_p$ and D_p, $Var = 0.55\ nm^2$; (c) relationship between cumulative gas production and variance, $D_p = 2.95$; (d) relationship between the slope of $Q_{prod} - Var$ and Var, $D_p = 2.95$.

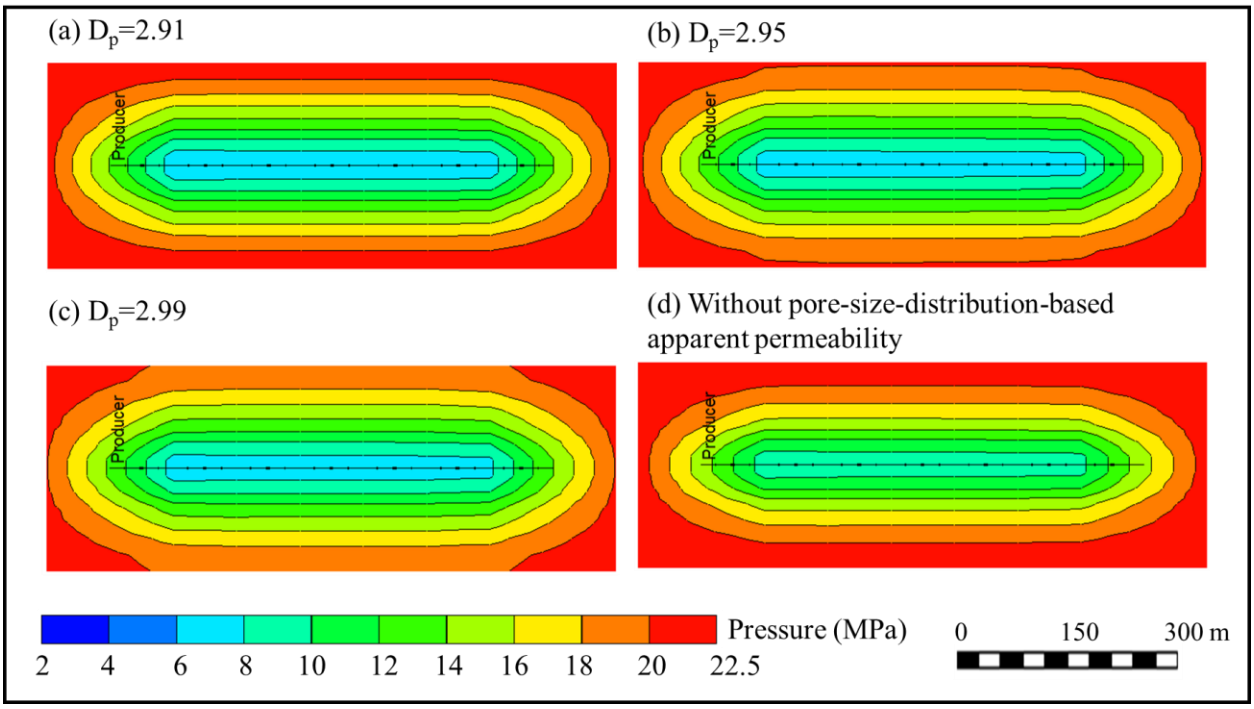

Figure 4-10 Contour map of pressure distribution after 5 years ((a): $D_p = 2.91$; (b): $D_p = 2.95$; (c) $D_p = 2.99$; (d): without pore-size-distribution-based apparent permeability).

4.3.3 Role of initial reservoir pressure in considering pore size distribution

Owing to a gradual increase in apparent permeability with a pressure decline, the sensitivity of gas flow to a pore size distribution at different initial reservoir pressures is of great importance to be examined. Figure 4-11(a) indicates that a higher initial reservoir pressure yields a higher sensitivity of a shale apparent permeability-shifting effect to a fractal dimension of pore sizes. When the fractal dimension of pore sizes is 2.9, $|\frac{d\zeta}{dD_p}|$ at the initial reservoir pressure of 20 MPa, 22.5 MPa and 25 MPa are 111.8, 132.7 and 145.1, respectively. This behavior is because the molecule-wall collision ratio is lower under a higher pressure condition, which provides a more room for apparent permeability-shifting with a pressure decline. A higher sensitivity of the

apparent permeability-shifting effect makes the gas production at higher pressure to be more sensitive to the fractal dimension of pore sizes as shown in Figure 4-11(b). Specially at $D_p = 2.95$, $|\frac{dQ_{prod}}{dD_p}|$ increases from 111.8 MMm^3 to 145.1 MMm^3 when the initial reservoir pressure increases from 20 MPa to 25 MPa. Figure 4-11(c) indicates that the shale apparent permeability-shifting effect is more sensitive to variance at a higher initial reservoir pressure. When the variance is 0.5 nm^2, $|\frac{d\zeta}{dVar}|$ equals 2.0 nm^{-2}, 2.1 nm^{-2} and 2.2 nm^{-2} at initial reservoir pressures of 20 MPa, 22.5 MPa and 25Mpa, respectively. Owing to a higher sensitivity of the apparent permeability-shifting effect to variance, the gas production is more sensitive to variance at a higher initial reservoir pressure as shown in Figure 4-11(d). Thus the influence of a nano-scale pore size distribution is magnified at a higher initial reservoir pressure condition.

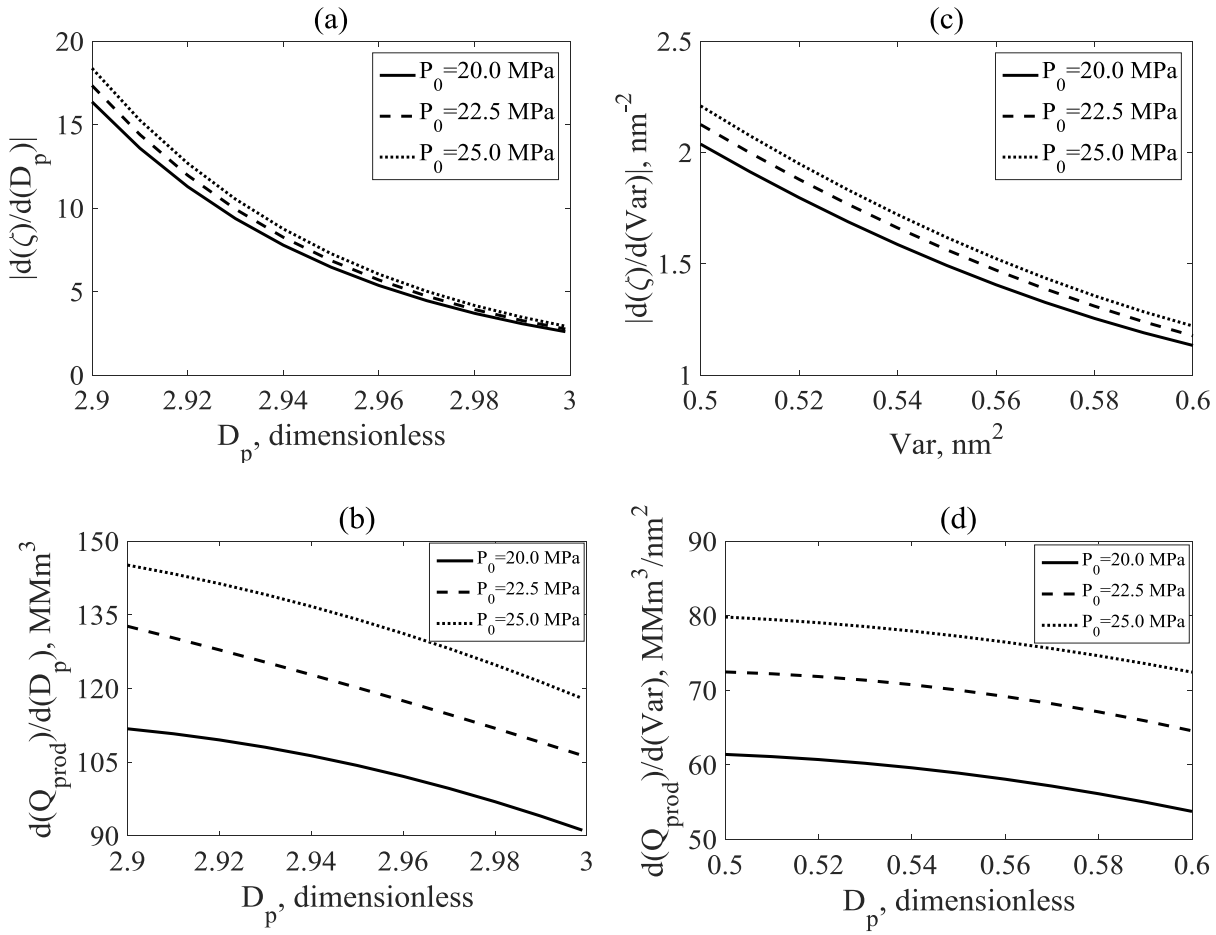

Figure 4-11 (a) relationship between the slope of $\zeta - D_p$ and fractal dimension, $Var = 0.55\ nm^2$; (b) relationship between the slope of $Q_{prod} - D_p$ and D_p at various initial reservoir pressures, $Var = 0.55\ nm^2$ (c) relationship between the slope of $\zeta - Var$ and variance, $D_p = 2.95$.; (d) relationship between the slope of $Q_{prod} - Var$ and variance at different initial reservoir pressures, $D_p = 2.95$.

4.4 Conclusions

An improved approach for multi-scale gas transport simulation in shale gas reservoirs has been proposed in this study, which bridges a nano-scale pore size distribution, a real gas effect, a

geomechanical effect, multiple real gas transport mechanisms and field-scale gas production. Based on the proposed approach, the effects of a nano-scale pore size distribution on gas production are further explored and highlighted. Validations of this model with field data have shown the reliability and practicability of the present model. The main conclusions are as follows:

(1) A larger fractal dimension of a pore size results in a higher frequency of occurrence of large pores, which further results in a higher gas transport efficiency; a larger variance yields better transport efficiency with increased frequency of occurrence of large pores.

(2) In a shale gas reservoir owning a pore size distribution with a higher fractal dimension of pore sizes and variance, the shale apparent permeability-shifting effect is less obvious, and the sensitivity of this effect to a nano-scale pore size distribution is also impaired.

(3) A pore size distribution with a higher fractal dimension of pore sizes and variance yields higher cumulative gas production and a lower sensitivity of the gas production rate to a nano-scale pore size distribution.

(4) The shale apparent permeability-shifting effect is more sensitive to a nano-scale pore size distribution under a higher initial reservoir pressure; this behavior brings a higher sensitivity of gas production to a nano-scale pore size distribution.

Chapter Five: Conclusions and Recommendations

5.1 Conclusions

This thesis is focused on multi-scale shale gas transport in shale matrix. Based on three stages of the work, we can draw conclusions as follows:

We first present a model for real gas transport in tapered non-circular nanopores of shale rocks bridging the real gas effect and molecular kinetic and transport behavior. The proposed model is also well validated with experimental and simulation data. Compared with the previous work, this model considers the structure of tapered non-circular nanopores, applies an EOS into calculations, and provides a flow regime map. Results show that the flow conductance will be misled if the real gas effects are neglected. The real gas effects influence the tapered circular nanopore the most, ahead of tapered square, elliptical and rectangular nanopores. Real gas effects are weakened and the free gas transport ratio are lowered if the taper ratio and aspect ratio increase. Moreover, the taper effect lowers the total transport capacity of nanopores, and the tapered circular nanopores own the greatest transport capacity, followed by tapered square, elliptical and rectangular nanopores.

We second proposed a gas transport model in a dual-porosity shale rock composed of a bundle of pores in shale matrix and a bundle of channels in natural fracture. The model is well validated with experimental data. Results indicate that decreasing fractal dimensions of pore size and tortuosity expands matrix-dominated region. More tortuous and complex pores weak the dominancy of the shale matrix. Transport conductance owns negative relationships with fractal dimensions of pore size and tortuosity, and positive relationship with minimum pore size. With

the derease of fractal dimensions of pore size and tortuosity, and the decrease of minimum pore size, the apparent peremability decreases.

Based on the work from the previous two stages, we third propose an improved approach to bridge a nano-scale pore size distribution, multiple gas transport mechanisms and shale gas production. This model is well validated with field tests. Results indicate that the gas production is underestimated without considering nano-scale pore size distribution-based gas transport mechanisms. A pore size distribution with a higher fractal dimension of pore sizes and variance yields a higher frequency of occurrence of large pores, which further results in better gas transport efficiency. With an increase in the fractal dimension of pore sizes and variance, the apparent permeability-shifting effect is less obvious, and the sensitivity of this effect to a nano-scale pore size distribution is also impaired. A higher fractal dimension of pore sizes and a higher variance result in higher cumulative gas production and a lower sensitivity of gas production to a nano-scale pore size distribution. The shale apparent permeability-shifting effect is more sensitive to a nano-scale pore size distribution under a higher initial reservoir pressure, which results in a higher sensitivity of gas production to a nano-scale pore size distribution.

5.2 Recommendations

Although significant improvements have been achieved in this thesis to understand the gas flow in shale matrix, some improvements can be made in the following areas. First, sub-irreducible water in pores has been reported in some shale formations (Li et al., 2017), which affects the gas transport in nano-scale. A relative gas-water relative permeability based on the derived apparent permeability of gas and water is thus in need to be explored. Second, the enhanced shale gas recovery by a CO2 gas injection technique has been studied in recent years (Du et al., 2017). How

to deal with the multi-component gas transport in nanopores is a big challenge and worth to be studied. Third, most of current pressure transient analysis studies on shale gas production did not consider a shale apparent permeability-shifting effect. Improving the existing pressure transient analysis methods is valuable to industrial applications.

.

Appendix A: Structural Parameters and Gas Properties in Tapered Non-Circular Nanopores

The volume (V) of the tapered nanopores is calculated as follows:

$$V = \begin{cases} \frac{{h_{in}}^2 w_{in}}{3(h_{in}-h_{out})} L - \frac{{h_{out}}^2 w_{out}}{3(h_{in}-h_{out})} L, Rectangular \\ \frac{\pi a_{in} {b_{in}}^2}{12(b_{in}-b_{out})} L - \frac{\pi a_{out} {b_{out}}^2}{12(b_{in}-b_{out})} L, Elliptical \end{cases} \quad \text{(A-1)}$$

By coupling Equations (2-1), (2-2) and (A-1), we can obtain the expression of V for tapered nanopores as follows:

$$V = \begin{cases} \frac{\gamma_R({\xi_R}^2+\xi_R+1){h_{in}}^2}{3{\xi_R}^2} L, Rectangular \\ \frac{\pi\gamma_E({\xi_E}^2+\xi_E+1){b_{in}}^2}{12{\xi_E}^2} L, Elliptical \end{cases} \quad \text{(A-2)}$$

As the thickness of the single adsorbed layer is θd_m (Wu et al., 2016), we can obtain the pore volume occupied free gas (V_b) as follows:

$$V_b = \begin{cases} \frac{\gamma_R({\xi_R}^2+\xi_R+1)(h_{in}-2\theta d_m)^2}{3{\xi_R}^2} L, Rectangular \\ \frac{\pi\gamma_E({\xi_E}^2+\xi_E+1)(b_{in}-2\theta d_m)^2}{12{\xi_E}^2} L, Elliptical \end{cases} \quad \text{(A-3)}$$

Thus we can obtain the average effective porosity for free gas transport ($\overline{\phi_b}$) and the average effective porosity for adsorbed gas transport ($\overline{\phi_a}$) as follows:

$$\overline{\phi_b} = \begin{cases} \frac{(h_{in}-2\theta d_m)^2}{{h_{in}}^2} \phi, Recatangular \\ \frac{(b_{in}-2\theta d_m)^2}{{b_{in}}^2} \phi, Elliptical \end{cases} \quad \text{(A-4)}$$

$$\overline{\phi_a} = \phi - \overline{\phi_b} \quad \text{(A-5)}$$

The effective porosity for free gas transport along the length of the nanopore (ϕ_b) and the effective porosity for adsorbed gas transport along the length of the nanopore (ϕ_a) are obtained as follows:

$$\phi_b = \begin{cases} \frac{(h-2\theta d_m)(w-2\theta d_m)}{hw}, \ Rectangular \\ \frac{(a-2\theta d_m)(b-2\theta d_m)}{ab}, \ Elliptical \end{cases} \tag{A-6}$$

$$\phi_b = \phi - \phi_b \tag{A-7}$$

The mean cross-sectional area ($\bar{A}$) is obtained as follows:

$$\bar{A} = \frac{V}{L} = \begin{cases} \frac{\gamma_R({\xi_R}^2+\xi_R+1)}{3{\xi_R}^2} {h_{in}}^2, Rectangular \\ \frac{\pi\gamma_E({\xi_E}^2+\xi_E+1)}{12{\xi_E}^2} {b_{in}}^2, Elliptical \end{cases} \tag{A-8}$$

The cross-sectional area along the length of the nanopore (A) is calculated as follows:

$$A = \begin{cases} hw, \ Recatangular \\ \frac{\pi ab}{4}, \ Elliptical \end{cases} \tag{A-9}$$

Particularly, the inlet cross-sectional area (A_{in}) is obtained as follows:

$$A_{in} = \begin{cases} \gamma_R {h_{in}}^2, \ Recatangular \\ \frac{\pi\gamma_E {b_{in}}^2}{4}, \ Elliptical \end{cases} \tag{A-10}$$

The cross-sectional area occupied by free gas along the nanopore (A_b) is obtained as follows:

$$A_b = \begin{cases} (h-2\theta d_m)(w-2\theta d_m), Recatangular \\ \frac{\pi(a-2\theta d_m)(b-2\theta d_m)}{4}, Elliptical \end{cases} \tag{A-11}$$

The cross-sectional area occupied by adsorbed gas along the nanopore (A_a) is obtained as follows:

$$A_a = A - A_b \tag{A-12}$$

The hydraulic diameter (d_H) is defined as follows (Panigraphi, 2016):

$$d_H = \begin{cases} \frac{2hw}{h+w}, \ Rectangular \\ \frac{2ab}{[3(a+b)-\sqrt{(3a+b)(a+3b)}]}, \ Elliptical \end{cases} \quad \text{(A-13)}$$

Appendix B: Derivation of Average Viscous Flow Conductance in Tapered Non-Circular Nanopores

Equation (B-1) is obtained by coupling Equations (2-1), (2-2) and (2-4).

$$q_v = \begin{cases} -\frac{\phi_{eb}}{\tau}\frac{\rho{\gamma_E}^3 h^4}{12\mu M}\left[1-\frac{192\gamma_E}{\pi^5}\sum_{i=1,3,5,\ldots}^{\infty}\frac{tanh(i\pi/2\gamma_E)}{i^5}\right]\nabla P, Rectangular \\ -\frac{\phi_{eb}}{\tau}\frac{\pi\rho b^4}{64\mu M}\frac{{\gamma_E}^3}{{\gamma_E}^2+1}\nabla P, Elliptical \end{cases} \quad \text{(B-1)}$$

We further couple Equations (B-1) and (2-3), and get Equation (B-2) as follows:

$$q_v = \begin{cases} -\frac{\phi_{eb}}{\tau}\frac{\rho{\gamma_E}^3 h^4}{12\mu M}\frac{h_{out}-h_{in}}{L}\left[1-\frac{192\gamma_E}{\pi^5}\sum_{i=1,3,5,\ldots}^{\infty}\frac{tanh(i\pi/2\gamma_E)}{i^5}\right]\frac{dP}{dh}, Rectangular \\ -\frac{\phi_{eb}}{\tau}\frac{\pi\rho b^4}{64\mu M}\frac{b_{out}-b_{in}}{L}\frac{{\gamma_E}^3}{{\gamma_E}^2+1}\frac{dP}{db}, Elliptical \end{cases} \quad \text{(B-2)}$$

After performing integrations, we can obtain the expression of q_v as Equation (2-5).

q_k and q_s can be obtained in the similar way.

Appendix C: Copyright Permission

Copyright Clearance Center RightsLink®

Home | Account Info | Help

Title: Real gas transport in tapered noncircular nanopores of shale rocks

Author: Jinze Xu,Keliu Wu,Sheng Yang,Jili Cao,Zhangxin Chen,Yi Pan,Bicheng Yan

Publication: AIChE Journal

Publisher: John Wiley and Sons

Date: Mar 2, 2017

Logged in as:
Jinze Xu
Account #:
3001068409
LOGOUT

Order Completed

Thank you for your order.

This Agreement between Jinze Xu ("You") and John Wiley and Sons ("John Wiley and Sons") consists of your license details and the terms and conditions provided by John Wiley and Sons and Copyright Clearance Center.

Your confirmation email will contain your order number for future reference.

printable details

License Number	4302370307291
License date	Mar 05, 2018
Licensed Content Publisher	John Wiley and Sons
Licensed Content Publication	AIChE Journal
Licensed Content Title	Real gas transport in tapered noncircular nanopores of shale rocks
Licensed Content Author	Jinze Xu,Keliu Wu,Sheng Yang,Jili Cao,Zhangxin Chen,Yi Pan,Bicheng Yan
Licensed Content Date	Mar 2, 2017
Licensed Content Pages	19
Type of use	Dissertation/Thesis
Requestor type	Author of this Wiley article
Format	Print and electronic
Portion	Full article
Will you be translating?	No
Title of your thesis / dissertation	Multi-scale Real Gas Transport in Shale Matrix
Expected completion date	Mar 2018
Expected size (number of pages)	101
Attachment	
Requestor Location	Jinze Xu 3707, Valdes Place, NW Calgary, AB T2L 2A2 Canada Attn: Jinze Xu
Publisher Tax ID	EU826007151
Total	0.00 USD

Would you like to purchase the full text of this article? If so, please continue on to the content ordering system located here: Purchase PDF

If you click on the buttons below or close this window, you will not be able to return to the content ordering system.

ORDER MORE | CLOSE WINDOW

References

Akkutlu, I. Y., Efendiev, Y., Vasilyeva, M., & Wang, Y. (2017). Multiscale model reduction for shale gas transport in a coupled discrete fracture and dual-continuum porous media. Journal of Natural Gas Science and Engineering, 48, 65-76.

Andrews, I. J. (2013). The Carboniferous Bowland Shale gas study: geology and resource estimation.

Barisik, M., & Beskok, A. (2014). Scale effects in gas nano flows. Physics of Fluids, 26(5), 052003.

Bocora, J. (2012). Global prospects for the development of unconventional gas. Procedia-Social and Behavioral Sciences, 65, 436-442.

Bolsaitis, P., & Spain, I. L. (1977). High pressure technology. Marcel Dekker,(New York), 1, 477.

Bustin, R. M., Bustin, A. M., Cui, A., Ross, D., & Pathi, V. M. (2008, January). Impact of shale properties on pore structure and storage characteristics. In SPE shale gas production conference. Society of Petroleum Engineers.

Bahadur, J., Melnichenko, Y. B., Mastalerz, M., Furmann, A., & Clarkson, C. R. (2014). Hierarchical pore morphology of cretaceous shale: a small-angle neutron scattering and ultrasmall-angle neutron scattering study. Energy & Fuels, 28(10), 6336-6344.

Bu, H., Ju, Y., Tan, J., Wang, G., & Li, X. (2015). Fractal characteristics of pores in non-marine shales from the Huainan coalfield, eastern China. Journal of Natural Gas Science and Engineering, 24, 166-177.

Chalmers, G. R., Bustin, R. M., & Power, I. M. (2012). Characterization of gas shale pore systems by porosimetry, pycnometry, surface area, and field emission scanning electron

microscopy/transmission electron microscopy image analyses: Examples from the Barnett, Woodford, Haynesville, Marcellus, and Doig units. AAPG bulletin, 96(6), 1099-1119.

Chalmers, G. R., & Bustin, R. M. (2017). A multidisciplinary approach in determining the maceral (kerogen type) and mineralogical composition of Upper Cretaceous Eagle Ford Formation: Impact on pore development and pore size distribution. International Journal of Coal Geology, 171, 93-110.

Chalmers, G. R., Ross, D. J., & Bustin, R. M. (2012). Geological controls on matrix permeability of Devonian Gas Shales in the Horn River and Liard basins, northeastern British Columbia, Canada. International Journal of Coal Geology, 103, 120-131.

Clarkson, C. R., Solano, N., Bustin, R. M., Bustin, A. M. M., Chalmers, G. R. L., He, L., Melnichenko Y. B., Radliński A. P. & Blach, T. P. (2013). Pore structure characterization of North American shale gas reservoirs using USANS/SANS, gas adsorption, and mercury intrusion. Fuel, 103, 606-616.

Curtis, J. B. (2002). Fractured shale-gas systems. AAPG bulletin, 86(11), 1921-1938.

Curtis, M. E., Ambrose, R. J., & Sondergeld, C. H. (2010, January). Structural characterization of gas shales on the micro-and nano-scales. In Canadian unconventional resources and international petroleum conference. Society of Petroleum Engineers.

Chen, Y. D., & Yang, R. T. (1991). Concentration dependence of surface diffusion and zeolitic diffusion. AIChE journal, 37(10), 1579-1582.

Civan, F. (2010). Effective correlation of apparent gas permeability in tight porous media. Transport in porous media, 82(2), 375-384.

Civan, F., Devegowda, D., & Sigal, R. (2014). Rigorous modeling of gas transport in nano-darcy shale porous media under extreme pore proximity and elevated pressure conditions. In International Conference on Heat Transfer and Fluid Flow.

Cunningham, R. E., & Williams, R. J. J. (1980). Diffusion in gases and porous media (Vol. 1). New York: Plenum Press.

GEM, C. (2016). Version 2016 user's guide. Computer Modeling Group Ltd., Calgary, Alberta.

Darabi, H., Ettehad, A., Javadpour, F., & Sepehrnoori, K. (2012). Gas flow in ultra-tight shale strata. Journal of Fluid Mechanics, 710, 641-658.

Dong, J. J., Hsu, J. Y., Wu, W. J., Shimamoto, T., Hung, J. H., Yeh, E. C., ... & Sone, H. (2010). Stress-dependence of the permeability and porosity of sandstone and shale from TCDP Hole-A. International Journal of Rock Mechanics and Mining Sciences, 47(7), 1141-1157.

Du, X. D., Gu, M., Duan, S., & Xian, X. F. (2017). Investigation of CO2–CH4 Displacement and Transport in Shale for Enhanced Shale Gas Recovery and CO2 Sequestration. Journal of Energy Resources Technology, 139(1), 012909.

Ewart, T., Perrier, P., Graur, I., & Méolans, J. G. (2007). Tangential momemtum accommodation in microtube. Microfluidics and Nanofluidics, 3(6), 689-695.

Guo, C., Xu, J., Wu, K., Wei, M., & Liu, S. (2015). Study on gas flow through nano pores of shale gas reservoirs. Fuel, 143, 107-117.

Gunda, N. S. K., Joseph, J., Tamayol, A., Akbari, M., & Mitra, S. K. (2013). Measurement of pressure drop and flow resistance in microchannels with integrated micropillars. Microfluidics and nanofluidics, 14(3-4), 711-721.

Heller, R., & Zoback, M. (2014). Adsorption of methane and carbon dioxide on gas shale and pure mineral samples. Journal of Unconventional Oil and Gas Resources, 8, 14-24.

Jahandideh, A., & Jafarpour, B. (2016). Optimization of hydraulic fracturing design under spatially variable shale fracability. Journal of Petroleum Science and Engineering, 138, 174-188.

Jarrahian, A., & Heidaryan, E. (2014). A simple correlation to estimate natural gas viscosity. Journal of Natural Gas Science and Engineering, 20, 50-57.

Javadpour, F., Fisher, D., & Unsworth, M. (2007). Nanoscale gas flow in shale gas sediments. Journal of Canadian Petroleum Technology, 46(10).

Javadpour, F. (2009). Nanopores and apparent permeability of gas flow in mudrocks (shales and siltstone). Journal of Canadian Petroleum Technology, 48(08), 16-21.

Kargbo, D. M., Wilhelm, R. G., & Campbell, D. J. (2010). Natural gas plays in the Marcellus Shale: Challenges and potential opportunities.

Kuuskraa, V., Stevens, S. H., & Moodhe, K. D. (2013). Technically recoverable shale oil and shale gas resources: an assessment of 137 shale formations in 41 countries outside the United States. US Energy Information Administration, US Department of Energy.

Lee, D. S., Herman, J. D., Elsworth, D., Kim, H. T., & Lee, H. S. (2011). A critical evaluation of unconventional gas recovery from the marcellus shale, northeastern United States. KSCE Journal of Civil Engineering, 15(4), 679.

Landry, C. J., Prodanović, M., & Eichhubl, P. (2016). Direct simulation of supercritical gas flow in complex nanoporous media and prediction of apparent permeability. International Journal of Coal Geology, 159, 120-134.

Lee, S., Fischer, T. B., Stokes, M. R., Klingler, R. J., Ilavsky, J., McCarty, D. K., Wigand, M.O., Derkowski, A. & Winans, R. E. (2014). Dehydration effect on the pore size, porosity, and fractal parameters of shale rocks: Ultrasmall-angle X-ray scattering study. Energy & Fuels, 28(11), 6772-6779.

Li, B., Liu, R., & Jiang, Y. (2016). A multiple fractal model for estimating permeability of dual-porosity media. Journal of Hydrology, 540, 659-669.

Li, J., Jia, P., Wu, K., Wang, X., Qu, S., Shi, J., ... & Dong, Y. (2017). Gas Slippage in Tight Rocks With Sub-irreducible Water Saturation. Unconventional Resources Technology Conference (URTEC).

Lafferty, J. M. Foundations of Vacuum Science and Technology, 1998.

Levorsen, A. I., & Berry, F. A. (1967). Geology of petroleum (Vol. 8). San Francisco: WH Freeman.

Loucks, R. G., Reed, R. M., Ruppel, S. C., & Hammes, U. (2010, December). Spectrum of pore types in siliceous mudstones in shale-gas systems. In AAPG Hedberg Conference (Vol. 5, No. 10).

Loucks, R. G., Reed, R. M., Ruppel, S. C., & Jarvie, D. M. (2009). Morphology, genesis, and distribution of nanometer-scale pores in siliceous mudstones of the Mississippian Barnett Shale. Journal of sedimentary research, 79(12), 848-861.

Majumder, M., Chopra, N., & Hinds, B. J. (2011). Mass transport through carbon nanotube membranes in three different regimes: ionic diffusion and gas and liquid flow. ACS nano, 5(5), 3867-3877.

Marschang, R., Lee, S., Hewitt, A., & Moeller, T. (2014). Export of Marcellus Shale Gas.

Meyer, B. R., Bazan, L. W., Jacot, R. H., & Lattibeaudiere, M. G. (2010, January). Optimization of multiple transverse hydraulic fractures in horizontal wellbores. In SPE Unconventional Gas Conference. Society of Petroleum Engineers.

Miao, T., Yang, S., Long, Z., & Yu, B. (2015). Fractal analysis of permeability of dual-porosity media embedded with random fractures. International Journal of Heat and Mass Transfer, 88, 814-821.

Miao, T., Yang, S., Long, Z., & Yu, B. (2015). Fractal analysis of permeability of dual-porosity media embedded with random fractures. International Journal of Heat and Mass Transfer, 88, 814-821.

Miao, T., Yu, B., Duan, Y., & Fang, Q. (2015). A fractal analysis of permeability for fractured rocks. International Journal of Heat and Mass Transfer, 81, 75-80.

Munson, E. O. (2015). Reservoir characterization of the Duvernay Formation, Alberta: a pore-to basin-scale investigation (Doctoral dissertation, University of British Columbia).

Noy, A. (2013). Kinetic model of gas transport in carbon nanotube channels. The Journal of Physical Chemistry C, 117(15), 7656-7660.

Nikolov K. (2014). Shale gas and Snake oil – Geological characteristics of continuous petroleum resources and resource abundance evaluation assessment methodology for shale gas/oil in some European countries (Master dissertation, Aalborg University Esbjerg).

Rahmanian, M., Aguilera, R., & Kantzas, A. (2012). A New Unified Diffusion--Viscous-Flow Model Based on Pore-Level Studies of Tight Gas Formations. SPE Journal, 18(01), 38-49.

Rivard, C., Lavoie, D., Lefebvre, R., Séjourné, S., Lamontagne, C., & Duchesne, M. (2014). An overview of Canadian shale gas production and environmental concerns. International Journal of Coal Geology, 126, 64-76.

Roy, S., Raju, R., Chuang, H. F., Cruden, B. A., & Meyyappan, M. (2003). Modeling gas flow through microchannels and nanopores. Journal of applied physics, 93(8), 4870-4879.

Reed, R. M., & Loucks, R. G. (2007, April). Imaging nanoscale pores in the Mississippian Barnett Shale of the northern Fort Worth Basin. In AAPG Annual Convention Abstracts (Vol. 16, p. 115).

Ren, W., Li, G., Tian, S., Sheng, M., & Fan, X. (2016). An analytical model for real gas flow in shale nanopores with non‐circular cross‐section. AIChE Journal, 62(8), 2893-2901.

Ren, Y., Guo, X., Xie, C., & Wu, H. (2016). Experimental study on gas slippage of Marine Shale in Southern China. Petroleum, 2(2), 171-176.

Rogers, H. (2011). Shale gas—the unfolding story. Oxford Review of Economic Policy, 27(1), 117-143.

Shapiro, A. A., & Wesselingh, J. A. (2008). Gas transport in tight porous media: gas kinetic approach. Chemical Engineering Journal, 142(1), 14-22.

Sheng, M., Li, G., Huang, Z., Tian, S., Shah, S., & Geng, L. (2015). Pore-scale modeling and analysis of surface diffusion effects on shale-gas flow in Kerogen pores. Journal of Natural Gas Science and Engineering, 27, 979-985.

Singh, K. (2010). Problms & Soln In Chem Iit. Tata McGraw-Hill.

Singh, H., & Javadpour, F. (2013). Nonempirical apparent permeability of shale. Unconventional Resources Technology Conference (URTEC).

Slatt, R. M., & O'Brien, N. R. (2011). Pore types in the Barnett and Woodford gas shales: Contribution to understanding gas storage and migration pathways in fine-grained rocks. AAPG bulletin, 95(12), 2017-2030.

Sheng, M., Li, G., Huang, Z., Tian, S., Shah, S., & Geng, L. (2015). Pore-scale modeling and analysis of surface diffusion effects on shale-gas flow in Kerogen pores. Journal of Natural Gas Science and Engineering, 27, 979-985.

Shan, C., Zhang, T., Guo, J., Zhang, Z., & Yang, Y. (2015). Characterization of the micropore systems in high-rank coal reservoirs of the southern Sichuan Basin, ChinaCharacterization of the Micropore Systems in High-Rank Coal Reservoirs. AAPG Bulletin, 99(11), 2099-2119.

Soeder, D. J. (1988). Porosity and permeability of eastern Devonian gas shale. SPE Formation Evaluation, 3(01), 116-124.

Tassios, D. P. (2013). Applied chemical engineering thermodynamics. Springer.

Utpalendu K., Prasad, M., & Kazemi, H. (2013). Assessing Knudsen flow in gas-flow models of shale reservoirs. Can. Soc. Explor. Geophys. Rec, 38(5), 22-27.

Utpalendu K., & Prasad, M. (2013). Specific surface area and pore‐size distribution in clays and shales. Geophysical Prospecting, 61(2), 341-362.

Wang, J., Ryan, D., & Anthony, E. J. (2011). Reducing the greenhouse gas footprint of shale gas. Energy Policy, 39(12), 8196-8199.

Wang, J., Liu, H., Wang, L., Zhang, H., Luo, H., & Gao, Y. (2015). Apparent permeability for gas transport in nanopores of organic shale reservoirs including multiple effects. International Journal of Coal Geology, 152, 50-62.

Wang, M., & Li, Z. (2004). Micro-and nanoscale non-ideal gas Poiseuille flows in a consistent Boltzmann algorithm model. Journal of Micromechanics and Microengineering, 14(7), 1057.

Wang, M., Xue, H., Tian, S., Wilkins, R. W., & Wang, Z. (2015). Fractal characteristics of Upper Cretaceous lacustrine shale from the Songliao Basin, NE China. Marine and Petroleum Geology, 67, 144-153.

Wilson, M. J., Wilson, L., & Shaldybin, M. V. (2016). Clay mineralogy and unconventional hydrocarbon shale reservoirs in the USA. II. Implications of predominantly illitic clays on the physico-chemical properties of shales. Earth-Science Reviews, 158, 1-8.

White, F. M., & Corfield, I. (2006). Viscous fluid flow (Vol. 3). New York: McGraw-Hill.

Wu, C., Tuo, J., Zhang, L., Zhang, M., Li, J., Liu, Y., & Qian, Y. (2017). Pore characteristics differences between clay-rich and clay-poor shales of the Lower Cambrian Niutitang Formation in the Northern Guizhou area, and insights into shale gas storage mechanisms. International Journal of Coal Geology, 178, 13-25.

Wu, K., Chen, Z., & Li, X. (2015). Real gas transport through nanopores of varying cross-section type and shape in shale gas reservoirs. Chemical Engineering Journal, 281, 813-825.

Wu, K., Li, X., Wang, C., Chen, Z., & Yu, W. (2015). A model for gas transport in microfractures of shale and tight gas reservoirs. AIChE Journal, 61(6), 2079-2088.

Wu, K., Chen, Z., Li, X., Guo, C., & Wei, M. (2016). A model for multiple transport mechanisms through nanopores of shale gas reservoirs with real gas effect–adsorption-mechanic coupling. International Journal of Heat and Mass Transfer, 93, 408-426.

Wu, K., Chen, Z., Li, X., Xu, J., Li, J., Wang, K., Wang H, Wang S & Dong, X. (2017). Flow behavior of gas confined in nanoporous shale at high pressure: Real gas effect. Fuel, 205, 173-183.

Wu, K., Li, X., Wang, C., Yu, W., & Chen, Z. (2015). Model for surface diffusion of adsorbed gas in nanopores of shale gas reservoirs. Industrial & Engineering Chemistry Research, 54(12), 3225-3236.

Xu, J., Wu, K., Yang, S., Cao, J., Chen, Z., Pan, Y., & Yan, B. (2017). Real gas transport in tapered noncircular nanopores of shale rocks. AIChE Journal, 63(7), 3224-3242.

Xu J, Wu K, Li R, Li Z, Li J, Xu Q, Chen Z. (2018). Real Gas Transport in Shale Matrix with Fractal Structures. Fuel, 218, 353-363.

Xu, P., Qiu, S., Yu, B., & Jiang, Z. (2013). Prediction of relative permeability in unsaturated porous media with a fractal approach. International Journal of Heat and Mass Transfer, 64, 829-837.

Yamaguchi, H., Hanawa, T., Yamamoto, O., Matsuda, Y., Egami, Y., & Niimi, T. (2011). Experimental measurement on tangential momentum accommodation coefficient in a single microtube. Microfluidics and nanofluidics, 11(1), 57-64.

Yang, S., Fu, H., & Yu, B. (2017). Fractal analysis of flow resistance in tree-like branching networks with roughened microchannels. Fractals, 25(01), 1750008.

Yang, R., Huang, Z., Yu, W., Li, G., Ren, W., Zuo, L., ... & Sheng, M. (2016). A comprehensive model for real gas transport in shale formations with complex non-planar fracture networks. Scientific reports, 6, 36673.

Yang, S., Chen, Z., Wei, Y., Wu, K., Shao, L., & Wu, W. (2015, October). A Simulation Model for Accurate Prediction of Uneven Proppant Distribution in the Marcellus Shale Coupled with Reservoir Geomechanics. In SPE Eastern Regional Meeting. Society of Petroleum Engineers.

Ye, Z., Chen, D., & Pan, Z. (2015). A unified method to evaluate shale gas flow behaviours in different flow regions. Journal of Natural Gas Science and Engineering, 26, 205-215.

Yu, B., & Li, J. (2001). Some fractal characters of porous media. Fractals, 9(03), 365-372.

Yu, W., Wu, K., Sepehrnoori, K., & Xu, W. (2017). A comprehensive model for simulation of gas transport in shale formation with complex hydraulic-fracture geometry. SPE Reservoir Evaluation & Engineering, 20(03), 547-561.

Yu, W., & Sepehrnoori, K. (2014). An efficient reservoir-simulation approach to design and optimize unconventional gas production. Journal of Canadian Petroleum Technology, 53(02), 109-121.

Zhan, J., Lu, J., Fogwill, A., Ulovich, I., Cao, J. P., He, R., & Chen, Z. (2017, November). An Integrated Numerical Simulation Scheme to Predict Shale Gas Production of a Multi-Fractured Horizontal Well. In SPE Abu Dhabi International Petroleum Exhibition & Conference. Society of Petroleum Engineers.

Zhang, J., Fan, T., Li, J., Zhang, J., Li, Y., Wu, Y., & Xiong, W. (2015). Characterization of the Lower Cambrian shale in the Northwestern Guizhou province, South China: implications for shale-gas potential. Energy & Fuels, 29(10), 6383-6393.

Zhang, L., Shan, B., Zhao, Y., Du, J., Chen, J., & Tao, X. (2018). Gas Transport Model in Organic Shale Nanopores Considering Langmuir Slip Conditions and Diffusion: Pore Confinement, Real Gas, and Geomechanical Effects. Energies, 11(1), 223.

Zhang, T., Ellis, G. S., Ruppel, S. C., Milliken, K., & Yang, R. (2012). Effect of organic-matter type and thermal maturity on methane adsorption in shale-gas systems. Organic geochemistry, 47, 120-131.

Zhao, Y. L., & Zhang, L. (2017). Numerical solution of fractured horizontal wells in shale gas reservoirs considering multiple transport mechanisms. Journal of Geophysics and Engineering.

Zheng, Q., & Yu, B. (2012). A fractal permeability model for gas flow through dual-porosity media. Journal of Applied Physics, 111(2), 024316.

Zhu, W., Tian, W., Gao, Y., Deng, J., Zhang, X., Qi, Q., & Ma, Q. (2016). Study on experiment conditions of marine shale gas seepage law. Journal of Natural Gas Geoscience, 1(2), 157-163.